SQUID-on-tip sensors for real-space magnetic imaging of a chiral magnet

Inauguraldissertation

zur Erlangung der Würde eines Doktors der Philosophie

vorgelegt der
Philosophisch-Naturwissenschaftlichen Fakultät
der Universität Basel

von

Giulio Romagnoli

von Italien

Basel, 2024

Genehmigt von der Philosophisch-Naturwissenschaftlichen Fakultät auf Antrag von

Prof. Dr. Martino Poggio
Erstbetreuer/in

Prof. Dr. Ilaria Zardo
Zweitbetreuer/in

Dr. Amit Finkler
Externe/r Experte/in

Basel, den 21. Juni 2022

Prof. Dr. Marcel Mayor
Dekan/in

Contents

List of Symbols

SQUID	**S**uperconducting **QU**uantum **I**nterference **D**evice
SSM	**S**canning **S**QUID **M**icroscopy
SOT	**S**QUID-**O**n-**T**ip
LTEM	**L**orentz **T**ransmission **E**lectron **M**icroscopy
MFM	**M**agnetic **F**orce **M**icroscope
SNVM	**S**canning **N**itrogen **V**acancy **C**entre **M**icroscopy
SANS	**S**mall **A**ngle **N**eutron **S**cattering
SPM	**S**canning **P**robe **M**icroscopy
STM	**S**canning **T**unneling **M**icroscope
SFM	**S**canning **F**orce **M**icroscope
AFM	**A**tomic **F**orce **M**icroscope
SHM	**S**canning **H**all **B**ar **M**icroscopy
ODMR	**O**ptically **D**etected **M**agnetic **R**esonance **S**pectroscopy
RCSJ	**R**esistively and **C**apacitively **S**hunted **J**unction
ID	**I**nner **D**iameter
OD	**O**uter **D**iameter
SEM	**S**canning **E**lectron **M**icroscope
UHV	**U**ltra **H**igh **V**acuum
SSAA	**SQUID** **S**eries **A**rray **A**mplifier
FLL	**F**lux-**L**ocked **L**oop
PLL	**P**hase-**L**ocked **L**oop
ZFC	**Z**ero-**F**ield **C**ooling
DMI	**D**zyaloshinskii-**M**oriya **I**nteraction
IVC	**I**nner **V**acuum **C**hamber
FFT	**F**ast **F**ourier **T**ransform

Introduction

Nanomagnetism is an area of research in Physics that studies magnetic properties of samples which have at least one dimension in the nanometer range. The aim of nanomagnetism is to investigate properties and applications of nano-objects, such as particles, dots, wires, or thin films or bulk samples exhibiting changes in magnetism (like magnetic domains or interfaces) at the nanoscale.

Among all the applications of nanomagnetism, the most successful one has been in the field of information storage and data communication. In the last few decades, magnetic recording has drastically improved, getting able to boost both areal density and data rate. The rapid growth of this technology was made possible only by the effort in analyzing the properties of magnetic thin films and of small magnetic particles that constitute a key part of magnetic read heads and hard disk platters.

Another emerging field where magnetism plays a crucial role is spintronics, for the implementation of the next generation of nanoelectronic devices with reduced power consumption, increased memory and processing capability. Such devices are based on the interaction of magnetic materials with the spin degree of freedom of an electric current and make use of films and other magnetic structures at the nanoscale.

To investigate the electronic correlations that give rise rise to macroscopic phenomena such as magnetism, superconductivity, and topological phases, it is necessary to fully understand the micro- or nanoscopic mechanism behind them. This study often requires probes with very fine spatial resolution, capable to sense changes in magnetic field over a length scale of hundreds of nanometers or less. Not many imaging techniques can provide that, especially when the information is not accessible by optical or topographic images.

Magnetic field changes not only take place on short distances, but might as well be extremely weak to probe. This happens when the electronic properties are defined by a small fraction of electrons participating in a certain order, or when the phenomena take place in material layers that are screened by other layers above them. Furthermore, perturbation of the electrons by the sensing probe can be detrimental for the observation of some phenomena. So, in many experiments, a sensitive sensor offering high spatial resolution and low invasiveness is desired.

Among the variety of magnetic probes, the one interesting this thesis work is the Superconducting Quantum Interference Device (SQUID). SQUIDs are superconducting interferometers, defined by a loop threaded by magnetic field, and are one of the most powerful magnetometers, due to their excellent sensitivity to stray magnetic field and a negligible perturbation of the sample under investigation. A further strong point is their versatility to probe a broad range of electronic orders, due to the possibility to perform local thermometry and susceptometry measurements.

The success of SQUID microscopy comes from the balance between magnetic field sensitivity and spatial resolution. The latter is mainly influenced by the size of the SQUID loop and by the distance of the loop from the studied surface. Great effort and research were invested over the years in designing SQUIDs with miniaturized

loops and in configurations that could be approached hundreds of nanometers away from the surface of interest [1].
A game changer in the history of Scanning SQUID Microscopy (SSM) is represented by the innovative idea, by Finkler et al. in 2010 [2], of fabricating a SQUID loop on the apex of a laser-pulled quartz pipette, having a sharp tip with an apex diameter of few tens of nanometers. This configuration brings three main advantages: a easier, self-aligned fabrication process, the possibility to miniaturize and tune the SQUID loop down to a nanometric size and, ultimately, a design that allows to move the SQUID loop and approach it at sample to probe distances comparable to the SQUID diameter. The consequent fine spatial resolution that can be achieved has led the SQUID-on-Tip (SOT) technique to tens of remarkable achievements over the last decade, probing magnetic fields and heat dissipation with sub-100 nm resolution [3–7].
In many reported SOT publications, a common material choice for the SQUID fabrication is Pb, due to its softness and the provided extremely low magnetic noise. The softness plays a role when depositing superconducting thin films on top of the curved pipette surface, while the noise limits the minimum detectable magnetic field. Other reported evaporated materials providing low noise SQUID sensors are Sn and In [8].

In this thesis work, a contribution to the SOT field is brought, focused on implementing a new deposition method, that extends the range of materials that can be used to coat the quartz pipettes. In fact, thermal evaporation is limited to elemental materials and not suitable to deposit metal alloys. An alternative choice is given by magnetron sputtering, which is a physical vapor deposition method, using a plasma of energetic ions to extract atoms from a metallic target and coat a surface of interest. Sputtering is compatible with a broad range of materials and is mainly used for thin film deposition on planar wafers due to the offered low film roughness, the strong material adhesion and the high film purity. On the other hand, contrary to the directional, point-like source thermal evaporation, magnetron sputtering provides a diffusive deposition.
Fabricating SOT sensors via thin film sputtering deposition was already reported in literature, with a method based on creating a collimated, differential pressure, magnetron sputtering technique [9]. The difference in pressure allows for a quasi-ballistic flow of atoms from the target to the pipette, helping to preserve the SQUID geometry. Here we start by replicating this method, and resulting SOT sensors with sub-100 nm diameter made of MoGe are shown. The choice of MoGe is motivated by the will to fabricate a SQUID suitable to work in presence of high applied magnetic field, which offers the potential to study interesting phenomena, such as quantum hall effect in 2D electron gas.
As a further step towards sputtered SOT sensors, we invested effort in depositing superconducting materials via direct magnetron sputtering method, without the need of a differential pressure, collimation system. The initial choice of material is Nb, which has a high critical temperature and is known to have a low kinetic inductance, and so a high magnetic response. The idea of removing the collimation chamber is mainly motivated by two reasons: from a practical point of view, the collimation process elongates the sputtering time, leading to more maintenance of the setup, while the achieved thin film quality is lower. As a further improvement of the film quality, the thin superconducting film is protected by thin Ti layers from the contamination from quartz underneath and from degradation from oxidation. The quality improvement of the thin Nb film is demonstrated by a electric transport test performed with

planar devices, where the encapsulated film sputtered without collimation system is proved to enhance the critical temperature by a 25% factor with respect to a film with same thickness sputtered with collimation.

The property of directionality in depositing superconducting materials via magnetron sputtering method is achieved by a short distance from the target to the pipette, combined to the engineering of the capillary shape. The pipettes include four, symmetric, grooves, which act as a physical barrier and help in avoiding electrical shorts between the two superconducting electrodes. The shape of the groove is customized in order to maximize this effect.

The results achieved by magnetron sputtering deposited Nb SOTs are presented in Chap. 2, together with the results of MoGe SOTs, fabricated via collimated magnetron sputtered, and of thermally evaporated Pb SOTs. A comparison between these three materials can be made and the choice of material according to the planned experimental application is discussed.

Chap. 3 focuses on the application of a MoGe SOT for the investigation of magnetic phases in a bulk crystal of Cu_2OSeO_3. This chiral magnet is the first insulating material which was found to host a lattice of topologically non-trivial spin textures called magnetic skyrmions [10]. Skyrmions can be extremely small, with diameters in the nanometer range, and behave as quasi-particles that can be created, manipulated, annihilated, which makes them suitable for applications in the fields of logic technology and information storage. Furthermore, skyrmions in Cu_2OSeO_3 exert a strong magnetoelectric effect: being this material an insulator, this gives the possibility to use an electric field to manipulate skyrmions without energy loss due to Joule heating.

Usually, skyrmion phases exist at a relatively high temperature of tens of Kelvin, because they require thermal fluctuations to become thermodynamically stable in bulk materials. Such high temperature skyrmion phases cannot be accessed by the SOT technique due to the limitation imposed by the critical temperature of our sensor. However, recent measurements by Chacon et al. [11] showed the presence of a second, low temperature skyrmion phase in Cu_2OSeO_3, which appears when an external magnetic field is applied along the [001] crystal axis. This phase is distinct from the well-known high temperature phase, is highly hysteretic, and appears to be stabilized by cubic anisotropy.

Real-space imaging of magnetic textures at the surface of a bulk crystal hosting skyrmions can shed light on the spin arrangement inside the crystal and on the mechanism through which single skyrmions appear and aggregate in a ordered lattice. SQUID microscopy is a perfect candidate for such an investigation, thanks to the high magnetic sensitivity, the fine spatial resolution and the low sample invasiveness.

Contrary, we can mention other well-established techniques which show potential limitations. One of them is Lorentz Transmission Electron Microscopy (LTEM), a powerful tool to study magnetic domain structures formed due to the interactions between the electron beam and the emergent magnetic fields accompaying their intrinsic local magnetization distribution [12]. It provides insight into magnetic structures, with a spatial resolution better than 20 nm. However, the transmission requires the sample to be extremely thin, so that LTEM is not suitable to investigate bulk crystals.

Another candidate could be Magnetic Force Microscopy (MFM), whose imaging capability relies on the magnetostatic interaction between a magnetic tip and the stray magnetic field of the sample under investigation. Despite a spatial resolution as

good as 10 nm and the possibility to scan over bulk crystals, MFM is not so sensitive to weakly magnetized samples and the tip can result to be invasive, in terms of sample perturbation.
A possibility is offered by Scanning Nitrogen-Vacancy Centre Microscopy (SNVM), a technique which is based on a nitrogen-vacancy centre, hosted within a crystalline diamond nanopillar, scanning over a surface of interest [13–15]. It has emerged as a powerful microscopy for studying weak stray field patterns with nanometer resolution. However, due to the internal crystal anisotropy of the spin defect, external bias fields, critical for the study of magnetic materials, must be applied along specific spatial directions. Some further challenges emerge when working at cryogenic temperature and a limitation concerns the relatively low operating field of sensor.

Our work used a SOT made of MoGe with high flux sensitivity and sub-100 nm spatial resolution to perform real-space imaging of the magnetic textures at the surface of a polished Cu_2OSeO_3 crystal. Magnetic images at 1.8 K and at different magnetic fields applied along the [001] crystallographic direction are reported. By changing magnetic field, it is possible to resolve the helical, tilted conical and field polarized magnetic phases and to extract the angle of the tilted conical modulation with respect to the magnetic field axis. This angle matches the value measured by Small Angle Neutron Scattering (SANS) technique [11]. A further topic is brought into discussion, about the observation in the tilted conical phase of circular objects, with estimated dimensions of 60 nm. The shape of these objects, either single or disposed in straight lines, remind magnetic skyrmions and the presence of a mixed tilted conical and low temperature skyrmion phase would be supported by the phase diagram reported in literature [11]. Due to the size of magnetic skyrmions in this material and a lack of spatial resolution, it was not possible to confirm their observation; however, these results are a promising first step towards real-space imaging of the low temperature skyrmion lattice in Cu_2OSeO_3.

Chapter 1

Background

The purpose of this chapter is to summarize the essential background necessary to understand the following experimental chapters.

Initially, a short history of scanning probe microscopy is provided, reporting the first experimental steps that led to what now is an extremely broad and well developed field of research. In this thesis, special attention is paid to scanning probe microscopy techniques suitable to map stray magnetic fields.

The main section of the chapter describes in detail the SSM technique. Josephson junctions and SQUID loops are introduced and the dependence of their behavior on many parameters is analyzed. Then the focus shifts on how to use a SQUID sensor to perform a scanning probe microscopy experiment. A brief overview of the approach with planar on-chip SQUIDs is reported, followed by a detailed section regarding the SOT technique.

1.1 Origin of Scanning Probe Microscopy

The field of Scanning Probe Microscopy (SPM) owns its origin to the seminal talk given by Richard Feynman in 1959 at the annual meeting of the American Physical Society. The talk, entitled *"There's Plenty of Room at the Bottom"* was focusing on the problem of manipulating and controlling things on a small scale and was covering a broad range of concepts and opportunities, that subsequently would have been topics of interest in the field of nanoscience. For example, he asserted that laws of physics do not prevent manipulation and interrogation of materials at the atomic scale and he discussed some concepts on how to produce nanometer-sized devices. Finally, Feynman highlighted the potential impact of the capability to interrogate and manipulate matter at the atomic scale and asserted that this ability would give rise to technologies such as high-density data storage, materials engineering at the atomic scale, and miniaturization of computing devices.

The bridge between macroscopic world and single-atom manipulation was the invention of SPM, which at first provided real-space images of surfaces with high spatial resolution. These images rely on the detection of the local interaction between a small probe tip and a surface, on a spatial range that can vary from hundreds of micrometers down to few picometers. According to the type of interaction, and so to the particular SPM technique, images can represent physical surface topographic contrast, electronic structure, electric and magnetic fields and so on [16].

The first important step in SPM was the invention of the Scanning Tunnel Microscope (STM) in 1982 by Binnig and Rohrer [17], an invention that led them to win the Nobel prize for physics four years later. The STM consists of a small, sharp metallic needle, scanning over a conductive surface of interest at very short distance (less than 1 nm). At such distance, a quantum effect called tunneling takes place: regardless of the thin insulator or vacuum gap, an electric current can flow from the very last atom of the tip apex to individual atoms at the surface [18, 19]. By controlling the amount of tunneling current, it is possible to tune the distance between tip and surface. In a typical STM experiment, piezoelectric elements are used to move the tip in three directions with sub-angstrom resolution. Feedback electronics allows to keep a tip to sample distance corresponding to a chosen constant value of tunneling current. The distance is recorded by a computer as a function of lateral (x, y) position and displayed as a microscope image. For achieving a scanning spatial resolution at the atomic scale, a key element is to decouple the experimental setup from external mechanical vibrations.

The few ingredients required for a STM experiment constitute the base elements for all the following, widely used and developed, SPM techniques: a short-range interaction, a local probe scanning over the surface of interest and sensing the probe-sample interaction with fine spatial resolution, an electronics recording and analyzing the data, an advanced setup design to isolate the experiment from external noise sources such as mechanical vibrations.

The second milestone in SPM was the invention of the Scanning Force Microscope (SFM) in 1986 by Binnig, Quate and Gerber [20]. This instrument relies on the short-range force interaction between probe and surface of interest. A typical experiment is analogous to what already pictured for STM, with the difference that the probe to surface distance is controlled in such a way the force between tip and sample remains constant. This kind of device constitutes an extension of STM: in fact, while the current flow by tunneling effect is limited to conductor or semi-conductor sample surfaces, SFM can investigate the topography of any surface, conductive or insulating. Assuming that the resolution of the instrument is determined by the force between the closest atoms of tip and surface, this microscope is usually known as Atomic Force Microscope (AFM).

Over the course of few years, an entire family of SPMs grew up and it became possible to access different types of physical information by suitably replacing or altering the probe according to the specific properties of the material under investigation. An example is represented by MFM [21], where the tip of a AFM cantilever is coated with a magnetic material such as cobalt. This allows the probe to map the stray field emanating from a sample surface with high spatial resolution and sensitivity. In a similar way, AFM probes modified with biological materials can be used to achieve maps of biomolecular forces [22]. In addition to two-dimensional images, SPM techniques represent a powerful tool to manipulate materials at the nanoscale: in fact, local probes can be used to deposit material, or as a lithographic tool to etch material away, or as a tool to change orientation of magnetic domains of a material.

For the purpose of this thesis, among all the SPM techniques that can be mentioned, some further attention will be paid to the ones suitable for magnetic field imaging at the nanoscale.

1.2 SPM techniques for magnetic field imaging

The development of magnetic imaging techniques is driven by applications in fields such as magnetic storage and information processing, where an understanding of magnetostatics and dynamics with spatial resolution of tens of nanometers or better is required. This kind of imaging is of great relevance, since it sheds light on properties and phenomena that cannot be investigated by topographic or optical imaging

techniques. To just mention few examples, superconducting properties can be studied, such as clusters, vortices, penetration depth [23]. Material properties, such as length scales, role of defects, inhomogeneities and interations get accessible in a not invasive way. It is possible to reconstruct magnetization patterns, current distributions and spin configurations. Moreover, the very fine spatial resolution allows to investigate the properties of engineered 2D materials [24].
Among the most widely used techniques to map stray magnetic fields, either generated by current distributions or magnetization patterns, very important are: MFM, with standard AFM cantilever probes or individual nanowires; SNVM; Scanning Hall bar Microscopy (SHM); SSM, realized with planar devices or more complex designs. In the following, a short, general introduction for all these techniques is reported, with the working principle, operation range and state-of-the-art of the sensors. SSM will then be covered more in detail in the next section, since it is of primary importance for the thesis contents.

As previously mentioned, MFM was developed as an improvement of AFM and it was the first SPM technique to be implemented for imaging magnetic fields of surfaces with high spatial resolution [21, 25]. The imaging capability relies on the magnetostatic interaction between a magnetic tip and the stray magnetic field of the sample under investigation.
In a typical experiment, the probe is constituted by a commercial AFM cantilever made of Si, SiO_2, Si_3N_4, coated with a ferromagnetic material, such as Co or Ni. The cantilever is scanned over a surface of interest due to the use of piezoelectric elements, while the motion amplitude and mechanical frequency of the cantilever are recorded by optical deflection or interferometry. In particular, both amplitude and mechanical frequency respond to gradients of the stray field of the sample.
To mention some advantages, MFM experiments can take place under different environmental conditions (such as air, vacuum, liquids) and under a wide temperature range. Scanning is rather fast, in such a way it is possible to cover an area of several squared micrometers in few minutes. On the other hand, MFM images only provide information about stray field gradients; reconstructing a map of the exact magnetic field is often not trivial and requires a process of deconvolution where the shape of the tip and its magnetization configuration are known.
Speaking about performance, the cantilever's design leads to very high spring constant values (order of magnitude of 1 N/m). This gives the benefit of fine spatial resolution (tens of nanometers, down to 10 nm in vacuum and at cryogenic temperature [26, 27]). However, MFM is not so sensitive to weakly magnetized samples, in fact typical stray field gradients have to be on the order of magnitude of tens of $\mathrm{T/m\sqrt{Hz}}$. Moreover, the tip can result to be invasive, in terms of perturbation of the sample surface.
A valid alternative to cantilever probes is constituted by carbon nanotubes [28] or single nanowires [29, 30]. The smaller size of such probes naturally gives the advantages of low invasiveness on the sample surface, better spatial resolution and really good force sensitivity (as good as 1 $\mathrm{aN/\sqrt{Hz}}$ [31]) and magnetic sensitivity ($\mathrm{nT/\sqrt{Hz}}$ [32]). However, both nanotubes and nanowires are still in a preliminary stage and are not beyond proof-of-principle stage yet.
The sensitivity to magnetic fields and magnetic field gradients is finally limited by thermal noise, causing random fluctuations in the measurements of frequency and mechanical amplitude of either cantilevers or nanowires. It is important to mention that sensitivity also depends on other parameters, such as probe to sample distance and type of measurement (DC or AC). Moreover, additional noise sources, such as

temperature variations, can avoid to reach the thermal limit on frequency measurements.
Summarizing the key parameters [27, 33–35], both cantilevers and nanowires allow to measure from above room temperature down to cryogenic temperature, and with external applied magnetic fields of 10 T or more. As a combination of sensor size and sensor to sample distance, typical spatial resolution is 10 - 100 nm for cantilevers and 100 nm for nanowires. For what concerns magnetic sensitivity, nanowires turn out to be much more sensitive, showing an AC/DC sensitivity of few $\mathrm{nT}/\sqrt{\mathrm{Hz}}$, while cantilevers have AC sensitivity of about 200 $\mathrm{nT}/\sqrt{\mathrm{Hz}}$ and DC sensitivity of 10 - 100 $\mu\mathrm{T}/\sqrt{\mathrm{Hz}}$.

Originated in 2008, SNVM is a quite novel technique, which uses a nitrogen-vacancy centre, hosted within a crystalline diamond nanopillar to scan over a surface of interest [13–15]. NV centres are electronic defect spins in diamond, which are usually accessed by optical setup.
Experiments involve the use of optically detected magnetic resonance spectroscopy (ODMR), which consists in exciting and at the same time optically reading out the state of the defect spin, while the electron paramagnetic resonance spectrum of the nitrogen-vacancy is recorded. The mechanism providing magnetic field sensitivity is a Zeeman shift of the spin resonances: in presence of a weak, external magnetic field, with a component parallel to the vacancy symmetry axis, the $m_s = \pm 1$ spin states undergo a linear shift, proportional to the free-electron gyromagnetic ratio $\gamma = 2\pi \cdot 28$ GHz/T. So, while exciting the defect spin either by continuous wave or by microwave excitation, the ODMR spectrum records a change in the optical intensity [36].
In a typical SPM experiment, nitrogen-vacancy centres are implanted at a depth of few tens of nanometers from the edge of the nanopillar, with a state-of-the-art implantation depth of 10 nm [37]. The really short distance is of great importance in order to maximize spatial resolution and sensitivity. As standard for other SPM techniques, the probe is kept fixed at one position, while the sample underneath is moved by a set of piezoelectric elements. To control the pillar to sample distance and make as short as possible, the probe can be coupled to a mechanical tuning fork. As already mentioned, the excitation of the defect spin and the fluorescence detection are optical and are provided by an objective lens placed above the pillar.
For what concerns the performance of this technique, the best spatial resolution is around 20 nm [38], even though 10 nm is achievable if a shallow nitrogen-vacancy centre is combined to a very short implantation depth and the sample is scanned at the minimum pillar to surface distance. Magnetic field sensitivity is about 100 $\mathrm{nT}/\sqrt{\mathrm{Hz}}$ [39] for AC signals and few $\mu\mathrm{T}/\sqrt{\mathrm{Hz}}$ [40] for DC signals. Temperature operation range is in priciple very broad, in fact it is possible to operate from room temperature down to 1 K. However, some challenges emerge at cryogenic temperatures, related to charge stability, reduction of photoluminescence contrast and possible perturbation of fragile samples due to the optical excitation. Experiments at high fields may be challenging as well, because of the high-frequency microwave needed to excite the electron spin and a spin-level mixing phenomenon taking place for fields which are misaligned from the nitrogen-vacancy symmetry axis [41].
The ultimate noise limiting SNVM is photon shot noise from the optical read-out [42]. The minimum magnetic field which can be detected, $B_{\mathrm{min}} = 1/\gamma\epsilon\sqrt{I_0 t_{\mathrm{int}} T_2}$, is a function of gyromagnetic ratio γ, optical contrast ϵ, maximum photon count rate I_0, photon integration time t_{int} and decoherence time T_2. This leads to the AC and DC sensitivity previously reported. Further improvements are not straightforward,

but might be achieved by reducing the implantation depth while maintaining the coherence properties. In fact, the combination of 2 - 3 nm implantation depth with decoherence time T_2 greater than 10 μs [43] could lead to a AC sensitivity below 10 nT/$\sqrt{\text{Hz}}$.

SHM bases its working principle on the Hall effect [23]. When a longitudinal current I_y flows through the bar in presence of an external magnetic field B_z oriented perpendicular to the plane of the Hall bar, the bar develops a transverse voltage $V_\text{x} = -I_\text{y}B_\text{z}/en$, where n is the carrier density per unit area of the Hall bar. This implies that large Hall voltages can be developed by materials which have a small carrier density per unit area, such as semi-metals, semi-conductors or 2D electron gases at the interface between semi-conductors with different band gaps. Following this concept, a Hall bar sensor can be used as a scanning probe tool: when in proximity to a sample surface of interest characterized by a certain magnetic field B_z oriented perpendicular to the plane of the Hall bar, the Hall sensor measures a transverse voltage V_x proportional to the magnetic field averaged over the sensor.
After initial Hall bar systems made of Bi, InSb, GaAs, more advanced and complex structures were realized, showing smaller size and higher sensitivity to magnetic field. To mention some materials, GaAs/Al$_\text{x}$Ga$_\text{1-x}$As [44–46], GaSb/InAs/GaSb [47], Si/SiGe [48] and InGaAs/InP [49] were used.
Speaking about permormance, the sensors have a spatial resolution of 100 nm, which is mainly limited by the fact that the 2D electron gas is not in contact with the outer surface, but in fact is positioned 50 - 100 nm underneath. A recent work [50] using GaAs/Al$_\text{x}$Ga$_\text{1-x}$As heterojunction electron gas material, at cryogenic temperature, reports a magnetic field noise of 500 μT/$\sqrt{\text{Hz}}$ and a spin sensitivity of 1.2×10^4 $\mu_\text{B}/\sqrt{\text{Hz}}$. From the point of view of temperature operation, it is possible to work in a very broad range; however, heterojunctions become less sensitive at higher temperatures due to thermal noise. In fact, as estimated by the work of Boero et al. [51], the minimum detectable magnetic field in a micro-Hall cross geometry is limited by Johnson noise and can be expressed by $B_\text{min} = \sqrt{4k_\text{B}TR_0}/wv_\text{sat}$, where k_B is the Boltzmann constant, T is the working temperature, R_0 is the output resistance at zero magnetic field, w is the width of the cross and v_sat is the saturation carrier drift velocity. So it appears convenient to perform experiments at cryogenic temperature, since the minimum detectable field scales as $\sqrt{T}$. However, Johnson noise in micro-Hall bars is often overcome by the $1/f$ noise [50], which leads to a minimum detectable field of $B_\text{min} \approx \sqrt{\alpha_\text{H}G_\text{N}\Delta f/\mu^2 d^2 nf}$, where α_H is the Hooge's $1/f$ noise parameter, G_N is a constant, Δf is the measurement bandwidth, μ is the mobility, d is the sensor size, n is the carrier density and f is the frequency.

SSM has its origins in the early 1980s and uses SQUID sensors, whose characteristic is to be extremely sensitive to magnetic flux. The device consists of a superconducting ring, with two Josephson junctions enclosed in it. For a more detailed treatment we refer to the second part of the chapter, while here only the fundamental basics will be covered. In a typical operation condition, the SQUID is biased by a current and an external magnetic field is applied in the direction orthogonal to the ring, in such a way magnetic flux is threading the superconducting loop. The sensitivity to magnetic flux comes from the fact that the critical current of the SQUID (i.e. the maximum current that can flow through the loop before the device transitions to the normal metal state) is periodic in the magnetic flux through the loop, with the periodicity of a flux quantum Φ_0. By biasing the device with the appropriate current, it is possible to measure voltages across the SQUID that correspond to changes in the magnetic flux through the loop equivalent to fractions of Φ_0, typically down to $10^{-6}\ \Phi_0/\sqrt{\mathrm{Hz}}$. This sensitivity comes to the price that superconductivity only works below a critical temperature T_c, which depends on the applied magnetic field and current and ultimately is a property of the superconducting material used to fabricate the SQUID. Excluding high critical temperature materials, about which there is plenty of research, conventional superconductors have a T_c below 8 - 10 K.

In a SPM experiment, the sample of interest is scanned by a DC SQUID or a pick-up loop inductively coupled to it [24, 52]. As in other techniques, piezoelectric elements are used to move the sample underneath the sensor and the isolation from vibrations is important in order to approach the SQUID close to the surface of interest. To finely control the probe to surface distance, the sensor can be coupled to a mechanical tuning fork [53]. Typical scans are few minutes long, up to several hours if a very long integration time is needed. A major difference is that in almost all cases the probe is placed in vacuum and at low temperatures inside a cryostat. This enhances the difficulty of the experiment, as well as the time required to perform it, due to warm-up and cool-down thermal cycles.

In order to combine good magnetic flux sensitivity to a fine spatial resolution, lot of effort is invested in reducing the loop size. In one approach, nano-lithography has stepped forward to reduce the size of the pick-up loop of a conventional SQUID. This miniaturization is followed by placing the loop at the corner of the chip, as close as possible to the edge, so that it can get close to the sample of interest. To mention the state-of-the-art of this technique, the work from Kirtley et al. [1] has provided sub-micrometer magnetic imaging resolution and sensitivity of 130 $\mathrm{nT}/\sqrt{\mathrm{Hz}}$ by designing a small loop with an inner diameter of 200 nm. This good performance comes to the price of a complex nano-fabrication process. A second, more recent approach, which is the main topic of this thesis, consists on fabricating a SQUID sensor on the apex of a laser-pulled quartz capillary. This idea from Finkler et al. in 2010 [2] has led to several ways and materials to coat quartz capillaries [9] and has resulted in scanning SQUID sensors with diameters as small as 50 nm, spatial resolution of about 100 nm and magnetic field sensitivity of 5 $\mathrm{nT}/\sqrt{\mathrm{Hz}}$ [54].

As analyzed from Kirtley et al. [23], there are several sources of noise that ultimately limit the SQUID sensitivity to magnetic flux. A role is played by Johnson noise, shot noise, quantum noise and $1/f$ noise. For nano-scale SQUIDs and at frequencies in the KHz range or higher, $1/f$ noise is negligible and quantum noise defines the minimum detectable magnetic flux to be $\Phi_Q = \sqrt{\hbar L}$, where $\hbar$ is the Planck's constant and L is the SQUID loop inductance [55, 56]. State-of-art sensors, with diameters of 50 nm and made of Pb, in the KHz range have reported to detect a minimum flux of $\Phi_{\mathrm{min}} = 50\ \mathrm{n}\Phi_0/\sqrt{\mathrm{Hz}}$, which roughly corresponds to four times the limit set by quantum noise. On the other hand, DC measurements in few Hz range are limited by $1/f$ noise, which leads to a minimum detectable magnetic flux roughly ten times higher.

Margins of improvement in the minimum magnetic flux detectable by SQUID can be gained by reducing the SQUID inductance. This parameter mainly depends on the kinetic contribution (rather than the geometric one), which is a property of the superconducting material used to fabricate the device. Instead, for what concerns the size of the sensor, it is difficult to achieve further reduction of the diameter loop, because the diameter would become comparable or even smaller than the film thickness deposited on top of it. A novel approach that is rapidly growing is to use a focused ion beam of Ga [57], Ne [58] or He [59] to pattern SQUIDs with size of few nanometers. Some work still has to be done in integrating such a small sensor into a scanning probe setup.

1.3 Scanning SQUID Microscopy

Here a general picture of superconductivity [60] is assumed to be known, as well as its first microscopic BCS theory at T = 0 K by Bardeen, Cooper and Schrieffer [61], leading to concepts like Cooper pairs, superconducting gap and excitations of the superconducting ground state. For a detailed treatment of the microscopic theory of superconductivity and other general notions we refer to [62, 63].

1.3.1 Josephson junctions

Josephson junctions take their name from the work by Josephson [64] in 1962, when he predicted that a zero-voltage supercurrent could flow through two superconducting electrodes separated by a thin enough insulating barrier. Josephson provided a microscopic treatment of the quantum mechanical tunneling through the insulating layer, leading to the two famous equations:

$$I_\mathrm{s} = I_\mathrm{c} \sin\delta \tag{1.1}$$

$$\frac{\mathrm{d}\delta}{\mathrm{d}t} = \frac{2\,\mathrm{e}}{\hbar}V = \frac{2\pi}{\Phi_0}V \tag{1.2}$$

where I_s is the supercurrent, I_c is the critical current, δ is the phase difference between the Ginzburg-Landau wavefunction in the two superconducting electrodes, Φ_0 is the magnetic flux quantum and V is the voltage developed across the two electrodes.

The meaning of Eq. (1.1) can be summarized as follows [63]. The current flowing through a Josephson junction is the sum of a non-dissipative term, given by the Cooper-pair current, and a dissipative term, given by the quasiparticle current of not-paired normal electrons. The quasiparticle current, following Ohm's law, is due to the thermal breaking of Cooper pairs. By assuming that the temperature is much lower than the critical value, $0 \ll T \ll T_\mathrm{c}$, thermal fluctuations that could affect the Cooper pairs can be neglected. When no voltage develops across the junction, then the dissipative contribution vanishes and only the tunneling of Cooper pairs contributes to the current. This supercurrent has a limit, set by the critical value I_c. This is known as DC Josephson effect.

Once the current reaches the critical value, then a voltage develops across the junction, whose value is set by the time dependence of the phase difference, as shown by Eq. (1.2). The current through the junction becomes an AC current, with amplitude I_c and frequency $2\mathrm{e}V/h$. This is known as AC Josephson effect.

As already mentioned, the derivation from Josephson regarded two superconducting electrodes separated by a thin insulating barrier. However, AC and DC Josephson effects are way more general and take place when two superconducting electrodes are connected through a weak link. Three types of weak link can be distinguished: S-I-S, where the weak link is given by a thin insulating layer; S-N-S, where a normal metal shows weak superconductivity due to the proximity effect by the strong superconducting electrodes; S-c-S, where two regions of a single superconducting layer are linked by a narrow constriction. The latter is known as Dayem bridge [65] and is the type of Josephson junction that will be discussed here.

The condition required for the coherent transmission of Cooper pairs from one strongly superconducting region to the other is that $L \leq \xi$, where L is the maximum dimension of the weak constriction and ξ is the temperature dependent coherence length of the superconducting material. The Josephson effect can be derived in the framework of the Ginzburg-Landau theory. In the following only few steps will be mentioned, while for a detailed treatment we refer to [62, 63].

The Ginzburg-Landau theory is a phenomenological theory that treats the second-order phase transition from normal state to superconducting state by introducing a macroscopic complex quantity, the order parameter $\psi(\vec{r})$, which describes the ordering reached due to the transition from the disordered normal state for $T > T_\mathrm{c}$ to the ordered superconducting state for $T < T_\mathrm{c}$. The order parameter at a certain temperature T is linked to the Cooper pair density by:

$$n_\mathrm{Cooper} = |\psi(\vec{r})|^2 \tag{1.3}$$

Let's consider the simplified case of a bulk semi-infinite superconductor, in absence of magnetic fields or gradients, in the halfplane $x > 0$. Then, calling ψ_∞ the order parameter for the superconductor ideally far from any surface effect, $\psi(x)$ obeys the equation:

$$-\xi_\mathrm{GL}^2(T)\frac{\mathrm{d}^2\psi(x)}{\mathrm{d}x^2} + \frac{|\psi(x)|^2}{|\psi_\infty|^2}\psi(x) = \psi(x) \tag{1.4}$$

The superconducting electrodes are assumed to be in equilibrium, so $\psi/\psi_\infty = 1$ and a dephasing ϕ is taken into account between the two sides of the constriction ($x = 0, L$). The solution of Eq. (1.4) has to satisfy $\psi/\psi_\infty = 1$ at $x = 0$ and $\psi/\psi_\infty = \mathrm{e}^{\mathrm{i}\phi}$ at $x = L$.

As discussed in [66] by Aslamazov and Larkin, the solution of Eq. (1.4) becomes easier when a short constriction is assumed, $L \leq \xi_\mathrm{GL}$. In this case, the term proportional to ξ_GL^2 dominates over the others and the equation reduces to a second-order derivative. Applying the boundary conditions at the edges of the bridges, the solution can be written as:

$$\frac{\psi(x)}{\psi_\infty} = \left(1 - \frac{x}{L}\right) + \left(\frac{x}{L}\right)\mathrm{e}^{\mathrm{i}\phi} \tag{1.5}$$

This can be seen as the sum of two contributions, the first one representing the spread of the order parameter from the electrode with zero phase and the second one representing the spread of the order parameter from the electrode with phase ϕ. By inserting the solution into the Ginzburg-Landau expression for the current, the Josephson equation Eq. (1.1) is recovered.

RCSJ model

For the aim of this thesis, it is convenient to treat Josephson junctions as circuit components. Their behavior is well explained by the Resistively and Capacitively Shunted Junction (RCSJ) model [67], whose schematics in reported in Figure 1.1, where the junction is shunted in parallel by its self-capacitance C and by an external resistor R. Shunting the junction is needed to avoid a hysteretical behavior: when the bias current I overcomes the critical value I_c, the voltage V across the electrodes abruptly transitions to a non zero value, but returns to zero only at values of I much lower than I_c.

The main assumptions of the RCSJ model are that the Josephson junction parameters do not change in space and that the resistance R is linear below and above the

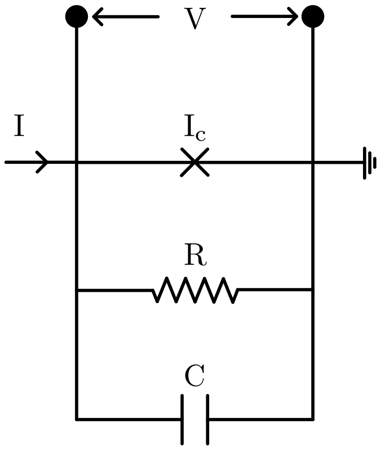

FIGURE 1.1: Equivalent circuit in the RCSJ model of a Josephson junction, with a self-capacitance C and shunted by a resistor R. I is the current flowing through the junction, being I_c its critical value, and V is the voltage across the the two superconducting electrodes.

gap voltage. Furthermore here we discard the contribution due to the current noise source associated to the resistor. By applying Kirchhoff's law, the circuit equation can be written as:

$$C\frac{\mathrm{d}V}{\mathrm{d}t}+\frac{V}{R}+I_c\sin\delta=I \tag{1.6}$$

By substituting V with the expression given by the second Josephson equation, Eq. (1.2), a second-order differential equation for the phase difference is found:

$$\frac{\Phi_0}{2\pi}C\frac{\partial^2\delta}{\partial t^2}+\frac{\Phi_0}{2\pi}\frac{1}{R}\frac{\partial\delta}{\partial t}=I-I_c\sin\delta=-\frac{2\pi}{\Phi_0}\frac{\partial U_J}{\partial\delta} \tag{1.7}$$

where U_J is defined as the tilted washboard potential of the Josephson junction and is given by:

$$U_J\equiv\frac{\Phi_0}{2\pi}\left[I_c(1-\cos\delta)-I\delta\right] \tag{1.8}$$

where the term $\Phi_0/2\pi$ is the Josephson coupling energy.
Eq. (1.7) describes the time evolution (otherwise called dynamics) of the phase δ in a way that recalls the motion of a point-like particle, characterized by a certain mass and friction coefficient, moving on a tilted washed potential. The situation is sketched in Figure 1.2, where the tilted washed potential is plotted as function of δ for three interesting physical cases. When a bias current $I < I_c$ flows through the junction, the cosine-shaped potential U_J tilts proportionally to the current. In this case, called static regime, the particle oscillates back and forth around a minimum of the potential at the junction plasma frequency

$$\omega_{p,I}=\left[\frac{2\pi I_c}{\Phi_0 C}\right]^{1/2}\left(1-\frac{I^2}{I_c^2}\right)^{1/4} \tag{1.9}$$

In the static regime $\partial\delta/\partial t=0$, so no voltage develops across the junction.

The case $I=0$, where no bias current flows through the junction is just a particular case of the static regime. The tilted washed potential becomes flat and the

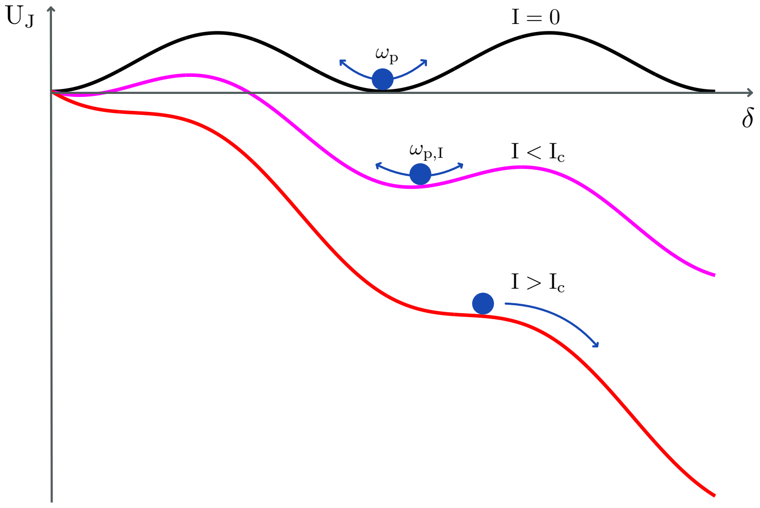

FIGURE 1.2: Sketch of the tilted washed potential U_J as a function of δ, as given by Eq. (1.8), for three cases of interest. The black and magenta curves represent the static regime, where no voltage develops across the junction; the dynamic regime for $I > I_c$ is shown by the red curve, which leads to a DC voltage across the junction proportional to the bias current.

junction plasma frequency reduces to $\omega_p = (2\pi I_c/\Phi_0 C)^{1/2}$.
As the current becomes greater than the critical value, the particle enters the dynamic regime: the washed potential gets so tilted that the local minima of the potential disappear. As a consequence, the phase difference evolves in time and a finite voltage V, proportional to the bias current, develops across the junction.

1.3.2 DC SQUIDs

A SQUID consists of two superconducting semi-rings, connected by two weak links, either S-N-S or S-I-S or Dayem bridges. Well known to be an extremely sensitive detector of magnetic flux, it combines the flow of supercurrent through a single junction with the physical phenomenon of flux quantization.
In the case of a closed superconducting ring, the phase variation must follow certain rules: once it reaches a complete loop around the ring, the phase cannot be discontinuous and needs to go back to the initial value. Yet, if an external magnetic flux is applied to the ring, the flux modifies the phase along the ring. In order for the phase to return to the initial value after a complete turn, only certain values of magnetic flux are allowed to go through the ring: flux is quantized in units of the flux quantum

$$\Phi_0 \equiv \frac{h}{2e} \approx 2.07 \cdot 10^{-15} \quad \text{Wb} \tag{1.10}$$

Two categories of SQUIDs can be distinguished, DC SQUIDs and RF SQUIDs. In the following only DC SQUIDs will be considered. The layout of a possible DC SQUID is shown in Figure 1.3.

The superconducting ring (in grey color) is biased by a DC current I_{bias} while, transverse to the ring plane, an external magnetic field B is applied. In each of the two arms of the SQUID a Josephson Junction (in orange color) is incorporated. Such a junction can be either S-N-S or S-I-S or a constriction junction such as a Dayem

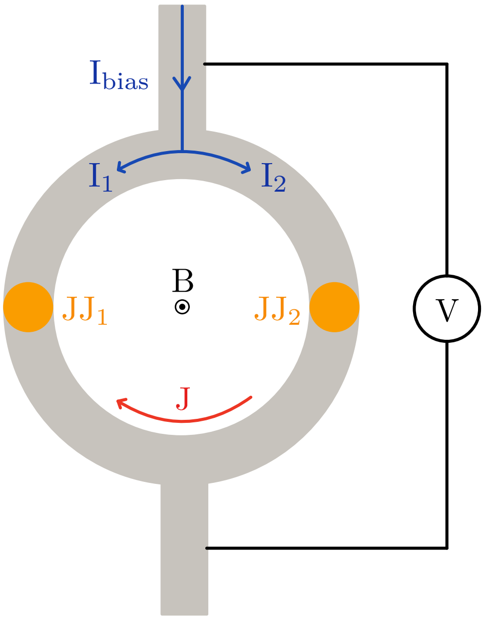

FIGURE 1.3: Schematic design of a SQUID, with two Josephson junctions JJ_1 and JJ_2, biased by a dc current I_{bias}. B is the external applied magnetic field, while J represents the loop current.

bridge. The junctions fix the maximum supercurrent I_c that can flow through the ring to a value determined by the sum of the critical currents of each junction. The value of I_c is periodically modulated by the magnetic flux enclosed inside the SQUID, with a periodicity of one flux quantum Φ_0. The same modulation phenomenon also occurs for the critical current of the junctions, but on a magnetic flux scale much larger than Φ_0, since the area of the junctions is much lower than the internal area of the SQUID. For this reason only the modulation of the critical current of the SQUID will be considered.

There are two ways to detect the field-induced modulation of the critical current. One possibility is to fix the magnetic field and increase the bias current until the junctions switch to the resistive state and a non-zero DC voltage develops across the SQUID. Repeating the measurement at different magnetic fields, the value of the critical current I_c at any applied magnetic flux is obtained. Another possibility is to work in the resistive regime, biasing the SQUID with a current $I_{bias} > I_c$ and reading out the DC voltage across the SQUID as a function of the applied magnetic flux. By detecting a small change in the voltage, it is possible to measure a flux variation typically as low as $10^{-6}\ \Phi_0$. This method is mainly used for DC SQUIDs with overdamped junctions, having a non-hysteretic I-V characteristics. The SQUID directly acts as flux-to-voltage transducer: when I_c is minimum, the voltage is maximum and vice-versa.

Rate equations modeling a DC SQUID

A DC symmetric SQUID (as the one of Figure 1.3) is characterized by two weak links with quite similar geometrical parameters. A quantitative description of this device is provided within the RCSJ model, which was already introduced in the framework of a single Josephson junction: the two junctions are supposed to have critical currents I_{c_1} and I_{c_2} and are coupled in parallel with self-capacitances C_1 and C_2 and shunt resistances R_1 and R_2. Again, as in the previous case, we avoid to take into account the current noise sources I_{N_1} and I_{N_2} associated to the resistors. The SQUID inductance has a geometrical contribution, as well as a kinetic contribution. The latter is relevant only when the linewidth of the superconducting structures is small and the thickness of the device is comparable or smaller than the London penetration depth λ_L. The contributions due to the left and the right arm of the SQUID can be different and are expressed as L_1 and L_2, respectively.

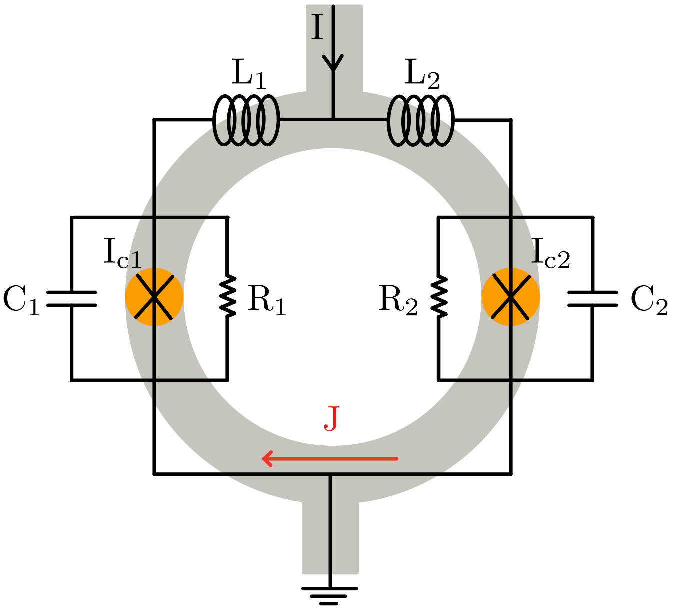

FIGURE 1.4: Equivalent circuit of a DC SQUID in the RCSJ model, where I is the DC bias current, C is the self-capacitance, R is the shunt resistance, L is the inductance and J is the loop current. For matter of simplicity, no current noise source is considered.

The equivalent circuit of a DC SQUID in the RCSJ model is reported in Figure 1.4, overlapped to the geometrical shape of the SQUID loop. The device is quantitatively described by three equations: the first two ones express the currents flowing through the two junctions, according to Kirchhoff's laws, while the last one relates the phase difference of the junctions, the magnetic flux penetrating the SQUID loop and the current J circulating around the ring.
The current through the first junction can be written as half the bias current plus the loop current, $I_1 = I/2 + J$, while the current through the second junction can be written as $I_2 = I/2 - J$. According to the RCSJ model, the equations describing a DC SQUID are [67]:

$$I_1 = \frac{I}{2} + J = I_{c_1}\sin(\delta_1) + \frac{\Phi_0}{2\pi R_1}\frac{\partial \delta_1}{\partial t} + \frac{\Phi_0}{2\pi}C_1\frac{\partial^2 \delta_1}{\partial t^2} \quad (1.11a)$$

$$I_2 = \frac{I}{2} - J = I_{c_2}\sin(\delta_2) + \frac{\Phi_0}{2\pi R_2}\frac{\partial \delta_2}{\partial t} + \frac{\Phi_0}{2\pi}C_2\frac{\partial^2 \delta_2}{\partial t^2} \quad (1.11b)$$

$$\delta_2 - \delta_1 = \frac{2\pi}{\Phi_0}(\Phi_a + LJ) = \frac{2\pi}{\Phi_0}\Phi_T \quad (1.11c)$$

where Φ_T is the total flux through the SQUID. This has contributions from the loop current and the applied magnetic flux $\Phi_\mathrm{a} = B \cdot A_\mathrm{eff}$, where A_eff is the effective internal area of the SQUID.

For a further analysis of Eqs. (1.11), it is useful to turn to dimensionless units. Firstly, the average critical current, $I_0 = (I_{c_1} + I_{c_2})/2$, the double parallel resistance of the SQUID, $R = 2R_1R_2/(R_1 + R_2)$ and the average capacitance, $C = (C_1 + C_2)/2$ can be introduced. Then, normalizing the currents to I_0, resistances to R, time to $\tau \equiv \Phi_0/(2\pi I_0 R)$, voltage to $I_0 R$ and magnetic flux to Φ_0, the equations of the DC SQUID transform into:

$$\frac{i}{2} + j = \sin(\delta_1) + \frac{\partial \delta_1}{\partial t} + \beta_\mathrm{c}\frac{\partial^2 \delta_1}{\partial t^2} \tag{1.12a}$$

$$\frac{i}{2} - j = \sin(\delta_2) + \frac{\partial \delta_2}{\partial t} + \beta_\mathrm{c}\frac{\partial^2 \delta_2}{\partial t^2} \tag{1.12b}$$

$$\delta_2 - \delta_1 = 2\pi\left(\frac{\Phi_\mathrm{a}}{\Phi_0} + \frac{1}{2}\beta_\mathrm{L} j\right) \tag{1.12c}$$

Here i and j denote the dimensionless bias and loop currents, respectively, $\beta_\mathrm{c} = 2\pi I_0 R^2 C/\Phi_0$ is the Stewart-McCumber parameter, while $\beta_\mathrm{L} = 2LI_0/\Phi_0$ is the screening parameter.

In the most general case in which an asymmetry in the SQUID is introduced, Eqs. (1.12) become:

$$\frac{i}{2} + j = (1-\alpha_\mathrm{I})\sin(\delta_1) + (1-\alpha_\mathrm{R})\frac{\partial \delta_1}{\partial t} + \beta_\mathrm{c}(1-\alpha_\mathrm{C})\frac{\partial^2 \delta_1}{\partial t^2} \tag{1.13a}$$

$$\frac{i}{2} - j = (1+\alpha_\mathrm{I})\sin(\delta_2) + (1+\alpha_\mathrm{R})\frac{\partial \delta_2}{\partial t} + \beta_\mathrm{c}(1+\alpha_\mathrm{C})\frac{\partial^2 \delta_2}{\partial t^2} \tag{1.13b}$$

$$\delta_2 - \delta_1 = 2\pi\left(\frac{\Phi_\mathrm{a}}{\Phi_0} + \frac{1}{2}\beta_\mathrm{L} j\right) \tag{1.13c}$$

where α_I, α_R and α_C parametrize the asymmetries in the junction critical currents, resistances and capacitances, respectively. Let's start studying the static solutions of a DC SQUID with symmetric junctions. In this case, the derivatives with respect to normalized time vanish and the Eqs. (1.13) become:

$$\frac{i}{2} + j = \sin(\delta_1) \tag{1.14a}$$

$$\frac{i}{2} - j = \sin(\delta_2) \tag{1.14b}$$

$$\delta_2 - \delta_1 = 2\pi\left(\frac{\Phi_\mathrm{a}}{\Phi_0} + \frac{1}{2}\beta_\mathrm{L} j\right) \tag{1.14c}$$

Eq. (1.14c) further simplifies when a negligible SQUID inductance is assumed ($\beta_\mathrm{L} \ll 1$): $\delta_2 - \delta_1 = 2\pi\Phi_\mathrm{a}/\Phi_0$. Solving the equation system, the current flowing through the SQUID reads as:

$$i = \sin(\delta_1) + \sin(\delta_2) = \sin(\delta_1) + \sin\left(\delta_1 + 2\pi\frac{\Phi_\mathrm{a}}{\Phi_0}\right) \tag{1.15}$$

The maximum current, expressed in absolute units, is found introducing $\delta_1^* = \delta_1 + \pi\Phi_\mathrm{a}/\Phi_0$ and maximizing i with respect to δ_1^*:

$$I_\mathrm{c}\left(\frac{\Phi_\mathrm{a}}{\Phi_0}\right) = 2I_0 \cdot \left|\cos\left(\pi\frac{\Phi_\mathrm{a}}{\Phi_0}\right)\right| \tag{1.16}$$

Therefore, in the case of symmetric junctions and negligible inductance, the critical current of the SQUID modulates between 0 and $2I_0$, with the period of a flux quantum. A reduction of the modulation depth occurs when the inductance is no longer negligible or when an asymmetry in the SQUID is introduced. For further information about the influence of inductance on the performance of DC SQUIDs, we refer to the next session.
For an asymmetric SQUID with negligible inductance, an expression for the critical current is reached starting from Eqs. (1.13) and maximizing i with respect to δ_1 and δ_2. In absolute units we find that:

$$I_\mathrm{c}\left(\frac{\Phi_\mathrm{a}}{\Phi_0}\right) = I_0\sqrt{2 + 2\alpha_\mathrm{I}^2 + 2(1-\alpha_\mathrm{I}^2)\cos\left(2\pi\frac{\Phi_\mathrm{a}}{\Phi_0}\right)} \tag{1.17}$$

where α_I is the ratio of the minimum and the maximum critical current. In this case the modulation depth is reduced proportionally to α_I, since the critical current modulates between $\alpha_\mathrm{I}I_0$ and $2I_0$.
So far, the response of a DC SQUID in the superconducting state was illustrated. Now the resistive regime of a symmetric SQUID, with a nonzero DC voltage V across the junctions, will be considered. Solving Eqs. (1.12) we see that the modulation in I_c directly transfers into a modulation of V. The solutions now are strongly dependent on the values of β_c and β_L. When $\beta_\mathrm{L} \ll 1$, the equation system becomes:

$$\frac{i}{2} + j = \sin(\delta_1) + \frac{\partial\delta_1}{\partial t} + \beta_\mathrm{c}\frac{\partial^2\delta_1}{\partial t^2} \tag{1.18a}$$

$$\frac{i}{2} - j = \sin(\delta_2) + \frac{\partial\delta_2}{\partial t} + \beta_\mathrm{c}\frac{\partial^2\delta_2}{\partial t^2} \tag{1.18b}$$

$$\frac{\partial\delta_1}{\partial t} = \frac{\partial\delta_2}{\partial t} \tag{1.18c}$$

Introducing $\delta_1^* = \delta_1 + \pi\Phi_\mathrm{a}/\Phi_0$, the current across the SQUID in absolute units reads as:

$$I = 2I_0\cos\left(\pi\frac{\Phi_\mathrm{a}}{\Phi_0}\right)\sin(\delta_1^*) + \frac{2\Phi_0}{2\pi R}\frac{\partial\delta_1^*}{\partial t} + \frac{2\Phi_0}{2\pi}C\frac{\partial^2\delta_1^*}{\partial t^2} \tag{1.19}$$

In the limit of negligible capacitance ($\beta_\mathrm{c} \ll 1$), the current-voltage characteristic for $I > I_\mathrm{c}$ is given by:

$$V = \frac{R}{2}\sqrt{I^2 - I_\mathrm{c}^2} \tag{1.20}$$

Replacing I_c with the expression reported in Eq. (1.16), we find:

$$V = \frac{R}{2}\sqrt{I^2 - 4I_0^2\cos^2\left(\pi\frac{\Phi_\mathrm{a}}{\Phi_0}\right)} \tag{1.21}$$

Therefore, the DC voltage oscillates with magnetic flux, with a period of one flux quantum, with minima at integer multiples of Φ_0 and maxima at half integer multiples of Φ_0. From the slope $\partial V/\partial\Phi_a$, we can introduce the transfer function of the SQUID as

$$V_\Phi = \max\left|\frac{\partial V}{\partial \Phi_a}\right| \tag{1.22}$$

where maximization is with respect to bias current and flux.

Impact of kinetic inductance on the performance of DC SQUIDs

The SQUID's inductance is determined by the sum of two contributions, a geometrical one and a kinetic one. For a detailed analysis of the geometric inductance for thin-film conductors, we refer to [68]. For the aim of this work, only nanoSQUIDs with loop diameter of few hundreds of nanometers are relevant, for which the geometric inductance offers a negligible contribution. For this reason, in the following only the kinetic inductance will be considered.

Kinetic inductance arises from the kinetic energy stored in the motion of supercurrent charge carriers. It is nonlinear with both current and temperature and, contrary to the geometric self-inductance, it does not couple with a magnetic field.

Here we are interested in analyzing from which parameters the kinetic inductance L_K depends on and how does it influence the current-phase characteristic of a SQUID. As pointed out by many works [69–71], kinetic inductance is in first place a property of the superconducting material used to fabricate the SQUID. In fact, for nanobridges in the dirty limit and for $T \ll T_c$:

$$L_K \propto \frac{\hbar R_{sh}}{k_B T_c} \tag{1.23}$$

where R_{sh}, called sheet resistance, is a parameter characterizing every conductor. R_{sh} is mainly determined by the resistivity of the material, whose typical order of magnitude is $10^{-6}\ \Omega\cdot\text{m}$. Certain disordered superconducting materials, such as TiN [72], NbN [73], $Mo_{79}Ge_{21}$ [71] have a quite high resistivity, which transduces in a high kinetic inductance. On the other hand, Pb [74] and Nb [75] are superconductors well known for having low resistivities, and consequently are reported to have low values of L_K.

Kinetic inductance depends not only on material properties, but also on the geometry of the weak link. In fact, as described by [70, 71], L_K scales with the dimensions of the weak link in the following way:

$$L_K \propto \frac{l}{w\cdot th} \tag{1.24}$$

where l is the length, w the width and th the thickness. Anticipating some concepts that will be covered in the next chapter, the SQUIDs of interest for this work, by construction, offer a limited capability of playing with the geometrical parameters of the weak link. So the possibility to tune the inductance is mostly offered by the choice of the material used to fabricate the SQUID.

When a finite, non negligible β_L is introduced, Eq. (1.14c) for the phase difference gets modified by a term proportional to the product $\beta_L j$. In this case, it is not possible to write a general, analytic expression for $I_c(\Phi_a)$, unless restrictions are imposed to some of the SQUID parameters. However, numerical solutions, reported in Figure 1.5, show that an increasing screening parameter leads to a monotonic decrease of the critical current modulation $\Delta I_c/I_{c,max}$ [67]. When $\beta_L \ll 1$, the typical

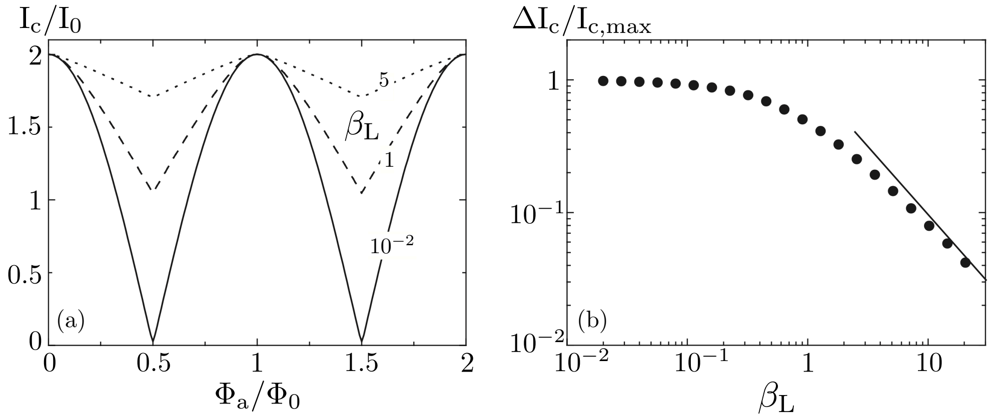

FIGURE 1.5: Impact of the kinetic inductance on the critical current modulation of the SQUID. (a) critical current plotted as function of applied magnetic flux, for three different values of the screening parameter β_L, which depends on the kinetic inductance of the SQUID; higher values of β_L lead to a reduced modulation depth and to a more triangular-shaped behavior of $I_c(\Phi_a)$. (b) Modulation depth $\Delta I_c/I_{c,max}$ as function of the screening parameter β_L. Starting from $\beta_L \simeq 3$, data can be fitted with a β_L^{-1} function. Image adapted from [67].

sinusoidal behavior of $I_c(\Phi_a)$ is found, with the periodicity of one flux quantum and a modulation depth of $2I_0$. Already when $\beta_L = 1$, which means $L = \Phi_0/2I_0$, the critical current modulates by 50%, and, for $\beta_L \gg 1$, $\Delta I_c/I_{c,max}$ decreases as $1/\beta_L$. Moreover, for $\beta_L \gg 1$, the sinusoidal behavior of $I_c(\Phi_a)$ progressively transforms into a triangular-shaped behavior. In the next chapter, it will be possible to see this phenomenon when comparing the I-V characteristic of Pb SQUIDs (with low screening parameters) to the I-V characteristic of SQUIDs made of MoGe, which has a much higher kinetic inductance.

An explanation for the monotonic decrease of the modulation depth proportional to $1/\beta_L$ can be found from the periodic response of the SQUID with the flux, with the applied flux $\Phi_0/2$ corresponding to the largest circulation current $J = \Phi_0/2L$, or in dimensionless units, $j = 1/\beta_L$. The minimum critical current turns out to be of the order of $2(I_0 - J)$, therefore $\Delta I_c/I_{c,max} \approx j \approx 1/\beta_L$ for $\beta_L \gg 1$.

1.3.3 SPM approach with SQUIDs on planar substrates

As mentioned in Sec. 1.2, SSM combines the high sensitivity of SQUIDs to magnetic flux with high spatial resolution to achieve local magnetic investigation of samples of interest. A key element to improve spatial resolution and sensitivity to local magnetic field sources is the miniaturization of SQUID structures. This process of shrinking the dimensions of the SQUID is by itself not enough if not matched to a very short distance between sensor and sample. Ideally, the working distance at which scanning over the surface should be of the same order or smaller than the size of the SQUID or the pick-up loop. A few strategies have been developed over the years. Here the approach which started in the 1990s based on SQUIDs on planar substrates will be briefly introduced, firstly mentioning the strategy based on sensing local fields by a miniaturized pick-up loop and then considering a different approach where local magnetic signals are coupled directly to a micrometer sized SQUID loop.

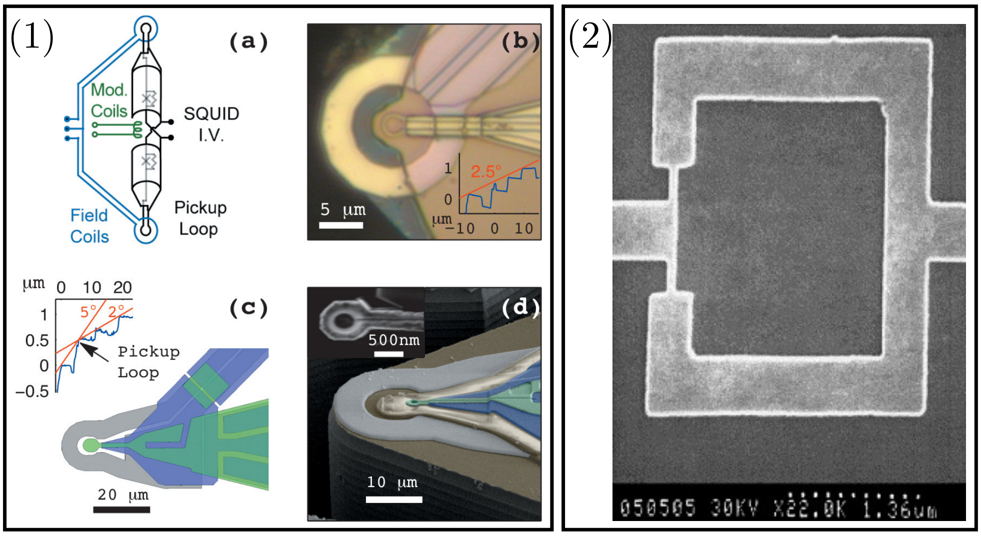

FIGURE 1.6: Panel (1) describing the design of a counterwound integrated scanning susceptometer, from Ref. [76]. (a) Diagram of the SQUID susceptometer; (b) Optical microscope picture of the pick-up loop of the SQUID (the inside ring), surrounded by the outer field coil; (c) SQUID design where focused ion beam etching is used to define the pick-up loop; (d) Scanning Electron Microscope picture of the sensor. Panel (2), from Ref. [77], shows a Scanning Electron Microscope image of a Nb micro-SQUID, having a diameter of 2 μm and linewidth of 300 nm.

Let's start from the first strategy, the one based on SQUIDs with an integrated pickup loop. Lot of references from the 1990s to nowadays can be cited, since this approach has led to tens of remarkable works, with performance improved over the years. For further reading we refer to [1, 76, 78–81].

Different techniques have been followed to achieve control of the sensor to sample distance, including fabricating SQUIDs on top of a Si cantilever; however, for a general understanding of the method, the discussion will be limited to the geometry shown in Panel (1) of Figure 1.6, from the the work in Ref. [76]. The main idea is to spatially separate the SQUID sensor with its Josephson junctions, junction shunts and modulation coils from the pick-up loop and its field coil, which is located as close as possible to the sample under investigation. The separation in space between SQUID and pick-up loop is typically of the order of a millimeter and allows to reduce the cross coupling between modulation coil and pick-up loop/field coil and at the same time allows the pick-up loop to be optimized for coupling to the sample.

The primary pick-up loop captures flux over the region of interest near the sample, while a current through the primary field coil is used to apply a local field. It is often desirable to null the SQUID response to the applied field, since in this way the signal only depends on the magnetic response of the sample to the applied field. This is usually done by flowing the same current through a secondary field coil around a counterwound secondary pick-up loop, which is placed opposite to the primary one symmetrically with respect to the SQUID. This is shown in Figure 1.6(1a). The connection between SQUID and pick-up loops is provided by well shielded superconducting thin film leads.

The Josephson junctions composing the SQUID ring are designed in such a way the critical current is $\Phi_0/2L$. By doing so, the screening parameter $\beta_L \simeq 1$ and the sensor achieves the optimal flux noise. The pick-up loop area is chosen to be as big as

possible, compatibly with the spatial resolution needed for the sample investigation. Sub-micrometer diameter loop sizes have been realized [1], but typical diameters are about few micrometers big.
Figure 1.6(1b-d) show another important feature of these SQUIDs. Tuning the pick-up loop size is not enough to guarantee the required scanning spatial resolution. In fact, this depends as well on the vertical distance between pick-up loop and sample. To minimize such a distance, the Si substrate is polished (either by cleaving or focused ion beam milling) to form a corner at a distance h of few tens of micrometers away from the center of the primary pick-up loop. The Si chip is then mounted on a holder with small inclination angle α to the sample plane (2 - 5°). In this way the vertical distance between pick-up loop and sample, given by $h \cdot \sin \alpha$), can be around 1 μm or less.
The strategy based on pick-up loops leads to Johnson noise limited performance as good as 0.1 - 0.2 $\mu\Phi_0/\sqrt{\text{Hz}}$ in the mK temperature region and about 1 $\mu\Phi_0/\sqrt{\text{Hz}}$ at 4 K. Scanning applications of such sensors were the study of superconducting vortices in different materials [1, 76], from which relevant informations regarding the superconductors could be extracted, such as coherence length or penetration depth. Moreover, the study of surface magnetic states [82], unpaired spins in metals [83], and edge currents in topological insulators [84].

A second strategy to achieve scanning SQUIDs with good spatial resolution was based on miniaturized Nb and Al SQUID loops with two Dayem bridges [77]. The approach differs from the one based on pick-up loops especially for what concerns the sensor fabrication. The relatively simple SQUID design allows single lithography fabrication process and is compatible with strong miniaturization. For instance, the device presented in Figure 1.6(2) is a scanning SQUID with diameter of 2 μm, but nanometer-size SQUIDs can be fabricated as well [85]. A sensor to sample distance as small as the loop diameter can be obtained in a similar way as described before for the pick-up loops. A possible approach involves the cutting of the Si substrate close to the SQUID device and the coupling of the Si chip to a mechanical tuning fork. Micro-SQUIDs were proven to compatible to crygenic temperature [86, 87] and were applied to investigate basic properties of superconductors [88].

1.3.4 SQUID-on-Tip approach

From last section we got the limitations involving lithographically produced planar SQUIDs on chip. Mainly, the difficulty in fabricating pick-up loop diameters smaller than 100 nm and placing them at a similar or smaller distance from the sample under investigation. This translates into a difficulty in reaching extremely high magnetic and spin sensitivity. For this reason, in the 2000s a lot of research focused on producing SQUIDs, in a configuration that could combine high magnetic flux sensitivity, reduction of sensor size and possibility to scan the sensor few nanometers above the surface of interest, in a similar way to AFM or MFM experiments.
An extremely successful approach to produce SQUIDs suitable for SPM experiments was the one introduced in 2010 by Finkler et al. in the Zeldov group at the Weizmann Institute [2]. The idea behind this technique is to fabricate a SQUID, based on two Dayem bridges, on the apex of a pulled quartz capillary. This device was called SOT. The mechanical pulling defines a unique platform, with a tunable diameter as small as 50 nm, where SQUIDs can be fabricated in a single, self-aligned process without need of any lithographic step. The first device, made of Al, had a diameter of about 200 nm and reported flux sensitivity of 1.8 $\mu\Phi_0/\sqrt{\text{Hz}}$ and spin sensitivity of

65 $\mu_B/\sqrt{\mathrm{Hz}}$. Performance improved rapidly over the years, until the work by Vasuykov et al. [54] reported a 46 nm diameter SOT, made of Pb, with flux sensitivity of 50 $\mathrm{n}\Phi_0/\sqrt{\mathrm{Hz}}$ and single-spin sensitivity of 0.38 $\mu_B/\sqrt{\mathrm{Hz}}$.

To integrate such a nano-SQUID into a scanning probe microscope, the SOT can be physically coupled to a commercial tuning fork [2, 89]. When voltage biased, the tuning fork oscillates, with an amplitude of about 1 nm. The quartz capillary, coupled to the tuning fork, oscillates as well, in a way that depends on stiffness (related to the material and the shape of the tapered part) and how far from the capillary's apex the tuning fork is coupled. The reduction in amplitude and frequency shift of the resonance peak of the tuning fork can be used to obtain a feedback on the sample to sensor distance.

To give the reader an understanding of the potential of this approach, SOT sensors were used to study the lattice [89], pinning and expulsion [90] and dynamics [4] of superconducting vortices; few studies on 2D materials focused on graphene, especially on mapping resonant dissipation from individual atomic defects [5], twist-angle disorder and Landau levels in magic-angle graphene [6] and long-range non-topological edge currents in charge-neutral graphene [7]. Furthermore, imaging analysis of magnetic configurations of individual ferromagnetic nanotubes [91] and of a chiral artificial spin ice system [92] can be mentioned.

Due to the dependence of the superconducting properties on temperature, SQUIDs are excellent thermometers, so they are suitable for local AC thermometry. A requirement for that is to thermally couple the SQUID junctions to the sample under investigation. An advantage offered by the SOT configuration is the possibility to approach the sensor close enough to the sample surface to perform local thermometry. A great example is given by the work of Halbertal [3], where a SOT with thermal sensitivity below 1 $\mu\mathrm{K}/\sqrt{\mathrm{Hz}}$ was reported. Such a sensor was used to perform nanoscale thermal imaging of quantum matter.

A very detailed description of how SOT sensors are fabricated and characterized, together with the implementation of such sensors into a SPM setup will be provided in Chap. 2. In the following, the rate equations for the SOT in its typical electronic setup will be described.

Rate equations for the SOT

In this final theoretical section, we go deeper into the circuit description of the SOT by introducing the typical electric circuit used to measure the SOT response and presenting a simplified analytic solution for the current flowing through the SOT.

As mentioned earlier in the chapter, analytic solution for the current flowing through a DC SQUID is possible only under the assumption that the Stewart-McCumber and screening parameters are respectively $\beta_c \ll 1$ and $\beta_L \ll 1$, which means that capacitance and inductance are negligible. In all other combinations of β_c and β_L, numerical solutions are required; for more explanation about this case we refer to the work by Finkler [93].

In the very simplified model presented in Figure 1.7, the SOT, in orange color, is treated as a single Josephson junction, in blue color, characterized by a critical current I_c and a phase difference δ between the two superconducting electrodes. I_{SOT} denotes the current flowing through the SOT, while R_{SOT} is the resistance and C_{SOT} is the capacitance.

The general circuit used to bias the SOT is shown in black color and consists of:

- V_{bias} is the DC bias voltage.

- R_{bias} is the input bias resistance. Usually in the few kΩ range, it is much higher than all the other resistances in the circuit. For this reason the bias current can be expressed as: $I_{\text{bias}} = V_{\text{bias}}/R_{\text{bias}}$. It is important that R_{bias} is not too high, as Johnson-Nyquist thermal noise associated to a resistor scales with the square root of the resistance. Typical noise for resistors in the kΩ range is less than 10 $\text{nV}/\sqrt{\text{Hz}}$.
- R_s is the external bias shunt resistance, usually in the range of few Ω.
- R_p is the parasitic resistance in series with the SOT, usually in the range of few Ω. It is influenced by the overall resistance of the electrical line, as well as by the contact resistance between the SOT electrodes and the SOT holder.

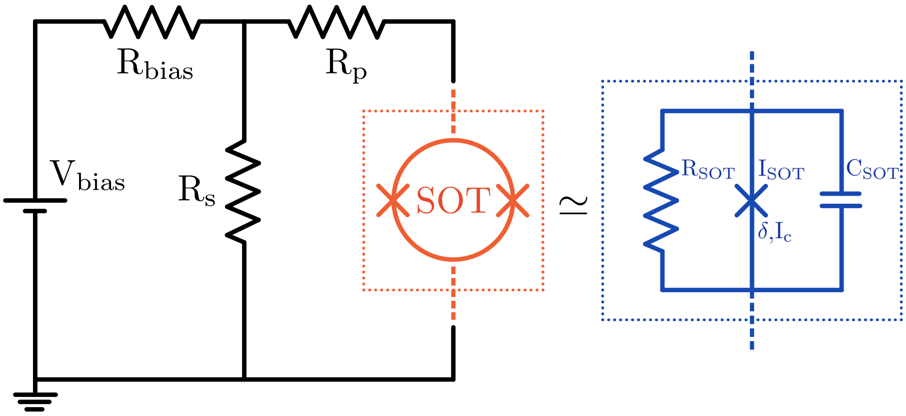

FIGURE 1.7: Diagram reporting the bias circuit for the SOT. The readout component is missing and will be mentioned in Chap. 2. In black the general circuit structure, with bias voltage V_{bias}, bias resistance R_{bias}, shunt resistance R_s and parasitic resistance R_p. The SOT (in orange color), is approximated by a single Josephson junction (in blue color), described by a critical current I_c and a phase difference δ between the two electrodes. I_{SOT} denotes the current flowing through the SOT, while R_{SOT} is the resistance and C_{SOT} is the capacitance.

Together with R_p, the other important parameter which determines the behavior of the SOT is the resistance R_{SOT}. This is influenced by the quasiparticle resistance of the SQUID, R_{quas} and by the short resistance R_{short} of a narrow and thin Au stripe evaporated close to the apex of the quartz pulled capillary. More details about this will follow in Chap. 2. R_{SOT} is given by the parallel of R_{quas} and R_{short}, so:

$$R_{\text{SOT}} = \frac{R_{\text{quas}} R_{\text{short}}}{R_{\text{quas}} + R_{\text{short}}} \tag{1.25}$$

In the following analysis, an expression for the current flowing through the SOT as function of the bias voltage is derived. Initially, Kirchhoff's laws are used to split the behavior of the SOT depending on whether the current flowing through the SOT is smaller or larger than the critical current [93].

For $I_{\mathrm{SOT}} \leq I_{\mathrm{c}}$:

$$V_{\mathrm{s}} = I_{\mathrm{bias}} \frac{R_{\mathrm{s}}(R_{\mathrm{p}} + R_{\mathrm{SOT}})}{R_{\mathrm{p}} + R_{\mathrm{s}} + R_{\mathrm{SOT}}} \approx I_{\mathrm{bias}} \frac{R_{\mathrm{s}} R_{\mathrm{p}}}{R_{\mathrm{p}} + R_{\mathrm{s}}} \tag{1.26a}$$

$$I_{\mathrm{SOT}} = \frac{V_{\mathrm{bias}}}{R_{\mathrm{bias}}} \frac{R_{\mathrm{s}}}{R_{\mathrm{p}} + R_{\mathrm{s}}} \tag{1.26b}$$

where V_{s} is the voltage drop across the shunt resistance. The two equations describe the SOT in its superconducting state: R_{SOT} can be approximated as null, while I_{SOT} follows a linear behavior as function of V_{bias}, with an angular coefficient given by the parallel between parasitic and shunt resistances.

For $I_{\mathrm{SOT}} > I_{\mathrm{c}}$:

$$V_{\mathrm{s}} = (I_{\mathrm{bias}} - I_{\mathrm{SOT}}) R_{\mathrm{s}} \tag{1.27a}$$

$$V_{\mathrm{s}} = I_{\mathrm{SOT}}(R_{\mathrm{p}} + R_{\mathrm{SOT}}) - R_{\mathrm{SOT}} I_{\mathrm{c}} \sin\delta \tag{1.27b}$$

$$\frac{\hbar}{2\,\mathrm{e}} \frac{\partial\delta}{\partial t} = (I_{\mathrm{SOT}} - I_{\mathrm{c}} \sin\delta) R_{\mathrm{SOT}} \tag{1.27c}$$

where in the last case the connection between voltage drop and time evolution of the phase difference is provided by Josephson equation, Eq. 1.2.
Combining Eqs. 1.27a and 1.27b, we find that:

$$I_{\mathrm{SOT}}(R_{\mathrm{p}} + R_{\mathrm{SOT}} + R_{\mathrm{s}}) = I_{\mathrm{bias}} R_{\mathrm{s}} + R_{\mathrm{SOT}} I_{\mathrm{c}} \sin\delta \tag{1.28}$$

This leads to an expression for the current flowing through the SOT:

$$I_{\mathrm{SOT}} = \frac{I_{\mathrm{bias}} R_{\mathrm{s}} + R_{\mathrm{SOT}} I_{\mathrm{c}} \sin\delta}{R_{\mathrm{p}} + R_{\mathrm{s}} + R_{\mathrm{SOT}}} \tag{1.29}$$

By inserting Eq. 1.29 into Eq. 1.27c, the following differential equation for the phase difference as function of the other circut parameters is obtained:

$$\frac{\hbar}{2\,\mathrm{e}} \frac{\partial\delta}{\partial t} = \left[\frac{I_{\mathrm{bias}} R_{\mathrm{s}} + R_{\mathrm{SOT}} I_{\mathrm{c}} \sin\delta - I_{\mathrm{c}} \sin\delta (R_{\mathrm{p}} + R_{\mathrm{s}} + R_{\mathrm{SOT}})}{R_{\mathrm{p}} + R_{\mathrm{s}} + R_{\mathrm{SOT}}} \right] R_{\mathrm{SOT}} \tag{1.30}$$

This can be rearranged as:

$$\frac{\hbar}{2\,\mathrm{e}} \frac{\partial\delta}{\partial t} + \frac{R_{\mathrm{SOT}}(R_{\mathrm{p}} + R_{\mathrm{s}})}{R_{\mathrm{p}} + R_{\mathrm{s}} + R_{\mathrm{SOT}}} I_{\mathrm{c}} \sin\delta - \frac{R_{\mathrm{SOT}} R_{\mathrm{s}}}{R_{\mathrm{p}} + R_{\mathrm{s}} + R_{\mathrm{SOT}}} I_{\mathrm{bias}} = 0 \tag{1.31}$$

By introducing the parameter $\eta = R_{\mathrm{SOT}}(R_{\mathrm{p}} + R_{\mathrm{s}})/(R_{\mathrm{p}} + R_{\mathrm{s}} + R_{\mathrm{SOT}})$ and multiplying Eq. 1.31 times $1/\eta$, we obtain:

$$\frac{\hbar}{2\,\mathrm{e}\eta} \frac{\partial\delta}{\partial t} + I_{\mathrm{c}} \sin\delta - I_{\mathrm{bias}} \frac{R_{\mathrm{s}}}{R_{\mathrm{p}} + R_{\mathrm{s}}} = 0 \tag{1.32}$$

which represents a differential equation of the form $a\partial y/\partial t + b \sin y - c = 0$, where $a = \hbar(R_{\mathrm{p}} + R_{\mathrm{s}} + R_{\mathrm{SOT}})/2\,\mathrm{e}R_{\mathrm{SOT}}(R_{\mathrm{p}} + R_{\mathrm{s}})$, $b = I_{\mathrm{c}}$ and $c = I_{\mathrm{bias}} R_{\mathrm{s}}/(R_{\mathrm{p}} + R_{\mathrm{s}})$.

The analytic solution of Eq. 1.32 is known and is of the kind:

$$y(t) = 2\tan^{-1}\left[\frac{b + \sqrt{c^2 - b^2}\tan\left(\frac{\sqrt{c^2-b^2}}{2a}t\right)}{c}\right] \tag{1.33}$$

The mathematical development for this equation is explained in details in [93] and goes beyond the purpose of this section. Briefly, Eq. 1.33 provides a solution for the phase difference δ and its time evolution $\partial\delta/\partial t$. By inserting these results in Eq. 1.32, a time dependent solution for I_{SOT} is achieved.
By averaging the solution over one period $[0, 2\pi]$, a final expression for the average current through the SOT, as a function of V_{bias}, can be written:

$$I_{\mathrm{SOT}}(V_{\mathrm{bias}}) = \begin{cases} \frac{V_{\mathrm{bias}}}{R_{\mathrm{bias}}}\frac{R_{\mathrm{s}}}{R_{\mathrm{p}}+R_{\mathrm{s}}} & \text{if } \frac{V_{\mathrm{bias}}}{R_{\mathrm{bias}}}\frac{R_{\mathrm{s}}}{R_{\mathrm{p}}+R_{\mathrm{s}}} < I_{\mathrm{c}}, \\ \frac{V_{\mathrm{bias}}}{R_{\mathrm{bias}}}\frac{R_{\mathrm{s}}}{R_{\mathrm{p}}+R_{\mathrm{s}}} - \frac{R_{\mathrm{SOT}}}{R_{\mathrm{p}}+R_{\mathrm{s}}+R_{\mathrm{SOT}}}\sqrt{(\frac{V_{\mathrm{bias}}}{R_{\mathrm{bias}}}\frac{R_{\mathrm{s}}}{R_{\mathrm{p}}+R_{\mathrm{s}}})^2 - I_{\mathrm{c}}^2} & \text{if } \frac{V_{\mathrm{bias}}}{R_{\mathrm{bias}}}\frac{R_{\mathrm{s}}}{R_{\mathrm{p}}+R_{\mathrm{s}}} > I_{\mathrm{c}} \end{cases} \tag{1.34}$$

The two equations can be used to analytically fit the measured *I*-*V* characteristic of a SOT. This is reported in Figure 1.8, where the black curve corresponds to the experimental data of a 180 nm diameter SOT made of Nb and the red curve is the fit according to Eq. 1.34. Circuit elements $R_{\mathrm{bias}} = 6100\ \Omega$ and $R_{\mathrm{s}} = 3\ \Omega$ are assumed as fixed, $I_{\mathrm{c}} = 48.2\ \mu$A is extracted from the data, while R_{p} and R_{SOT} are the fitting parameters. The expression from Eq. 1.34 well fits the experimental data, with an outcoming parasitic resistance of $R_{\mathrm{p}} = 0.5\ \Omega$ and a SOT resistance of $R_{\mathrm{SOT}} = 5.5\ \Omega$.

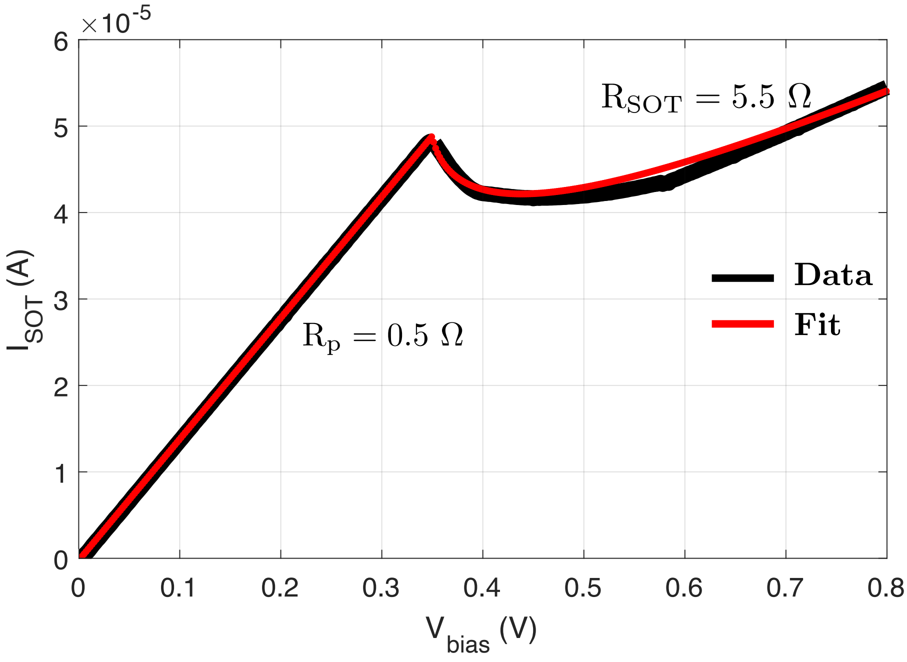

FIGURE 1.8: Analytic fit of the *I*-*V* characteristic of a 180 nm diameter SOT, made of Nb. Data are reported in black color, while the fit is shown in red color. To analytically fit the data, Eq. 1.34 is used, with fitting parameters R_{p} and R_{SOT}. Fit is in good agreement with the data, with parasitic resistance $R_{\mathrm{p}} = 0.5\ \Omega$ and SOT resistance $R_{\mathrm{SOT}} = 5.5\ \Omega$.

Few further comments regard the single junction approach followed in this section. By comparing the expressions of Eqs. 1.27c and 1.6, it is immediate to get that in this treatment the SOT capacitance contribution proportional to $C_{\mathrm{SOT}}\partial^2\delta/\partial t^2$ was assumed to be negligible. This means that the RCSJ model is reduced to a more simplified RSJ model. Recalling the definition of the Stewart-McCumber parameter, $\beta_{\mathrm{c}} = 2\pi I_{\mathrm{c}} R_{\mathrm{SOT}}^2 C_{\mathrm{SOT}}/\Phi_0$, a negligible capacitance is equivalent to the case $\beta_{\mathrm{c}} \to 0$. Physically this is the case of an extremely overdamped SOT, with no hysteresis in the I-V characteristic: this means that SOT transitions from the normal state back to the superconducting state at a current equal to the critical current (instead of at a lower one).

In a non-ideal SOT case, the capacitance is still quite low and the β_{c} parameter is mainly influenced by the values of I_{c} and R_{SOT}. A way to keep $\beta_{\mathrm{c}} \ll 1$ is to decrease the critical current of the SOT, but the most effective action is to decrease the SOT resistance. This can be achieved by decreasing the resistance R_{short} of the Au-stripe short in parallel to the quasiparticle normal-state resistance of the SOT.

Chapter 2

Sensors

This chapter focuses on fabrication and characterization of the SOT sensors, and their integration in a SPM setup. Contents are articulated in six sections.

First section explaines the preparation steps required before coating the capillaries with superconducting material. This part is followed by the description of the fabrication of the SOT sensors, made of Pb, MoGe and Nb by the use of different deposition techniques. Third and fourth sections introduce the test measurement setup and then report I-V characteristics and noise measurements for SOTs made of the three materials of interest.

In the fifth section, we analyze the advantages and drawbacks offered by Pb, MoGe and Nb and present a guide about which material should be used according to the requirements imposed by the SPM experiment.

Final part focuses on the integration of the SOT sensor into a SPM setup, and the coupling of the SOT to a qPlus mechanical resonator.

2.1 Preparation of quartz capillaries

The SOT fabrication consists on defining a SQUID, composed by two superconducting electrodes and a ring with two Josephson junctions enclosed in it, on the apex of a quartz capillary. Before coating the capillary with the desired superconducting material, few initial steps are required. Laser-pulling the capillary defines a sharp tip, with tunable diameter, which serves as a platform to define the superconducting ring. Furthermore, a way to hold the capillary on place and provide electrical contact to the two superconductive electrodes is needed.

2.1.1 Laser-pulling quartz capillaries

The first fabrication step is laser-pulling the quartz capillaries. It is of primary importance, since it defines shape and length of the tapered part, and its final diameter. The tip diameter automatically determines the effective diameter of the SQUID that will be defined on top. This parameter sets the spatial resolution of the sensor for magnetic imaging applications.

Laser-pulling in our case was performed using the commercial puller Sutter Instrument P2000. A full description of the pulling parameters, a guide about how to set them according to the goal, and a book of recipes are reported in Appendix A. For this reason, here only few important concepts are mentioned.

The key feature of laser-pulling is to uniformly warm up the outer surface of the pipette and pull it from opposite sides until two perfectly equal sharp pipettes are achieved. The way the capillary is warmed up and the strength of the mechanical pulling action determine the final diameter of the tip. Values ranging from few tens

to few hundreds of nanometers can be obtained. The process maintaines the aspect ratio of the capillary, which means that the proportion between wall width and outer diameter doesn't change.
Two types of quartz capillaries were used in this study. Figure 2.1(a) shows a commercial pipette, with inner diameter (ID) of 0.5 mm and outer diameter (OD) of 1 mm. The relatively big wall thickness of 250 μm is required when quartz capillaries with diameter as small as 50 nm are aimed.

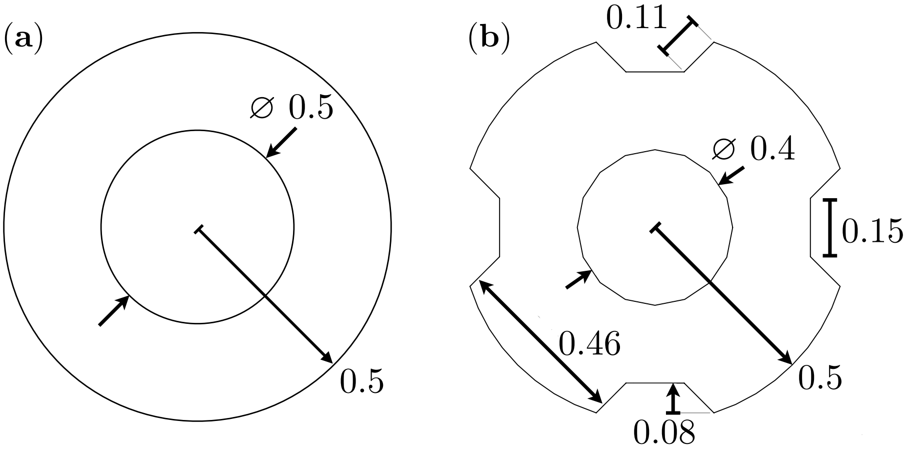

FIGURE 2.1: Cross section of the quartz capillaries used in our experiments. All dimensions are expressed in mm units. (a) Standard pipette, with inner diameter (ID) 0.5 mm and outer diameter (OD) 1 mm. (b) Custom 4-grooves capillary, with ID 0.4 mm and OD 1 mm. Grooves are 80 μm deep and 150 μm wide and they are disposed symmetrically.

Despite easy to pull with small final diameter, uniformly circular capillaries are not feasible for fabricating SOTs with diameter below 100 nm. A challenge is found in maintaining a gap between the superconducting leads along the pipette. In fact, when the pipette is coated with the superconducting material, as the diameter of the pipette is reduced, the gap size shrinks proportionally, leading to formation of electrical shorts and extra undesired Josephson junctions between the leads.
For this reason, we have designed quartz capillaries enclosing four symmetric grooves along its length. The cross section of such a pipette is showed in Figure 2.1(b). Once pulled, the grooves maintain their original shape, with the size scaling down with the tip diameter. While coating the capillary with the superconducting material, the groove acts as a physical barrier and provides shadowing for the material, contributing to preserve a gap in between the electrodes. To this aim, two grooves on opposite sides, aligned to the two superconducting gaps, would be enough. However, pulling a pipette with only two opposite grooves would provide an oval cross-sectional area SOT. Since this sensor is thought to be used as a magnetometer in a scanning experiment, a circular cross section is preferable. That is obtained by designing four symmetric grooves.
It is worth to mention that grooves offer the additional advantage of shrinking the effective width and length of the two weak links created on the apex of the capillary. This influences some important parameters of the SQUID, such as critical current, Stewart-McCumber parameter and kinetic inductance, which could lead to improved magnetic field/flux noise sensitivity and wider modulation depth. Therefore, customizing the geometry of the grooves with different depth and width can be used to tune the properties of the sensors.

2.1.2 Evaporation of Au electrodes and short

After the pulling process, the sharp tips are cut by a diamond scriber to a length of 18 mm and inserted into a grid made of brass with eight slots. The grid, designed with the commercial software Solidworks, is reported in Figure 2.2. This grid has the particularity of serving a double purpose. In first place it safely holds and stores the capillaries; moreover, it acts as a shadow mask for the deposition of the Au electrodes on opposite sides along the body of the pipette. To prevent overlap of the two electrodes, the slit on both sides has a limited width of 400 μm. The deposition of the electrodes is done in a high vacuum chamber by using e-beam evaporation. The final layer is composed by 5 nm Ti / 50 nm Cu / 20 nm Au and is symmetric on both sides. When working with four-grooves pipettes, it is important to fix the pipette in such a way one groove is perfectly aligned to the center of the slit. The electrodes are deposited only on the whole body length of the pipette, while the tapered part is protected by a mask.

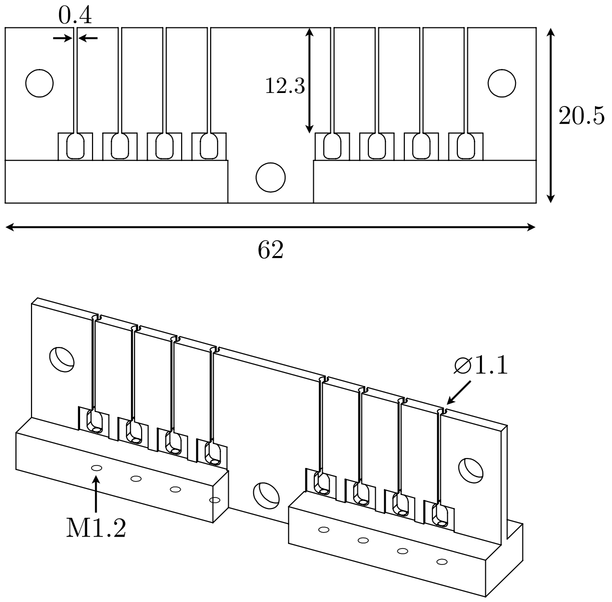

FIGURE 2.2: Schematic Solidworks 3D drawing of the grid used to store the capillaries and deposit Au electrodes and short. All dimensions are expressed in mm units. Capillaries are hold on place at the base by kapton tape. The 0.4 mm wide slits on opposite sides act as a shadow mask for the evaporation of Au electrodes along the body of the pipette, while the sharp tip is protected by an additional mask.

As a last step, pipettes are rotated by 90° and a thin and narrow Au layer short is deposited close to the tip apex. As explained in Sec. 1.3.4, this layer acts as a resistive shunt between the superconducting leads, in parallel to the SOT, and allows to tune the normal metal state resistance, R_{SOT}. The value of R_{SOT} influences β_c and determines the electrical response of the SOT when transitioning from superconducting to normal state. Moreover, the short protects the SOT from static discharge while the device is at room temperature.

The resistance of the short is a function of its geometrical parameters. The length is set by the pipette shape and depends on the distance of the short from the tip apex. The width can be changed by using different evaporation masks and the thickness can be tuned with very good precision.

The process is sketched in Figure 2.3(a), where only the tapered part of the pipette is shown. The mask, in grey color, has a tunable width, typically set to 100 μm. The center of the short is placed at a distance of 350 μm from the tip apex, while the evaporated thickness is 2 nm Ti / 5 - 10 nm Au. To set the position of the short, a M1.2 screw placed at the bottom of the grid is used to push the pipette upwards and hold it on place. By using an optical microscope, it is straightforward to align the tip apex with respect to the evaporation mask, with a precision of $\pm$ 10 μm. Figure 2.3(b) shows an optical microscope picture of a four-grooves quartz capillary, coated with a 2 nm Ti / 6 nm Au short, placed at 340 μm from the tip apex. On the right side, a more resolved Scanning Electron Microscope (SEM) picture is reported. The combination of the short geometrical parameters provide a typical R_{SOT} of about 5 - 10 Ω.

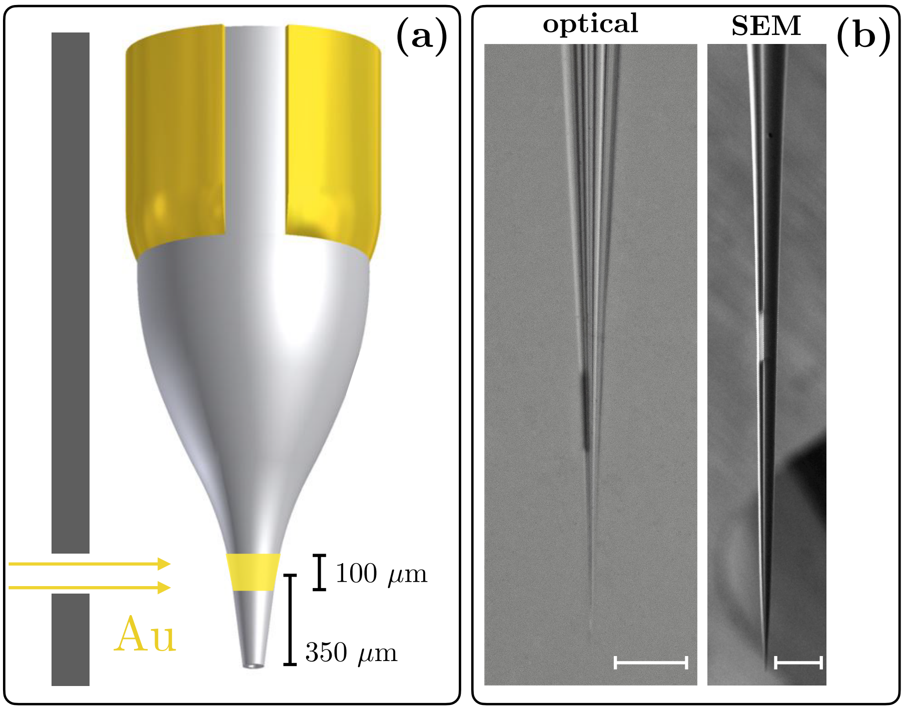

FIGURE 2.3: (a) Schematic drawing of the Au short deposition. A 100 μm wide mask is used for e-beam evaporation of a thin and narrow Ti/Au layer. Typically the center of the short is placed 350 μm far from the tip apex and the short thickness is 2 nm Ti / 5 - 10 nm Au. (b) Optical microscope and SEM pictures of a 2 nm Ti / 6 nm Au thick short. Both scale bars correspond to 100 μm. The short in the optical microscope picture is placed at about 340 μm from the tip apex, while the one in the SEM picture at about 1 mm distance.

2.1.3 Indium coating

At this stage, a batch of 8 or 16 tips with similar diameter and Au short resistance is achieved. The last preparation step before defining the SQUID is to fix a capillary on its holder and provide electrical contact to the evaporated Au electrodes and minimize the contact resistance.

The 3D rendering of the SOT holder is reported in Figure 2.4. The capillary is slided

inside the circular groove of a titanium holder, oriented in such a way one Au electrode is facing the holder body and the other one is pointing upwards and is electrically uncoupled from the holder. The pipette is clamped by two conductive springs. The bottom one, welded to the titanium body, is electrically connected to the lower SOT electrode; the top spring is insulated from the holder body and provides electrical contact just to the top SOT electrode. A dedicated screw allows to short bottom and top electrodes, as a safety procedure while not measuring. Two vertical supports are suited for the integration of an additional component, which couples the tip to a qPlus mechanical resonator (see Sec. 2.6.1).
As mentioned in Sec. 1.3.4, the SOT parasitic resistance depends on the overall electrical resistance of the line, as well as on the contact resistance between the SOT Au electrodes and the holder. Especially when using capillaries with grooves, the electrical contact between springs and Au electrodes is not optimal, leading to an unconsistent resistance of several Ohm. The consequence of high resistance and lack of consistency is that tips with similar R_{SOT} show a different response.
To improve the contact between springs and Au electrodes, a layer of In is soldered on top of both Au electrodes, along their entire length, before clamping the capillary on place. As a final check, the electrical resistance between the holder top electrode and the end of the In-painted Au electrode is measured. Typically this resistance is about 0.2 - 0.4 Ω (to be compared to about 2 Ω for the case without In layer). This considerably lowers R_{p} down to very consistent value of 0.5 - 1 Ω.

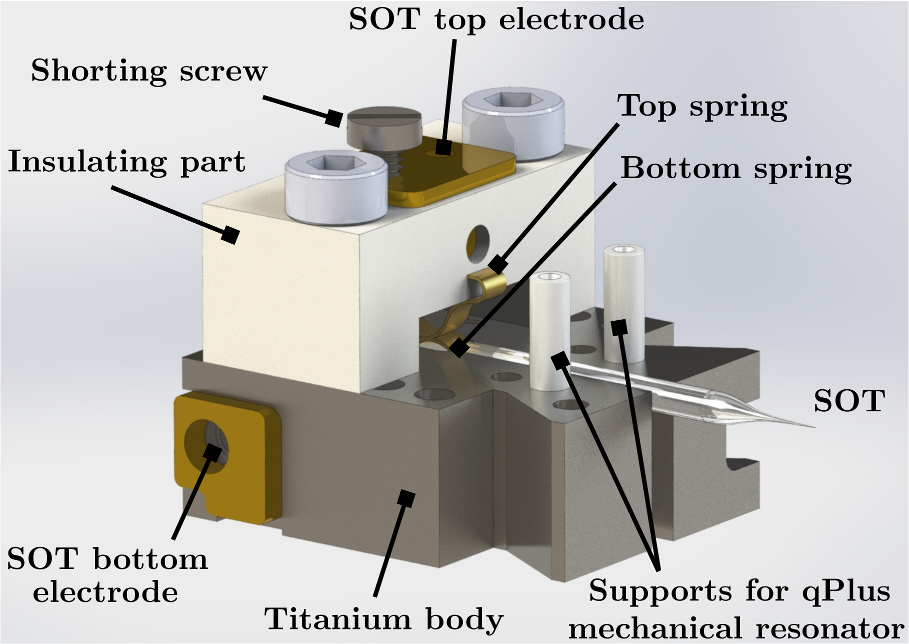

FIGURE 2.4: 3D rendering of the SOT holder. The main body is made of titanium, which is a non-magnetic material. The pulled capillary, with the evaporated Au electrodes and short, is clamped by two conductive springs. The bottom spring is electrically connected to the holder body and to the lower Au SOT electrode; the top spring is insulated from the holder body and provides electrical contact just to the top SOT Au electrode. A screw allows to electrically short bottom and top electrodes, as a safety while not measuring. Two supports are suited for the integration of a qPlus mechanical resonator, coupled to the tip apex.

2.2 SQUID-on-Tip fabrication

In the following, for the three materials of interest the deposition procedure and few SEM pictures of final devices are shown.

2.2.1 Pb deposition

Our interest in Pb is motivated by its potential in terms of extremely low current noise and high magnetic sensitivity. At 4.2 K it was reported to show a record flux noise of $50\ \mathrm{n}\Phi_0/\sqrt{\mathrm{Hz}}$ [54].
Pb deposition was performed via thermal evaporation in a high-vacuum custom-built evaporator. This technique is rather simple to describe. Pb pellets are placed inside a tungsten boat at the bottom of a low-pressure chamber. A large DC current ($\sim$ 100 A or more) flows through the boat and makes the pellets melting and then evaporating. Due to the vacuum level, Pb atoms travel ballistically (without scattering) upwards in the direction of the target of interest.
Our custom-built evaporator uses a turbomolecular pump to reach a base pressure of 5×10^{-8} mbar. The sample holder is mounted on the end of a rotateable sample stage, called cold-finger. This allows to coat the capillary with Pb, with the capillary rotated at different angles, as shown in Figure 2.5. This feature is of extreme importance, because the SQUID can be fabricated in one unique evaporation cycle, without the need of accessing the evaporator to change the orientation of the capillary.

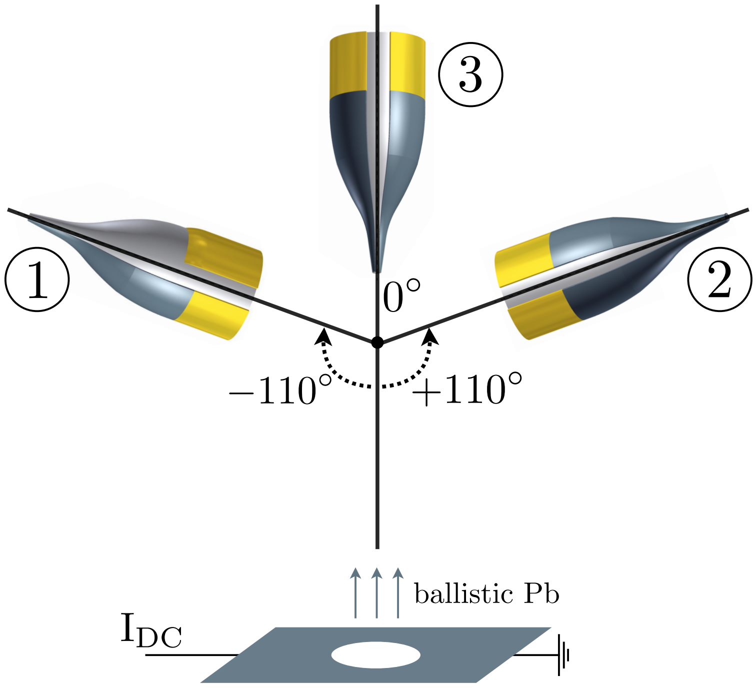

FIGURE 2.5: Thermal evaporation of Pb. Firstly the superconducting electrodes ① and ② are deposited, with the pipette rotated by ± 110°, then the SQUID ring ③ is formed on the tip apex by evaporating Pb on the pipette aligned to 0°.

At room temperature Pb atoms are characterized by a high surface mobility, which results in a growth of islands barely connected to each other. In fact, Pb films

deposited at room temperature show percolation only for large deposited thickness. Moreover, Pb films degrade quite fast when exposed to oxygen, due to a rapid oxidation process. To overcome these issues, it is important to improve the base operating pressure and cool the sample holder as much as possible. In our system this is done in two ways.
In first place, the sample holder is surrounded by a shell (with a hole facing the tungsten boat), cooled down to 77 K. This is helpful to perform cryo-pumping and improve the vacuum down to 1×10^{-8} mbar. Furthermore, the cold-finger has a hollow interspace where liquid ^{4}He can flow. This cools the copper sample holder by thermal contact down to a $T \sim 4.5$ K. This holder is in contact with the titanium SOT holder hosting the quartz pipette. We do not have a temperature sensor on the titanium holder and it is predictable that temperature of quartz will be higher than 5 K, due to the low thermal conductivity of both titanium and quartz. However, we experienced that waiting long time after inserting liquid helium allows to achieve good quality Pb thin films.

In the following, the procedure used to deposit Pb is reported. We refer to Figure 2.5 for the order of the deposition stages and the rotation of the capillary in each stage.

1. After pumping to 5 - 8 $\times 10^{-8}$ mbar, the shell around the SOT holder is cooled by liquid nitrogen. This allows to reach the bottom of 10^{-8} mbar range.
2. Cold-finger is cooled down by tiny flow of liquid ^{4}He.
3. 40 minutes waiting time, while He gas at a pressure of 5×10^{-5} mbar is maintained in the main chamber. This improves the heat exchange between the cold-finger and the titanium SOT holder.
4. 5 minutes pumping, to recover base pressure.
5. Superconducting electrode ① at -110°. This coats the capillary by overlapping one indium-coated Au electrode. Evaporation rate is ~ 2 Å/s and final thickness is $\sim$ 25 - 30 nm.
6. 20 minutes waiting time, while He gas at a pressure of 5×10^{-5} mbar is maintained. This helps in cooling the pipette down after hot Pb film was deposited.
7. 5 minutes pumping.
8. Superconducting electrode ② at +110°, overlapping the other indium-coated Au electrode. Typically, same amount of material of the other electrode is deposited, at a similar rate.
9. 30 minutes waiting time, followed by 5 minutes pumping.
10. Apex ring ③ at 0°. Thickness is $\sim$ 20 - 25 nm.

Figure 2.6 presents SEM images of four working Pb SOTs, with effective diameters in the range 105 - 300 nm. Figure 2.6(a) highlights the key elements of the sensor. The blue dotted line defines the gap between the two superconducting electrodes. The homogeneous thin coating means that the quartz capillary was well cooled during the deposition process. The two red dotted lines mark the Dayem bridges closing the apex ring.
SOTs in Figure 2.6(a)-(b) are made using standard 1mm OD quartz capillaries, while the ones reported in Figure 2.6(c)-(d) are made starting from 4-grooves capillaries. It is interest to notice that the presence of the groove helps in maintaining a well

defined superconducting gap when the diameter of the SOT is reduced to 100 nm. This prevents from creating an electrical short or undesired weak links between the superconducting electrodes.

Here pictures of working SOTs were reported, but overall this fabrication process is not straightforward, it has a low yield and can lead to different failures due to external factors. Main issues are related to electrical discharge, thermal failure in cooling the capillary down and non-optimal pulling process. For further pictures showing typical issues in Pb deposition we refer to Appendix B.

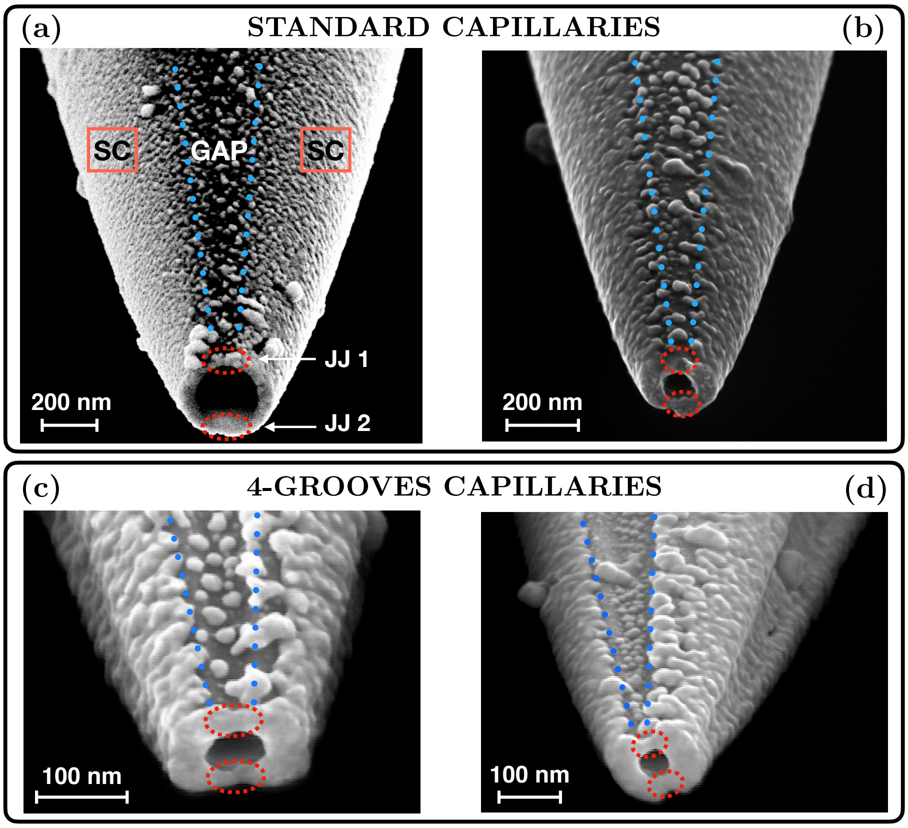

FIGURE 2.6: SEM images of Pb SOTs, where (a)-(b) are standard capillaries and (c)-(d) are 4-grooves capillaries. (a) Diameter ∅300 nm. The blue dotted line defines the superconducting gap between the two electrodes (labelled as SC) on the sides. The red dotted circles at the apex mark the two Dayem bridges closing the SQUID ring. (b) ∅155 nm. (c) ∅125 nm. (d) ∅105 nm. In (c)-(d) it is possible to notice the positive influence of the groove in maintaining a well defined superconducting gap when the diameter of the SOT is reduced to 100 nm.

2.2.2 MoGe deposition

The fabrication of Molybdenum-Germanium (MoGe) SOTs is motivated by the interest in developing a robust sensor that shows low degrade in air, can operate at sub-Kelvin temperature and in presence of high applied magnetic field. In this temperature range Pb SOTs become highly hysteretic due to an increase of the critical current and thermal instabilities. Moreover, even the smallest Pb SOT is limited to an applied field of about 2 T. Compared to Pb, MoGe better performs in the mK temperature regime and has a high critical magnetic field of about 3 - 4 T at base temperature.

Deposition techniques arising from point-like sources in high vacuum, such as e-beam evaporation or thermal evaporation described for the Pb case, are the most straightforward way to achieve a self-aligned coating method and avoid electrical shorts between the superconducting leads. However, these techniques are not suitable to evaporate alloys and the choice of materials is limited to elemental materials, such as Pb, Nb, In, Al.

An alternative technique, well established for the deposition of high quality, thin films on planar subtrates is magnetron sputtering deposition. This relies on the production of a plasma through electrical discharge and on electrostatically accelerated ions hitting a target of the material of interest. The target is positioned as a cathode inside a electrically grounded chamber which is in ultra-high vacuum (UHV) condition. Collisions of ions with atoms at the surface of the target can lead to an ejection of atoms into the vacuum environment. In order to increase the yield of the process, magnetron sources are used to confine the charged particles of the plasma close to the surface of the target: the combined effect of the electric field driving the sputtering process and the magnetic field due to the magnets placed behind the target leads to a higher electrons concentration in the target region, which results in a higher ionization rate and in a higher deposition rate.

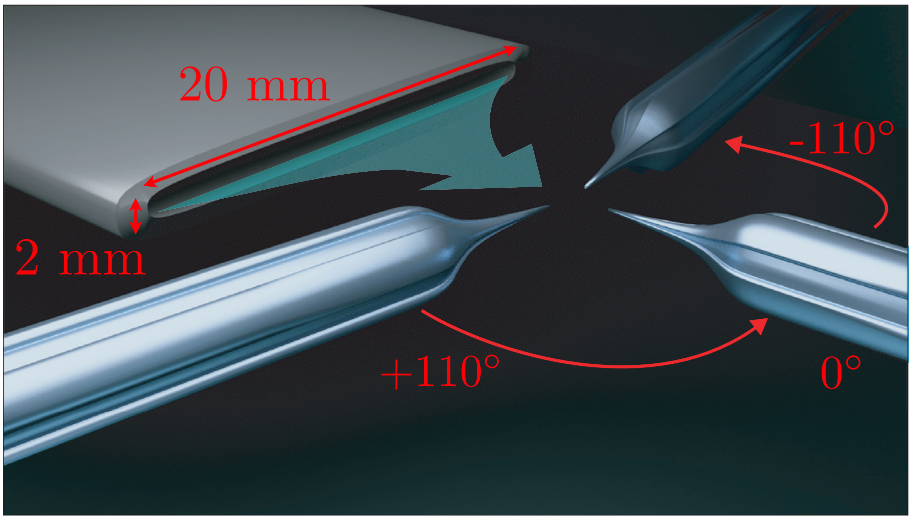

FIGURE 2.7: Sketch of magnetron sputtering setup, with collimation slit filtering the flow of atoms ejected from the target. Due to the difference in pressure before and after the slit, the flow of atoms directed towards the capillary is quasi-ballistic. The pipette, whose shape is reported in Figure 2.1(b), can be rotated in-situ to achieve three stage deposition in one unique process.

Typically targets with large size (1 or 2 inches diameter) and high Ar gas pressure ($\sim 2 - 5 \times 10^{-3}$ mbar) are required for depositing high quality thin films. This leads to a diffusive propagation of metallic atoms, which in principle is not compatible with SOT fabrication.

A way to combine magnetron sputtering and ballistic-flow deposition from point-like source relies on a differential pressure between the two regions where target and sample are located [9]. A closed chamber is implemented and mounted on a commercial sputtering source (AJA 320-XP UHV) in a way that surrounds the target and completely separates it from the main chamber where the quartz capillary is located. The sputtering chamber is set up with a dedicated gas line which allows to spark a plasma and the only connection between the sputtering chamber and the main chamber is a provided by a small cross-sectional area slit, that acts as a collimator for the sputtered atoms.

The collimation slit provokes a difference in pressure of two orders of magnitude or more between the sputtering chamber ($\sim 10^{-3}$ mbar) and the main chamber ($\sim 10^{-5}$ mbar). This allows proper operation of the sputtering source, as well as a quasi-ballistic flow of atoms out of the slit. Obviously, the plasma flow is subjected to get widened when the distance from the slit increases, making the flow more diffusive than ballistic; for this reason, the capillary is kept as close as possible to the outer part of the collimator.

Our situation is sketched in Figure 2.7. The main chamber can be pumped down to a base pressure of 7×10^{-10} mbar, thanks to the combination of baking up to 400 K, use of turbomolecular pump and cryocooling with liquid nitrogen cold-finger. The typical pressure obtained after one day attests on about 2 - 4 $\times 10^{-9}$ mbar. We use a 79/21 weight percent, 99.95% pure, 0.250 inch thick and 2 inches diameter MoGe target. The collimation slit has dimensions of 20 mm × 2 mm and the capillary is about 20 mm far from the outer part of the slit. A Ar gas pressure of 5×10^{-3} mbar is set in the sputtering chamber, corresponding to 1.5×10^{-5} mbar in the main chamber where the capillary is placed. A DC power of 120 W is used to achieve a sputtering rate of about 0.8 Å/s outside the collimation slit. The film thickness on both electrodes and apex ring is in the range from 40 to 60 nm.

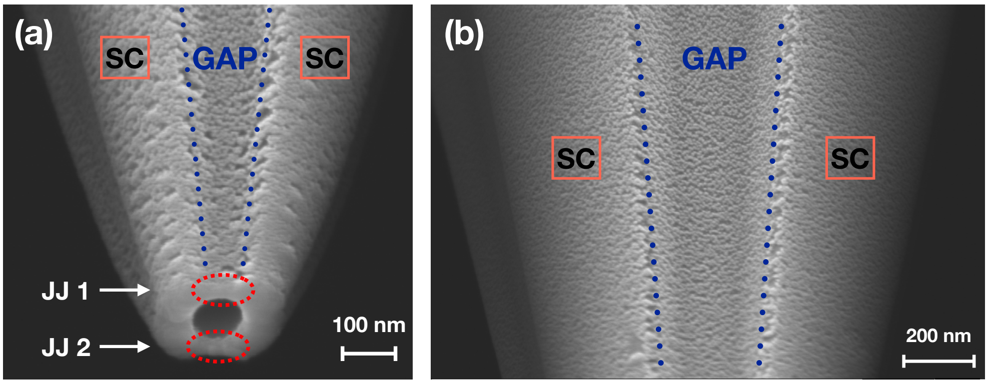

FIGURE 2.8: SEM images of a 4-grooves, ∅150 nm sputtered MoGe SOT. (a) view of the apex, where the blue dotted line defines the superconducting gap between the two electrodes (labelled as SC) and the red dotted circles at the apex mark the two Dayem bridges closing the SQUID ring. (b) zoomed-in view of the superconducting gap at few micrometers of distance from the tip apex. It is possible to notice the considerable amount of material deposited on the gap due to lack of directionality in the sputtering deposition method. However, thanks to the grooves and to the collimaton process, the two electrodes are not electrically shorted.

The technique just described proved to be extremely reliable, tested on a wide range of pressures, deposition angles and amount of material deposited. Figure 2.8(a) reports the SEM image of the apex of a ∅ 150 nm sputtered MoGe SOT, while Figure 2.8(b) shows the superconducting electrodes and the gap at few μm of distance from the apex. The main difference from the evaporated Pb SOTs is the increased amount of material coating the gap between the electrodes due to a lack of directionality in the deposition method. However, the combination of grooves and collimation system help in avoiding undesired electrical shorts.

2.2.3 Nb deposition

Nb SOTs are meant to be a compromise between the sensitivity of evaporated Pb SOTs and the robustness and wide temperature and field working range of the sputtered MoGe SOTs.

There are few concerns regarding Nb deposition. Firstly, when Nb is exposed to oxygen, a dead layer of material is created, which degrades the superconducting properties of the film. A similar degradation involves the first few atomic layers that are in contact with the quartz capillary. As a consequence, thicker films are required to ensure that the film remains superconducting.

The first idea to overcome these issues is to use the magnetron sputtering deposition technique explained for MoGe, relying on a differential pressure and a collimation slit to guarantee a superconducting gap between the electrodes. Particularly crucial for Nb deposition is the base pressure in main chamber before inserting Ar gas, to reduce contamination from oxygen. As mentioned before, the base pressure achievable in one day is about 1×10^{-9} mbar.

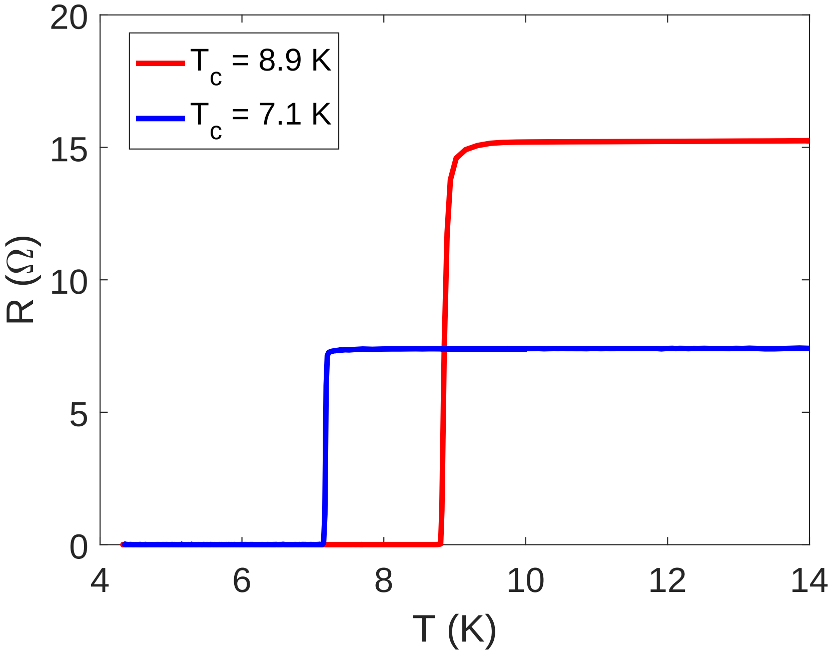

FIGURE 2.9: Measurement of the electrical resistance as function of temperature for two different 50 nm thick Nb planar devices, sputtered on Si/SiO$_2$. In both cases a 4-point-measurement is performed, showing a sharp transition from superconducting to normal state. The discrepance in the normal state resistance to which the samples transition can be explained by a different sample shape. The blue curve, with a T_c = 7.1 K, refers to a Nb film sputtered with collimation chamber; the red curve, with a T_c = 8.9 K, refers to a Nb film sputtered without collimation chamber and encapsulated in between two thin sputtered layers of Ti. Encapsulation increases the quality of the thin film.

In order to estimate the quality of a sputtered Nb thin film, a standard planar device suitable for 4-point-measurement was fabricated on Si/SiO$_2$ substrate via optical lithography. After reaching a base pressure of 8×10^{-10} mbar, a 50 nm Nb film was sputtered using a DC power of 150 W and Ar pressure of 3×10^{-3} mbar, corresponding to a sputtering rate of 0.5 Å/s outside the slit. The 4-point-measurement of the electrical resistance as function of temperature is shown by the blue curve in Figure 2.9. The device undergoes a sharp transition from normal to superconducting state at $T_c = 7.1$ K. This temperature is quite far from the critical temperature, $T_c = 9.3$ K, found in case of bulk Nb. The discrepance of more than 2 K can be explained by the contamination of both bottom and top layers due to quartz and oxygen, as well as by the not ideal deposition method offered by the collimation slit. In fact, the slit increases the DC power required for obtaining a sufficient sputtering rate, in such a way the atoms undergo many scattering processes before being ejected from the slit. This chaotic ejection of atoms contributes to lower the quality of the sputtered film. It is predictable that sputtering on a curved surface such as a quartz capillary will further contribute in decreasing the quality of the thin film, and consequently the T_c value.

A second approach is to recover a conventional sputtering process by removing the collimation chamber and to encapsulate the Nb film between a bottom and top thin Ti layers. A similar planar device was fabricated and a 50 nm thick Nb film was sputtered using a DC power of 70 W and Ar pressure of 5×10^{-3} mbar, corresponding to a sputtering rate of 3 Å/s. The higher rate, meaning a faster process, together with less chaotic ejection of atoms and lack of contamination from oxygen, are expected to provide a much higher T_c value. Measurement of the electrical resistance as function of temperature for this device is shown by the red curve in Figure 2.9. The critical temperature is $T_c = 8.9$ K, which is very close to the T_c of bulk Nb. The discrepance in the normal state resistance to which the two samples transition can be explained by a different sample design.

As a further proof of the better quality provided by the second method, the RRR ratio between the electrical resistance R at 300 K and the residual R before the transition to superconducting state was evaluated for both samples. A higher ratio means a better film quality. Sputtering with collimation slit and without encapsulation of the Nb film provides a RRR ratio of about 1.6 ($R_{300K} \simeq 12\ \Omega$, $R_{10K} \simeq 7.3\ \Omega$), while conventional sputtering with encapsulation of the Nb film leads to a RRR ratio of about 3 ($R_{300K} \simeq 45\ \Omega$, $R_{10K} \simeq 15\ \Omega$).

After testing the quality of the two methods, Nb sputtering deposition on quartz capillaries was performed without collimation slit and sandwiching the Nb film with bottom and top Ti layers. Nb is sputtered with a DC power of 70 W, Ar pressure of 5×10^{-3} mbar at a flow of 30 sccm. The sputtering rate is 3 Å/s. Ti is sputtered with a DC power of 60 W, Ar pressure of 5×10^{-3} mbar at a flow of 30 sccm. The sputtering rate is 1.25 Å/s. A typical recipe is 3 nm Ti / 28 nm Nb / 3 nm Ti on the electrodes, with an angle of $\pm 120°$, and 5 nm Ti / 30 nm Nb / 4 nm Ti on the apex ring.

The increased deposition angle for the electrodes, together with the presence of grooves, contributes to maintain a gap between the two superconducting electrodes. This can be seen in Figure 2.10, where two sputtered Nb SOTs are shown, with ⌀80 nm in Figure 2.10(a) and ⌀220 nm in Figure 2.10(b).

Despite a well defined superconducting gap, it is not straightforward to obtain working Nb SOTs with this technique and margins of improvement can be gained by tuning the thickness of the bottom and top Ti layers, as well as by tuning Ar pressure and DC power value to modify the Nb grain size. Furthermore, Nb film quality could be improved by upgrading the setup in such a way a lower base pressure is reached.

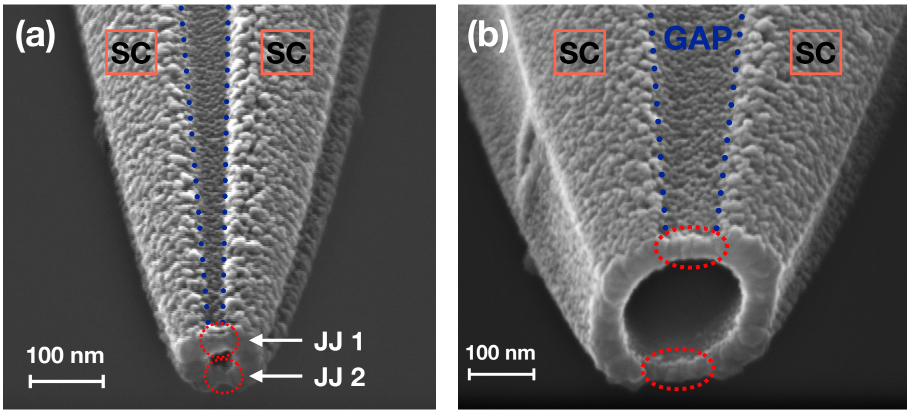

FIGURE 2.10: SEM images of two 4-grooves sputtered encapsulated Nb SOTs. (a) ∅80 nm (b) ∅220 nm. The blue dotted line marks the edges of the superconducting gap between the two electrodes and the red dotted circles at the apex indicate the two Dayem bridges closing the SQUID ring. Thanks to the grooves, a well defined gap can be noticed despite the deposition method is not directional.

2.3 Setup for characterizing the sensors

Before using the SOT sensors as a magnetic scanning tool, their properties need be tested, to understand if they fit the requirements imposed by the planned experiment. Important parameters are the critical current, the sensitivity to magnetic field and flux, the critical field and the scanning spatial resolution, which is connected to the effective diameter of the SOT.
The characterization of SOTs is performed at 4.2 K using a test electrical transport probe, cooled down in liquid helium. The helium dewar contains a superconducting solenoid, which allows to apply a magnetic field along the z-axis up to ±1.2 T. The probe includes a temperature sensor, as well as a local heater, which can be used to heat the SOT holder and characterize the electrical transport properties at different temperature. All the measurements are performed in vacuum.

A schematics of the circuit is highlighted in Figure 2.11. The bias part is consistent with the one reported in Figure 1.7. The circuit elements are:

- V_{bias} is the bias voltage, generated by a programmable DC source, Yokogawa 7651. Typically the voltage ranges from 0 to 3 V.
- R_{bias} is the bias resistance, 6.1 kΩ. This value is given by the series of a "warm", 5.1 kΩ, resistance which stays at room temperature and a "cold", 1 kΩ, resistance which is cooled down to 4.2 K together with the SOT.
- R_{s} is a 3 Ω shunt resistance.
- R_{p} is the parasitic resistance, due the residual resistance of the test probe electrical line and the contact resistance between the Au electrodes evaporated on the capillary and the clamping springs of the tip holder (see Figure 2.4). Thanks to indium coating, R_{p} is usually 1 Ω or less.
- SOT is characterized by a flow of current I_{SOT} and by a resistance R_{SOT}, given by the parallel between the quasiparticle resistance and the Au short evaporated close to the tip apex. Typically $R_{\text{SOT}} \simeq 6$ - 10 Ω.

The current bias $I_{\text{bias}} = V_{\text{bias}}/R_{\text{bias}}$ flows through the parallel between the SOT and the shunt resistance. The amount flowing through the SOT, I_{SOT}, depends on the SOT state, either superconducting or normal. I_{SOT} is the quantity we are interested to measure, because it carries the magnetic flux information sensed by the SQUID. The readout, illustrated on the right side of Figure 2.11, can be described as follows:

- I_{SOT} is inductively coupled to a SQUID Series Array Amplifier (SSAA), shown in blue color, through an input inductance L_{in}. The SSAA is produced by Magnicon. For further reading about SSAA we refer to [94].
- Due to the current coupled through the input inductance, the SSAA senses a flux change.
- When working in Flux Locked Loop (FLL) mode, the SSAA compensates for the measured change in flux via a feedback electronics, shown in green color. The feedback electronics receives the information as a change in voltage and sends back to the SSAA a current, inductively coupled through L_{fb}, which compansates the sensed change in flux.
- The feedback current flows across a feedback resistance, R_{fb}, resulting in a feedback voltage drop V_{fb}.
- V_{fb} is the raw signal measured in the SOT characterization, by a Agilent 34401A Multimeter, as function of V_{bias} and at external applied magnetic field. From the measurement of V_{fb} it is straightforward to calculate I_{SOT}, which is the physical quantity shown in the characterization reported in Sec. 2.4.

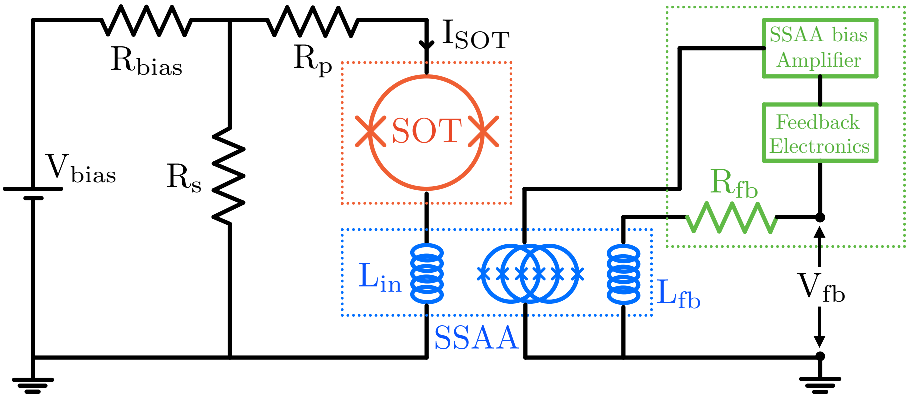

FIGURE 2.11: Sketch of the full SOT circuit. The bias part is consistent with the one shown in Figure 1.7. The readout is performed using a SQUID Series Array Amplifier (SSAA, in blue color), operating in flux-locked loop mode and controlled by a dedicated electronics (green color). The current through the SOT, I_{SOT}, is inductively coupled via L_{in} to the SSAA, which senses a change of flux produced by L_{in}. As a reaction to the change of flux, the feedback electronics flows a current back to the SSAA to compensate the change of flux. This feedback current, flowing through the feedback resistance R_{fb}, results in a feedback voltage V_{fb}, which is the quantity measured in the SOT characterization.

2.4 SQUID performance

The SOTs are tested at 4.2 K in two ways. In first place, by measuring the I_{SOT}-V_{bias} characteristic at different applied magnetic field we are able to show the quantum interference pattern typical of a SQUID sensor.

From the collected data, a 2D plot of individual I_{SOT} vs V_{bias} curves at few magnetic field values can be achieved. This kind of plot shows the behavior of the SOT in its superconducting and normal states. As known from the theory, the superconducting state is characterized by a slope, given by the parasitic resistance. To have a more intuitive understanding of the superconducting state, from the I_{SOT} vs V_{bias} curves it is possible to calculate the I_{SOT} vs V_{SOT} behavior at few magnetic field values of interest.

The second part of the data analysis regards the characterization of the magnetic sensitivity of the device. By taking the first derivative of I_{SOT} with respect to the applied magnetic field, a map of the magnetic response function, $\partial I_{\mathrm{SOT}}/\partial B$, as function of V_{bias} and B can be achieved. By taking a linecut of this map at fixed values of V_{bias}, a 2D plot of few magnetic response functions as function of B at fixed V_{bias} is obtained. This allows to understand in which (V_{bias}, B) points the SOT is responsive and can be used for a magnetic scanning experiment.

The second performed measurement includes the use of a spectrum analyzer. In a restricted magnetic field region of interest, for few values of V_{bias}, I_{SOT} is recorded, together with its spectral current noise. This allows to determine the magnetic field and flux noise at a specific frequency and the magnetic field noise spectral density at individual (V_{bias}, B) points. This is extremely important, because it shows the ultimate limit for the magnetic field or flux which can be detected by the SOT as function of the chosen bandwidth.

In the following section, the full set of data for a Nb, ∅180 nm SOT will be reported and discussed, and some characteristics such as critical current and magnetic response function will be compared to the ones achieved by MoGe and Pb SOTs.

2.4.1 *I*-*V* characteristics

By referring to the electrical circuit shown in Figure 2.11, the first measurement consists on sweeping V_{bias} and recording V_{fb} data, for a set value of applied magnetic field B. The measurement is repeated at different fields of interest. By dividing V_{fb} by R_{fb}, data are converted into I_{SOT} and plotted as function of B and V_{bias}.

The current map I_{SOT} as function of B and V_{bias} for a Nb, ∅180 nm SOT is reported in Figure 2.12, where the colorscale describes the amount of current flowing through the SOT, expressed in units of μA. The map of I_{SOT} shows a clear quantum interference pattern, which proves the SQUID behavior of the SOT. Current modulates between a minimum value and the critical current, with the periodicity of one flux quantum Φ_0. In the range from -0.1 to 0.1 T, almost three periods can be observed. The critical current at zero magnetic field is about 50 μA. By knowing the B range corresponding to one oscillation period, B_{period}, and by reminding that flux quantization imposes $\Phi_0 = B_{\mathrm{period}}\pi r^2$, the effective diameter of the SOT can be calculated as follows:

$$d\ [\mathrm{nm}] = 2\sqrt{\frac{\Phi_0 \cdot 10^{18}}{\pi B_{\mathrm{period}}\ [\mathrm{T}]}} = 2\sqrt{\frac{2065}{\pi B_{\mathrm{period}}\ [\mathrm{T}]}} \tag{2.1}$$

The period of 0.081 T corresponds to an effective diameter of 180 nm.

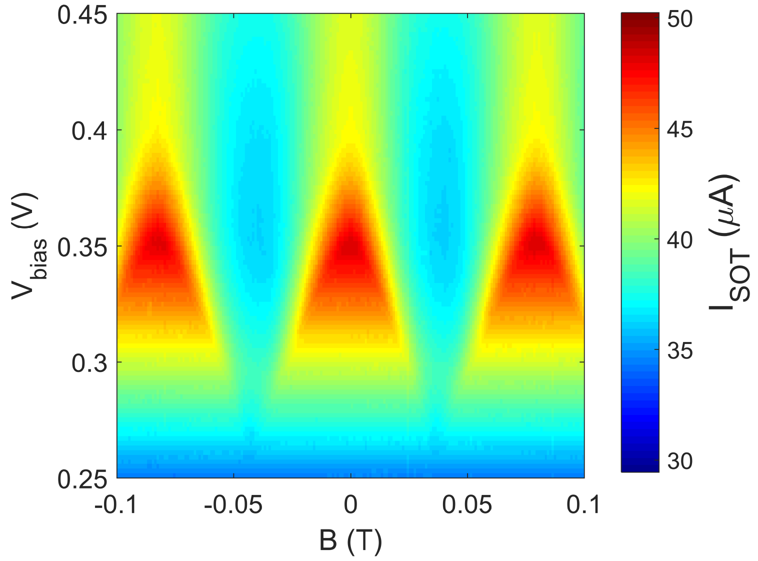

FIGURE 2.12: Map of I_{SOT} as function of V_{bias} and applied B for a sputtered Nb ∅180 nm SOT, showing the quantum interference pattern typical of SQUIDs with the periodicity of one flux quantum. The map reports the first three periods centered in zero field. Knowing the period of the interference pattern, by using Eq. 2.1 it is possible to calculate the effective diameter of the SOT.

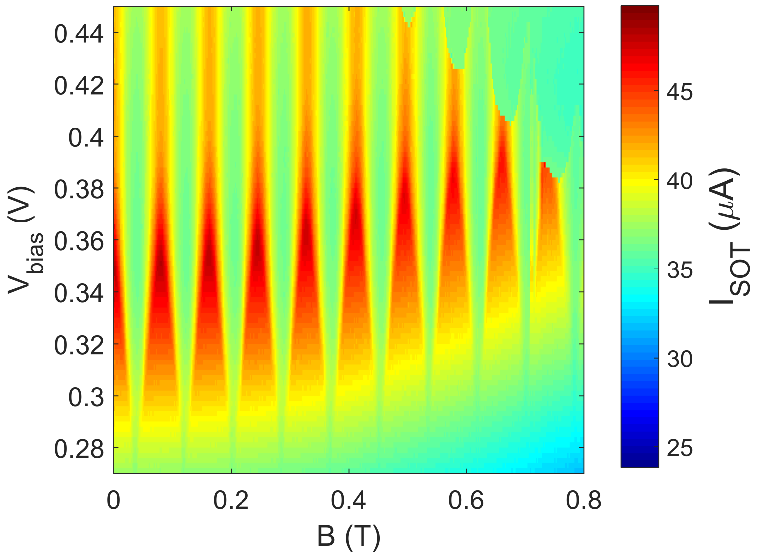

FIGURE 2.13: Map of I_{SOT} as function of V_{bias} and applied B for a sputtered Nb ∅180 nm SOT, showing the quantum interference pattern from zero field up to 0.8 T. This measurement allows to estimate the upper limit for the magnetic field at which the SOT is still responsive at 4.2 K.

The same measurement can be repeated on a wider range of applied B. The purpose is to observe the evolution of the quantum interference pattern at higher magnetic field, until the superconducting properties of the SOT degrade when B

approaches the critical field. This is of great relevance because it defines an upper limit for the applied magnetic field at which the SOT is still responsive. The data measured from 0 up to 0.8 T are reported in Figure 2.13. The interference pattern remains unchanged up to 0.5 - 0.6 T, while at higher fields a constant degradation is observed. The critical field of this SOT at 4.2 K is about 0.9 T.
To provide a better interpretation of the data, we select few B values ranging from a maximum to a minimum of one oscillation period and for each field we plot I_{SOT} as function of V_{bias}. Figure 2.14 shows such a 2D plot for 4-grooves SOTs made of Pb, MoGe and Nb, allowing to compare different materials. To facilitate the comparison, the I_{SOT} range in the plot is chosen to be similar, with the only exception for the MoGe SOT that shows too low values.

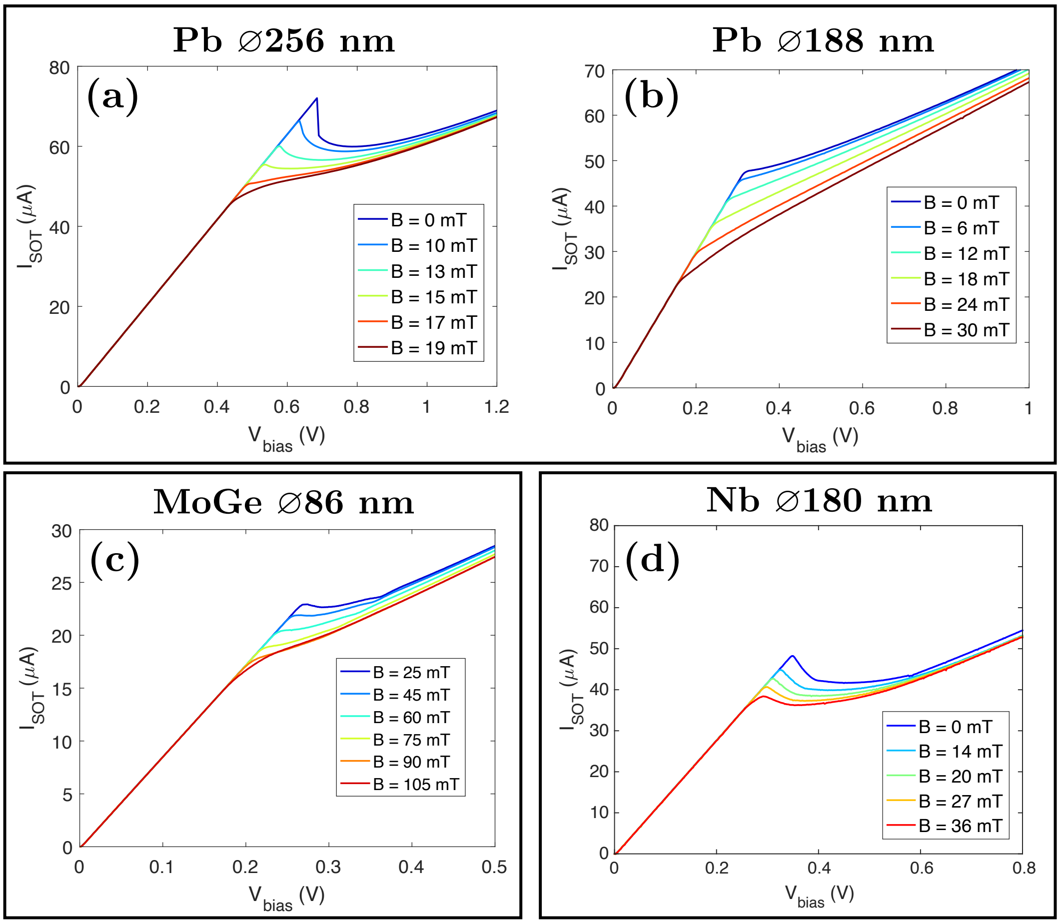

FIGURE 2.14: I_{SOT} plotted as function of V_{bias} for few applied values of B, corresponding to half of B_{period}. The 2D plot shows the SOT in its superconducting state and the transition to the normal state. The linear behavior in the superconducting state is due to the parasitic resistance. I_{SOT} range is similar for all plots, except for (c), where critical current is lower. (a)-(b) Comparison between a $I_c = 72\ \mu$A, ∅256 nm Pb SOT (a) and a $I_c = 48\ \mu$A, ∅188 nm Pb SOT (b). The higher critical current leads to a sharper transition from superconducting to normal state. (c) $I_c = 22\ \mu$A, ∅86 nm MoGe SOT. (d) $I_c = 48\ \mu$A, ∅180 nm Nb SOT.

Figure 2.14(a) reports a $I_c = 72\ \mu$A, ∅256 nm Pb SOT, while Figure 2.14(b) shows a $I_c = 48\ \mu$A, ∅188 nm Pb SOT. The linear behavior in the superconducting state is

due to the parasitic resistance, that slightly changes from sensor to sensor. In agreement with Eq. 1.34, the higher critical current in Figure 2.14(a) leads to a sharper transition from superconducting to normal state, with a negative resistance pattern. This pattern is not observed anymore when lowering I_c by about 25 μA. The values of critical current at which the transition gets from sharp to smooth are a property of the superconducting material. In fact, as can be seen in Figure 2.14(d), a $I_c = 48$ μA, ∅180 nm Nb SOT (I_c value very similar to the one in Figure 2.14(b)) transitions to the normal state by showing a really pronounced negative resistance pattern. Typically even lower is the critical current characterizing MoGe SOTs: Figure 2.14(c) presents a $I_c = 22$ μA, ∅86 nm MoGe SOT. In order to see negative resistance patterns for MoGe, I_c values around 30 - 40 μA are usually required. As we will see in Sec. 2.4.2, this translates to a different magnetic response function for these materials.
Another interesting comparison can be made regarding the modulation of the critical current with the applied magnetic flux. As discussed in Sec. 1.3.2, when β_L, $\beta_c \ll 1$ the critical current of a SQUID modulates between 0 and $I_{c,max}$, where $I_{c,max}$ is given by two times the average critical current of the two junctions forming the SQUID ring. The modulation depth $\Delta I_c/I_{c,max}$ reduces when the screening parameter due to kinetic inductance is no longer negligible. By looking at Figure 1.5(b), we see that $\beta_L \simeq 1$ corresponds to $\Delta I_c/I_{c,max} \simeq 0.5$, while for higher values of β_L the modulation depth decreases linearly with the screening parameter. The data showed in Figure 1.5(b) can be numerically fitted to achieve an expression for β_L as function of $\Delta I_c/I_{c,max}$. This fit assumes that the two SQUID junctions are perfectly symmetric and the reduction of modulation depth is only due to the high kinetic inductance.
From the curves shown in Figure 2.14 we calculate the modulation depth and then estimate the screening parameter. The values $\beta_L \simeq 2.8$ for MoGe (Figure 2.14(c)), $\beta_L \simeq 3.4$ for Nb (Figure 2.14(d)), $\beta_L \simeq 1.6$ for Pb (Figure 2.14(a)) and $\beta_L \simeq 0.85$ for Pb (Figure 2.14(b)) are found. Reminding that $\beta_L = 2LI_{c,max}/2\Phi_0$, the inductance values $L = 500$ pH for MoGe (Figure 2.14(c)), $L = 290$ pH for Nb (Figure 2.14(d)), $L = 91$ pH for Pb (Figure 2.14(a)) and $L = 72$ pH for Pb (Figure 2.14(b)) are achieved. This inductance is mainly due to the kinetic contribution. In fact, the geometric inductance is given by $L_g = \mu_0 d \ \log(4d/r)/2$ [89], where μ_0 is the vacuum permeability, d is the SOT diameter and r is the loop wire radius. For a SOT with diameter of hundreds of nm and loop wire radius of 10 - 30 nm, values of L_g of 1 pH or smaller are estimated.
From the reported data, we can conclude that Pb is characterized by a lower kinetic inductance than MoGe and Nb; this mainly reflects on a wider range of working points with high magnetic response function, and so on a better usability as the sensor for magnetic imaging.

As a last consideration, it is sometimes convenient to relate the current flowing through the SOT to the voltage drop across the SOT. Starting from the I_{SOT}-V_{bias} characteristic, by reminding Eq. 1.34, an expression for V_{SOT} can be calculated as follows:

$$V_{SOT} = V_{bias}\frac{R_s}{R_{bias}} - I_{SOT}(R_s + R_p) \tag{2.2}$$

Using this equation for the case of the ∅180 nm Nb, Figure 2.14(d) transforms into Figure 2.15, where V_{SOT} is plotted as function of I_{SOT} for four applied values of B, corresponding to half of B_{period}. The superconducting state is described by a flow of current with no voltage drop across the SOT. After the transition to the normal state, V_{SOT} discontinuously jumps to the value given by Eq. 2.2.

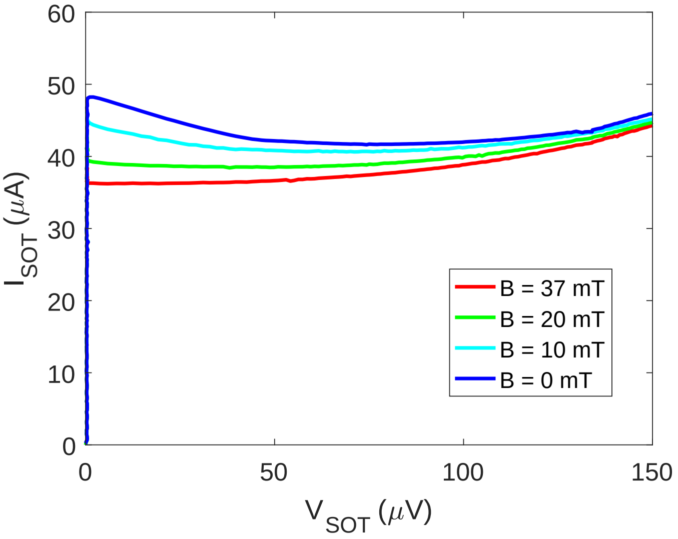

FIGURE 2.15: I_{SOT} as function of V_{SOT} for a ∅180 nm Nb SOT, plotted for four applied values of B, corresponding to half of B_{period}. It represents the same I-V characteristic of Figure 2.14(d), with V_{SOT} calculated by removing the contribution from V_{bias} due to R_p by using Eq. 2.2. The superconducting state shows the flow of current through the SOT with no voltage drop across the device, until the normal state is reached.

2.4.2 Magnetic response function

After mapping the current I_{SOT} flowing through the SOT as function of V_{bias} and B and analyzing how the critical current scales with the magnetic field, it is required to find the working points (V_{bias}, B) that maximize the magnetic sensitivity of the SOT. This quantity, called magnetic response function, is defined as $\partial I_{SOT}/\partial B$ and is given by the derivative of the current with respect to the field. It quantifies the shift in current when a tiny change in field is introduced. When using the SOT as a magnetic scanning sensor, the response function is very important because it defines the shift in I_{SOT} based on the stray magnetic field coming from the investigated sample.

Figure 2.16 shows the magnetic response function for the two Pb tips, whose I-V characteristics were presented in Figure 2.14(a,b). Figure 2.16(a,c) are related to the ∅188 nm SOT, while Figure 2.16(b,d) to the ∅256 nm SOT. The top part shows the magnetic response functions, mapped as function of V_{bias} and B. The ∅188 nm SOT, according to its smooth-transition I-V characteristic, presents wide (V_{bias}, B) regions with good magnetic response. Contrary, the ∅256 nm SOT has highly sensitive, but at the same time more localized, (V_{bias}, B) regions.
To quantify the magnetic response function, in the areas marked by the black stepped line, linecuts of $|\partial I_{SOT}/\partial B|\,(B)$ at set values of V_{bias} are taken. As observed in the map, the SOT with bigger diameter, higher critical current and sharper transition to normal state offers three times more magnetic response ($\sim$ 1800 μA/T vs 600 μA/T) than the other SOT. This comes to the price that the bigger response is achieved on a narrower B range ($\sim$ 5 mT vs 10 mT).

One more point regards the choice of the V_{bias} region where to analyze the magnetic response. In both cases a V_{bias} value at which the SOT did not fully transition to the normal state was set. This leads to a higher $\partial I_{SOT}/\partial B$ compared to the one found for V_{bias} values at which the SOT fully transitioned to the normal state. On the other hand, the higher magnetic response leads to blind spots where the SOT is

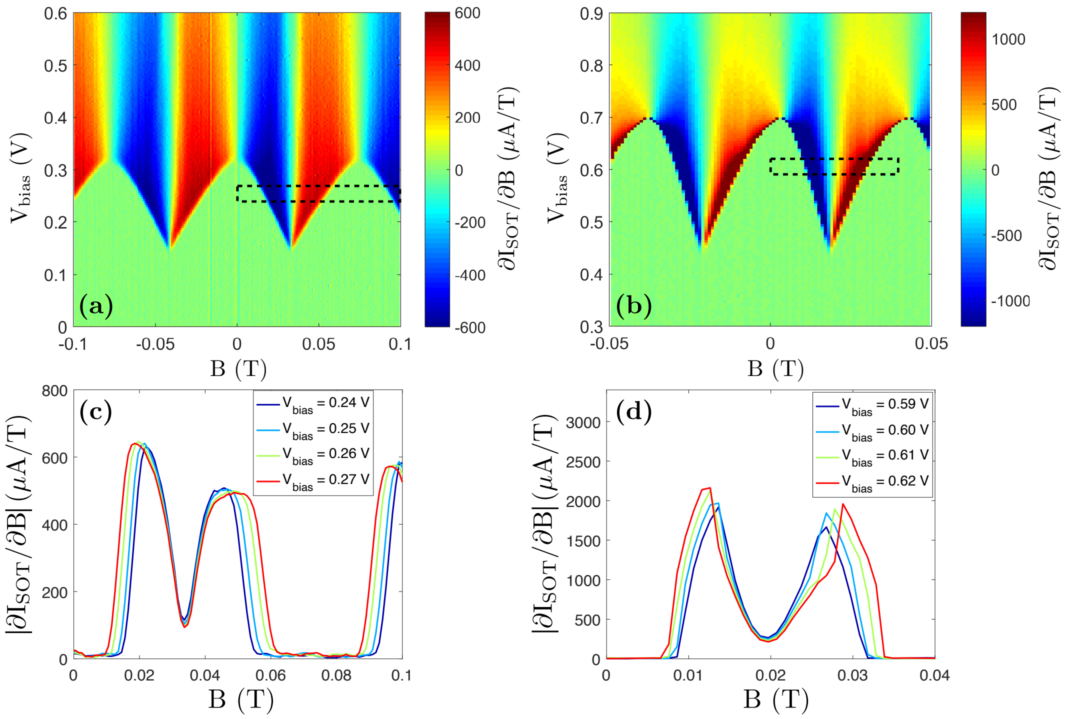

FIGURE 2.16: Magnetic response function and data analysis for two Pb SOTs with diameters ∅188 nm (a,c) and ∅256 nm (b,d), whose I-V characteristics was presented in Figure 2.14. (a,b) Magnetic response function $\partial I_{\mathrm{SOT}}/\partial B$ plotted as function of V_{bias} and B. The stepped line marks the region where linecuts of $|\partial I_{\mathrm{SOT}}/\partial B|\,(B)$ are plotted for fixed values of V_{bias} (c,d). Due to the bigger diameter and higher I_c, the ∅256 nm SOT has a magnetic response three times bigger than the one of the ∅188 nm SOT, but the field range that offers this magnetic response is narrower. Contrary, the ∅188 nm SOT shows less magnetic response, but on a wider field range.

superconducting and the response is almost zero. This can be detrimental for certain magnetic scanning experiments, where magnetic sensitivity at specific B is required. For this reason, the working V_{bias} point can be tuned accordingly to the imposed requirements.

The same study can be repeated for the ∅86 nm MoGe SOT, reported in Figure 2.17 and for the ∅180 nm Nb SOT, shown in Figure 2.18. In both cases the magnetic response function is analyzed at low and high magnetic field.

The MoGe SOT shows a $\partial I_{\mathrm{SOT}}/\partial B$ considerably lower than the one offered by Pb. The difference of more than one order of magnitude is partially justified by the smaller diameter (86 nm vs 188 nm and 256 nm), but an important role is played by the material. MoGe is characterized by low currents flowing through the SOT, and this implies a worse magnetic response. On the other hand, the small diameter leads to a low drop of performance with field. In fact, at 1 T, still the 60 - 80% of the magnetic response is found. Unfortunately, it was not possible to characterize the critical field of the sensor at 4.2 K, because of the upper limit of 1.2 T imposed by the magnet power supply.

The ∅180 nm Nb SOT offers a good compromise between the Pb and MoGe properties. In fact, the magnetic response function is comparable to the one of the Pb SOT with similar diameter with smooth-transition and low critical current, and absolute values of $\partial I_{\mathrm{SOT}}/\partial B$ at zero field are as good as 600 μA/T. Similarly to MoGe, the magnetic response is maintained up to high applied magnetic field. A drop appears

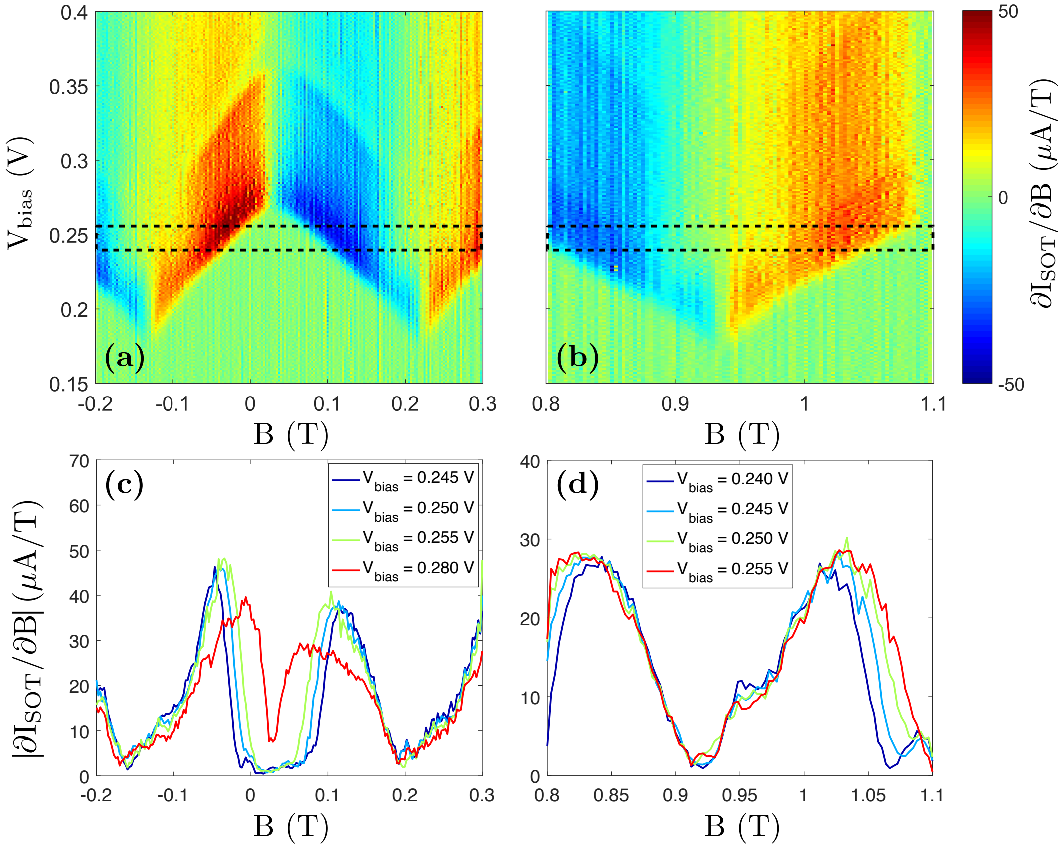

FIGURE 2.17: Magnetic response function and data analysis for a MoGe, ∅86 nm SOT, whose I-V characteristic was presented in Figure 2.14(c). (a,b) Magnetic response function $\partial I_{\rm SOT}/\partial B$ plotted as a function of $V_{\rm bias}$ and B, at low field (a) and at 1 T (b). The stepped line marks the region where linecuts of $|\partial I_{\rm SOT}/\partial B|\,(B)$ are plotted for fixed values of $V_{\rm bias}$ (c,d). The response drops from 40 - 50 μA/T at zero field to 25 - 30 μA/T at 1 T. The small drop in performances with field is due to both small diameter and properties of MoGe.

only above 0.7 T, and the critical field is measured around 0.9 T. Taking into account the relatively big diameter, this result can be considered quite successful.

2.4.3 Noise measurement

The measurement of $I_{\rm SOT}$ as function of $V_{\rm bias}$ and applied B spreads light on many superconducting properties, such as modulation of the critical current and magnetic response function. This characterization allows to understand if a SOT is sensitive enough to be used for magnetic scanning, however it does not reveal which is the ultimate magnetic field or flux that can be detected by the SQUID sensor. In order to get this knowledge, the measurement of $I_{\rm SOT}$ needs to be linked to the measurement of the current noise $S_{\rm I}^{1/2}$.

The electronic circuit remains the one illustrated in Figure 2.11. The raw $V_{\rm fb}$ signal measured by the Agilent Multimeter is splitted and sent to a Stanford SR770, which is a single channel Spectrum Analyzer with a DC to 100 kHz bandwidth. The spectrum analyzer outputs the voltage noise associated to $V_{\rm fb}$ at a certain frequency of

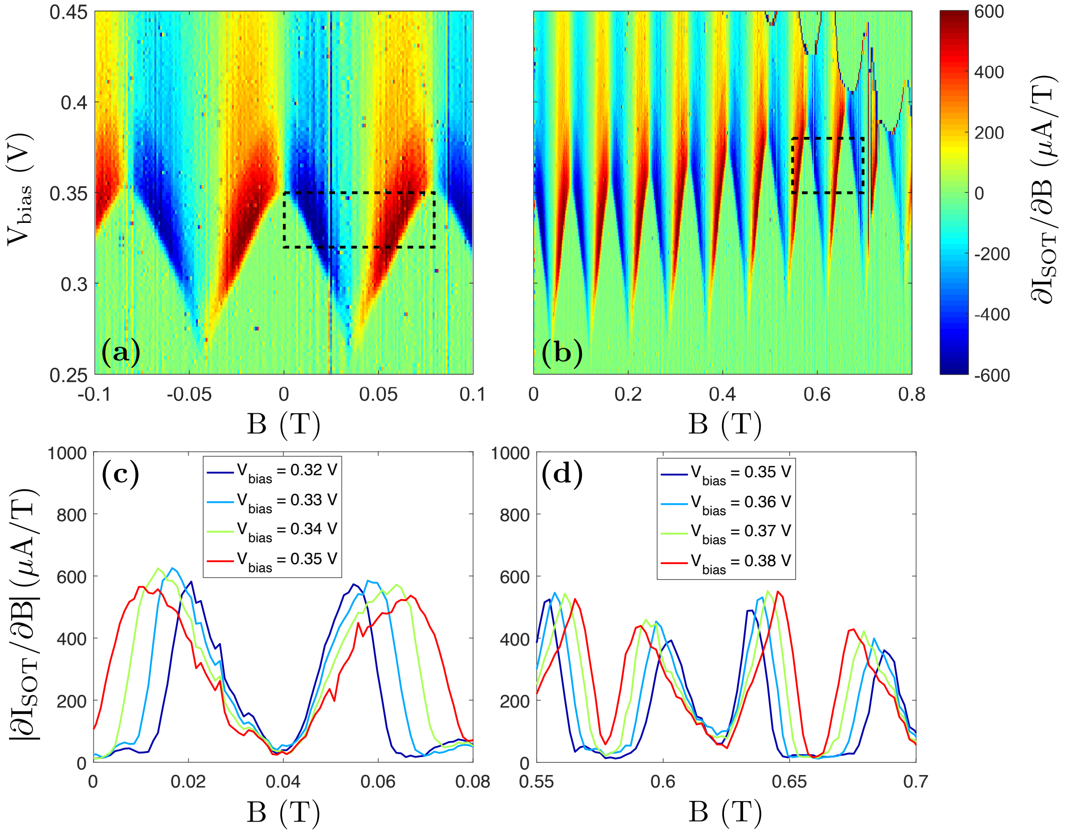

FIGURE 2.18: Magnetic response function and data analysis for a Nb, ∅180 nm SOT, whose I-V characteristic was presented in Figure 2.14(d). (a,b) Magnetic response function $\partial I_{\text{SOT}}/\partial B$ plotted as function of V_{bias} and B, at low field (a) and on a wide field range from 0 to 0.8 T (b). The stepped line marks the region where linecuts of $|\partial I_{\text{SOT}}/\partial B|\,(B)$ are plotted for fixed values of V_{bias} (c,d). The response drops from 600 μA/T at zero field to about 400 μA/T at 0.7 T. Above this field, a drop of the response is found. Considering the not so small diameter of this SOT, the field working range at 4.2 K is quite broad.

interest, expressed in $\mu\text{V}/\sqrt{\text{Hz}}$. Analogously to what explained in the previous section, we convert V_{fb} and its spectral noise into I_{SOT} and current noise.

Figure 2.19 reports the full noise characterization at 4.2 K for a ∅180 nm sputtered Nb SOT. In the measurement few V_{bias} points from 0.32 to 0.35 V are selected and B is swopt from 0 to 80 mT while I_{SOT} and its current noise at a frequency of 12 kHz are acquired. The frequency value is chosen in such a way white noise dominates, while $1/f$ noise is negligible.

Figure 2.19(a) shows the measured current noise $S_{\text{I}}^{1/2}$ in units of $\text{pA}/\sqrt{\text{Hz}}$, for two set V_{bias} points, plotted as function of applied B. The noise attests on values ranging from 100 to 150 $\text{pA}/\sqrt{\text{Hz}}$. Figure 2.19(b) presents the calculated magnetic response function $\partial I_{\text{SOT}}/\partial B$, whose values are consistent with the ones measured and shown in Figure 2.18. The maximum absolute value is about 600 $\mu\text{A}/\sqrt{\text{Hz}}$.

Figure 2.19(c) illustrates the magnetic field noise and flux noise at 12 kHz, as function of B. The magnetic field noise is given by the ratio of current noise and magnetic response function, $S_{\text{B}}^{1/2} = S_{\text{I}}^{1/2}/(\partial I_{\text{SOT}}/\partial B)$ and is reported in units of $\text{nT}/\sqrt{\text{Hz}}$. The flux noise is achieved by dividing the field noise by the SOT effective loop area,

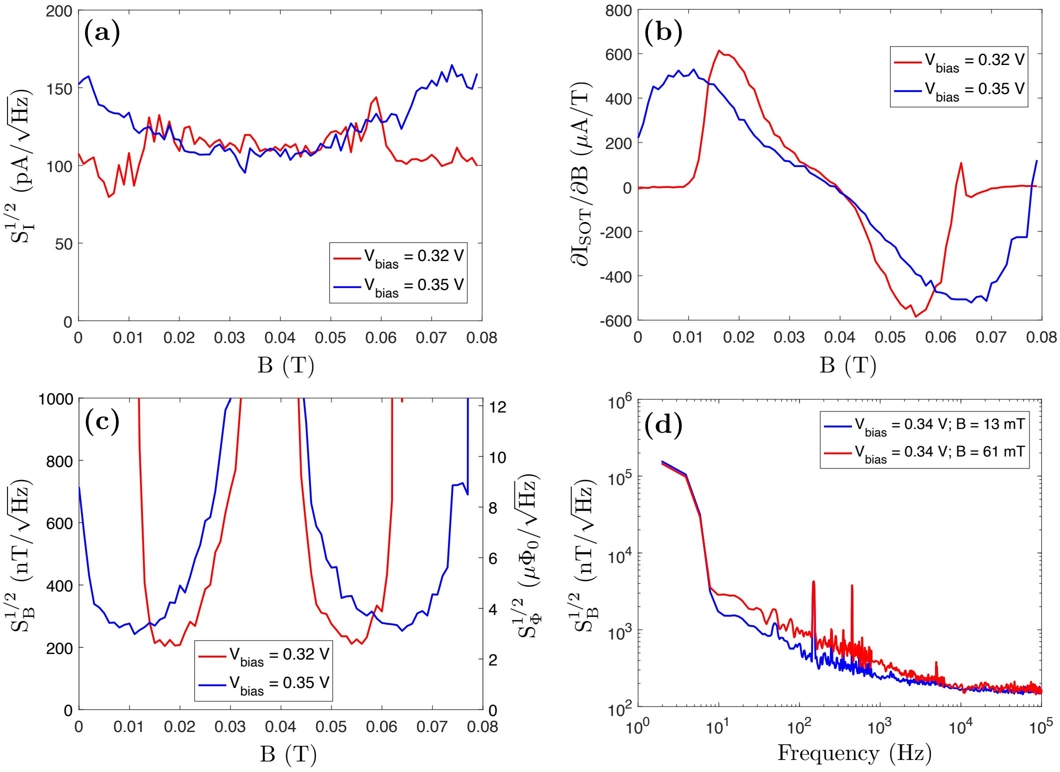

FIGURE 2.19: Noise characterization for a ⌀180 nm Nb SOT at 4.2 K. (a) Measured current noise at a frequency of 12 kHz, plotted as function of applied magnetic field for two values of V_{bias}. (b) Magnetic response function, calculated from the measured $I_{\text{SOT}}(B)$ data. The values are consistent with the ones measured and plotted in Figure 2.18. (c) Magnetic field (left y axis) and flux (right y axis) noise at a frequency of 12 kHz, plotted as function of applied magnetic field. Field noise is given by the ratio of current noise and magnetic response function. Flux noise is derived by the field noise, by scaling it with the effective area of the SOT and is reported in units of the flux quantum Φ_0. (d) Magnetic field noise spectral density, measured at two set (V_{bias}, B) points, reported in logarithmic scale. Magnetic noise is dominated by $1/f$ noise at low frequencies and a white noise $S_B^{1/2}$ of 200 nT/$\sqrt{\text{Hz}}$ is reached at frequencies above 10 kHz.

$S_\Phi^{1/2} = 4S_B^{1/2}/\pi d^2$, and is reported in units of the flux quantum Φ_0. Field noise is depending on the SOT diameter: bigger loop area SQUIDs sense more magnetic field and they will show a lower field noise. Flux noise is scaled accordingly to the loop area, and so it represents a tool to compare the performance of SOTs having different diameters. For this specific Nb SOT, a field noise of 200 nT/$\sqrt{\text{Hz}}$ and a flux noise of 2.5 $\mu\Phi_0/\sqrt{\text{Hz}}$ are measured.

As a further measurement, a (V_{bias}, B) condition is set and the spectral density of $S_I^{1/2}$ is recorded, from 0 to 100 kHz. By dividing the current noise spectral density by the magnetic response at the chosen working point, the magnetic field noise spectral density $S_B^{1/2}$ is found. Figure 2.19(d) shows the magnetic field noise spectral density measured at two working points, ($V_{\text{bias}} = 0.34$ V, $B = 13$ mT) and ($V_{\text{bias}} = 0.34$ V, $B = 61$ mT), reported in logarithmic scale. The noise spikes at low frequencies are located at multiple of 50 Hz. The spectrum is dominated by $1/f$ noise at low frequencies and by white noise $S_B^{1/2}$ under 400 nT/$\sqrt{\text{Hz}}$ above a few hundreds Hz. Above 10 kHz, the magnetic field noise reaches a base value below 200 nT/$\sqrt{\text{Hz}}$, corresponding to

a magnetic flux noise of 2 $\mu\Phi_0/\sqrt{\mathrm{Hz}}$. This magnetic sensitivity is about twice as better than the one from ∅238 nm Nb SOT reported in [54], but still far from the sensitivity offered by Pb SOTs. The same measurement, repeated at 0.5 T, leads to a very mild drop of performance: in fact, $S_B^{1/2} = 250$ nT$/\sqrt{\mathrm{Hz}}$ and $S_\Phi^{1/2} = 3$ $\mu\Phi_0/\sqrt{\mathrm{Hz}}$ are measured.
The field and flux noise measured for this Nb SOT can be compared to the ones achieved by the ∅86 nm MoGe SOT, whose magnetic response function was shown in Figure 2.17. For this SOT, a magnetic field noise $S_B^{1/2} = 2$ μT$/\sqrt{\mathrm{Hz}}$ and flux noise $S_\Phi^{1/2} = 5$ $\mu\Phi_0/\sqrt{\mathrm{Hz}}$ were measured at low field, and a mild drop was observed up to 1 T.

2.5 Analysis on the materials

Through this section, an analysis of which material is chosen for fabricating SOT is provided. This choice is influenced by the requirements imposed by each magnetic scanning experiment. Typical constraints concern scanning resolution, operating temperature and field, and magnetic field or flux noise. In the following, for each of these quantities, a brief comparison between the materials will be discussed, with pros and cons of MoGe, Nb and Pb.

- Magnetic scanning resolution. This is given by the interplay of SOT effective diameter and probe to sample distance. Ideally, when the SOT is scanning at a distance comparable or slightly smaller than the effective diameter, the spatial resolution is set by the SOT diameter.
  From a fabrication point of view, MoGe was found to be very reliable even when the size gets shrinked. Sputtering Nb on tips with apex diameter of 50 nm or smaller is not straightforward and requires a good balance between the thickness of both Nb and Ti bottom and top layers; fabrication yield improves when the diameter becomes 100 nm or bigger. Evaporating Pb is the most challenging SOT fabrication, since the film quality and Pb islands mobility and aggregation depend on the cooling efficiency.
  Another point to consider is the degradation of the material when exposed to air. Pb undergoes a fast oxidation phenomenon, which degrades its superconducting properties until the SOT is no longer working. A smaller diameter SOT is prone to degrade faster. Due to this reason, Pb is a risky choice, as the metarial degrades faster than Nb and MoGe. Nb is subjected to a surface oxidation when exposed to air, but on a slower time scale compared to Pb. MoGe is the most robust material and its properties were proved to be maintained over long time scales and several thermal cycles.
  For these reasons, if a SOT with effective ∅50 - 80 nm is required, the choice of MoGe is made. For effective ∅100 nm or bigger, Nb represents a good choice. When the size gets close to 200 nm, Pb becomes easier to operate.

- Temperature. The upper limit for the temperature working range is set by the T_c of the material. On top of this, depositing material on the curved pipette surface and the contamination of material due to poisoning from quartz and oxygen lead to a decrease of the nominal critical temperature. Thin films of Pb are the ones with the highest T_c, which attests on values close to 7 K. MoGe was tested to provide working SOTs up to just above 5 K, while Nb was preliminary measured up to 6 K. This is considerably lower than the T_c measured for a planar 50 nm thick Nb film. Perhaps it is possible that the T_c value can be

increased with optimizing Ti layers, Nb thickness and sputtering recipe.
For what concerns the lower temperature limit, MoGe can work well down in the mK region and was tested in a ^{3}He refrigerator down to 450 mK. The limit for Nb is still unknown, since there was no chance to cool down a SOT below 4.2 K. As already mentioned, below 4.2 K Pb SOTs become very hysteretic due to the increase of I_c and thermal instabilities. Only by suppressing its superconducting properties, for instance by applying a high magnetic field, Pb can be suitable for magnetic scanning in mK region.

- Magnetic field. The critical field is a property of the material, and is influenced by working temperature and SOT diameter. Smaller diameter SOTs and lower temperatures increase the critical field. Nb SOTs with ∅<100 nm were not fabricated yet, so it is hard to provide a comparison with Pb and MoGe sensors. For the ∅180 nm Nb SOT, a $B_c \sim 0.9$ T at 4.2 K was measured.
  Typical Pb critical field for ∅<100 nm SOT is about 0.5 - 1 T at 4.2 K, which becomes higher than 1 T in the mK region. According to [8], ∅65 nm Pb SOT at 300 mK is reported to have a $B_c > 2$ T.
  Among the materials tested here, MoGe is the one with the highest B_c. The ∅86 nm SOT was tested at 450 mK in a ^{3}He refrigerator up to almost 3 T. At this temperature, a ∅50 nm MoGe SOT could achieve a critical field about 4 T.

- Magnetic noise. A huge performance step in magnetic sensitivity is noticed between MoGe and Pb. In fact, typical measured flux noise for our MoGe SOT is on the order of several $\mu\Phi_0/\sqrt{\text{Hz}}$, while the best Pb SOTs report flux noise of few tens of $\text{n}\Phi_0/\sqrt{\text{Hz}}$ [8, 54]. Nb offers flux noise in between MoGe and Pb, however the barrier of 1 $\mu\Phi_0/\sqrt{\text{Hz}}$ from our Nb SOTs was not overcome yet.
  Based on these numbers, we ideally set a threshold at stray magnetic fields of about few μT. Stray fields above this value can in principle be investigated by any of the superconducting materials described here, MoGe included. For instance, features that produce such high stray magnetic fields are superconducting vortices in type II superconductors [89, 90], magnetic distributions in artificial spin ices [92], magnetic distributions in ferromagnetic nanotubes [91].
  For samples such as twisted bilayer graphene or other 2D materials, or 2D electron gases, signals of fraction of μT or lower are expected. In this case, the magnetic sensitivity of Pb sensors is required.

2.6 Integrating the SOT into a scanning probe setup

Scanning experiments are performed at cryogenic temperature, so the microscope is placed inside a ^{3}He or ^{4}He cryostat. The whole cryostat is incorporated in an optical table and hangs on three supports that can be lifted to isolate the system from low frequency mechanical vibrations. In the lowest part of the cryostat, a superconducting magnet is able to produce a DC magnetic field up to ±6 T along z direction. The scanning probe is enclosed in a stainless steel tube, where UHV is achieved.

The core of the probe is shown in Figure 2.20. The microscope structure hangs on four, non-magnetic springs, which improve the vibration isolation and contribute to reduce the scanning noise floor. Copper plates surround the central titanium frame, while copper braids provide thermal coupling between bottom and top parts of the probe. The titanium frame hosts the two key scanning elements, the SOT top stack and the sample bottom stack. The SOT holder is screwed to the titanium top stage

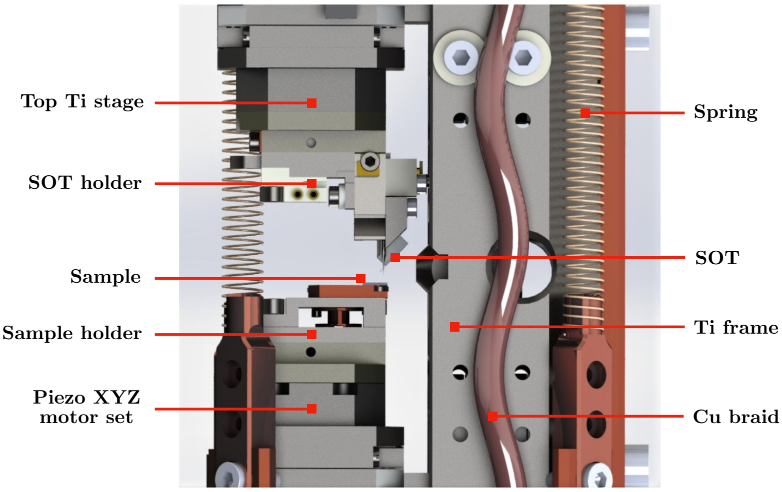

FIGURE 2.20: 3D rendering of the scanning probe. The titanium frame is hanging on four springs, that damp low mechanical frequencies. Copper braids are used to provide cooling power from the top to the bottom of the frame. The top stack where the SOT is mounted is fixed, while the sample is positioned on top of a piezoelectric x-y-z motor set. The set includes positioners and a 2D x-y scanner, with a range of 30 x 30 μm^2 at 4.2 K. When biased by a DC voltage, the z positioner allows for a fine extension with 2 μm range.

and its position is fixed. The bottom stack, containing the sample under investigation, is mounted on top of a piezoelectric motor set. Positioners allow to move the sample in x-y-z directions by several millimeters. When biased by a DC voltage, z positioner provides a fine, very controlled extension, with a 2 μm range. Magnetic scanning is guaranteed by a set of x-y scanners, with a 30 x 30 μm^2 scanning range at 4.2 K.
The SSAA is enclosed in a niobium cylinder, which shields the chip from the influence of external magnetic fields. This is in contact to the copper probe, to ensure thermal coupling to 4.2 K. As a further magnetic isolation, the cylinder is placed about 15 cm above the sample. The vertical separation allows to apply high magnetic fields to the sample and SOT, without interfering with the SSAA operation.

2.6.1 Coupling the SOT to a qPlus mechanical resonator

An upgrade to the SOT scanning probe discussed so far consists of coupling the tip apex to a tuning fork mechanical resonator, analogously to what reported in similar setups [5, 93]. As explained in the following, this coupling allows to have a feedback on the probe to sample distance and to perform SOT magnetic scanning at a constant distance of tens of nanometers.

Figure 2.21 reports a 3D rendering of the full sensor holder. The main titanium body hosting the tip is the same showed in Figure 2.4. On top of this, a titanium slider which can move in the direction orthogonal to the SOT length is added. A commercial shear piezo (Thorlabs PL5FBP3) and a qPlus mechanical resonator are glued on top of the slider. The main difference of the qPlus from conventional tuning forks is that one prong is much wider than the second one and is fixed to the piezo surface. Once the qPlus oscillation is driven, only the narrower prong produces vibrational modes.

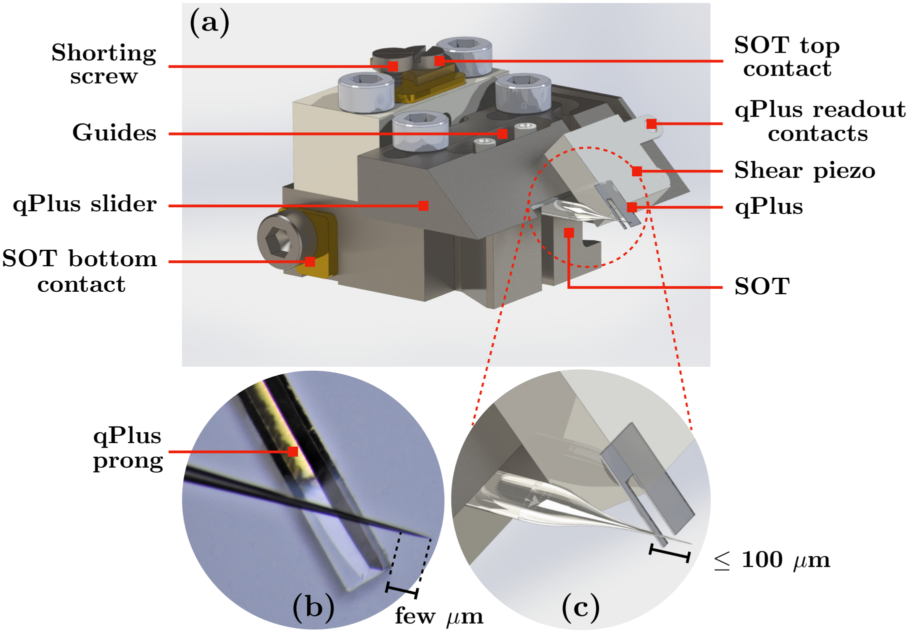

FIGURE 2.21: (a) 3D rendering of the SOT holder including a qPlus mechanical resonator coupled to the SOT apex. The holder is the one described in Figure 2.4. The qPlus is glued on top of a shear piezo, mounted on a titanium slider, which allows to move the qPlus and couple it to the SOT body, close to the apex. (b) optical microscope picture, reporting the very last part of the capillary and the qPlus prong. The protruding part of the prong is about few μm far from the SOT apex. (c) zoomed-in rendering of the coupling of the SOT to the qPlus prong, at a distance of <100 μm from the tip apex.

The qPlus is coupled to the SOT apex using a custom-made manipulator stage. Figure 2.21(c) shows a zoomed-in rendering of the coupling, which takes place at about 100 μm or less from the tip end. An optical microscope picture of a sputtered Nb SOT coupled to the qPlus prong is reported in Figure 2.21(b). The protruding part of the qPlus prong is about few μm far from the SOT apex.
The oscillation is driven and measured by a Lock-In Amplifier. An AC voltage (in the few mV range) drives the shear piezoelectric stack at the qPlus resonance frequency (about 33 kHz). The qPlus narrow prong vibrates coherently with the shear piezo, while the readout of oscillation amplitude and frequency is done capacitively by two gold stripes on the qPlus prong. A current-voltage converter amplifies the low current signal and then sends it to the input of a Lock-in Amplifier.
The qPlus is used to approach the sample towards the SOT. During this approach, a phase-locked loop (PLL) control allows to monitor frequency and phase of the vibrational mode. When the SOT is far from the sample, the fundamental frequency is constant and attests on a value which depends on the strength of the coupling between qPlus and capillary. Once the tip approaches closer than about 30 nm from the sample surface, van der Waals force interactions provoke a drastic frequency shift, which consequently gives rise to a phase shift. The PLL control allows to safely approach the SOT probe. After approaching as close as 20 nm, the tip is retracted until a distance comparable to the SOT diameter is reached. Longer distances can be chosen due to sample morphology or cleanliness. For more details about this technique, as well as the use of the coupled SOT for AFM measurements, we refer to [95].

Chapter 3

Results

This chapter focuses on the results of a magnetic scanning experiment on a bulk crystal of Cu_2OSeO_3 (copper-oxo-selenite), achieved by using a sub-100 nm diameter SOT made of MoGe.
The first section briefly introduces magnetic skyrmions and topological spin textures and explains their characterization and their potential applications in the field of spintronics. The second section focuses on the chiral magnet Cu_2OSeO_3. Its properties and the reason of interest for this material are summarized, followed by a report of the first experiments at high temperature via LTEM and SANS. Moreover, the first evidence of a low-temperature skyrmion phase via SANS will be discussed.
The third section shows the investigation of different magnetic phases in a bulk crystal of Cu_2OSeO_3, under condition of zero-field cooling (ZFC). The sample preparation and cool down and the SOT characterization are reported and the followed experimental method is explained. The main part presents the experimental results, with real-space images of helical phase, tilted conical phase and field polarized phase. A discussion, even though not conclusive, is made about the possible detection of single and aggregated skyrmions.
The last section shows the data analysis. This is focused on the modulation pitch of the imaged periodic magnetic features, which allows to calculate the angle of the tilted conical modulation with respect to the field axis.

3.1 Magnetic skyrmions

A magnetic skyrmion is a local whirl of the spin configuration in a magnetic material and its existence was firstly introduced by Skyrme in the 1960s to account for the stability of hadrons in particle particles [96].
As described in Figure 3.1, the spins inside a skyrmion progressively rotate with a fixed chirality from the down direction at one edge to the up direction at the centre, and then again to the down direction at the other edge. Many types of skyrmions can be distinguished; among them, typical ones are Bloch-type and Néel-type, for which different symmetries of the interaction between spins result in different directions of rotation [97].
From a topological point of view, a magnetic skyrmion is defined by an integer invariant, called topological charge, whose expression is given by [98]:

$$Q = \frac{1}{4\pi} \int d^2r \left(\partial_x \hat{n} \times \partial_y \hat{n}\right) \cdot \hat{n} \tag{3.1}$$

where $\hat{n} = \vec{m}/|\vec{m}|$ is a unit vector indicating the direction of the local magnetization $\vec{m}$. The topological charge describes how many times magnetic moments wrap around a unit sphere subtended by $\hat{n}(\vec{r})$. For Bloch and Néel skyrmions, the topological charge is $Q = 1$.

Skyrmions are further distinguished by two quantities, called helicity and polarity. Helicity defines the angle of the global rotation around the vertical axis: while for Néel-type skyrmions is null, Bloch skyrmions possess a non zero value. Polarity describes whether the magnetization points up or down at the center of the skyrmion. Both Bloch and Néel skyrmions have equal topological charge and polarity. One type of magnetic texture, for which topological charge and polarity have opposite values is called antiskyrmion (see Figure 3.1(c)).

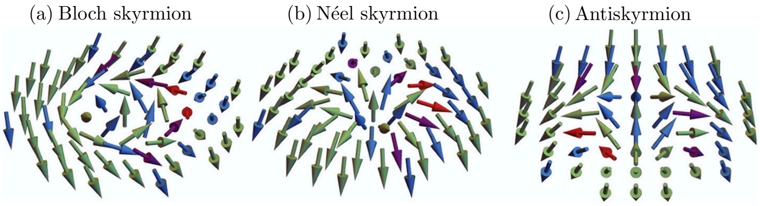
(a) Bloch skyrmion (b) Néel skyrmion (c) Antiskyrmion

FIGURE 3.1: Rotation of the spins in: (a) Bloch-type skyrmion; (b) Néel-type skyrmion; (c) antiskyrmion. In the Bloch-type, the magnetic moment rotates in a plane perpendicular to a radial direction, while in the Néel-type the moment rotates in a plane along a radial direction. Image adapted from [98].

In the case of skyrmions, the normalized magnetization is quantized, in the sense that it can be mapped on a unit sphere and covers the whole sphere (4π). This non-trivial topology leads to important properties. In first place, the spin configuration undergoes a topological protection, which means that the spins cannot be twisted in such a way the topological charge modifies. Even more important, due to their size on the nanoscale, skyrmions behave as particles, which can be moved, created and annihilated. These properties make them suitable for applications in information storage and logic technologies.

Initially, magnetic skyrmions of Bloch-type were identified in chiral B20 compounds with a non-centrosymmetric lattice, such as MnSi [99] and $\mathrm{Fe}_{1-x}\mathrm{Co}_x$ [100]. Their observation was explained by the appearance of the Dzyaloshinskii-Moriya interaction (DMI) [101, 102] induced by spin-orbit coupling. Sufficiently strong DMIs can lead to the formation of isolated skyrmions or a skyrmion lattice.

In a non-centrosymmetric lattice, characterized by a lack of inversion symmetry, spin-orbit coupling can induce an asymmetric exchange interaction, which takes the form:

$$H_{DMI} = \vec{D}_{12} \cdot \left(\vec{S}_1 \times \vec{S}_2\right) \tag{3.2}$$

where $\vec{S}_1$ and $\vec{S}_2$ describe neighbouring spins and $\vec{D}_{12}$ is the Dzyaloshinskii-Moriya vector. The strength of the DMI is directly proportional to the intensity of the spin-orbit interaction, which is expected to scale with the fourth power of the atomic number.

In the case of thin magnetic films, magnetic skyrmions can be studied by starting from the free energy written for a 2D ferromagnet below the Curie temperature [98]:

$$F = \int \mathrm{d}^2 r \left[A\left(\partial_i \hat{m}\right)^2 - K m_z^2 - H m_z + \vec{D}_j \cdot \left(\partial_j \hat{m} \times \hat{m}\right)\right] \tag{3.3}$$

where summing over repeated index i,j = x,y is assumed and $\hat{m}$ is a unit vector indicating the magnetization direction. In order, the first contribution in Eq. 3.3

describes isotropic exchange, with exchange stiffness parameter A; the second term expresses uniaxial anisotropy with strength K; the third contribution is the Zeeman energy due to the external magnetic field; the last term refers to the DMI and is the most important one for the formation of magnetic skyrmions.
By minimizing the free energy in Eq. 3.3, a phase diagram can be obtained, where boundaries separate different magnetic phases, such as spiral phase, ferromagnetic phase or hexagonal skyrmion lattice. The parameters A, K, H, D determine whether a skyrmion phase is energetically favorable. In fact, a critical DMI strength can be introduced, $D_c = 4(AK^{1/2}/\pi)$, close to which isolated skyrmions transition to a skyrmion lattice. Moreover, the magnetic skyrmion size at $D < D_c$ varies with the strength of the DMI, as $R_s \approx \sqrt{AD_c/2K(D_c - D)}$.

The last part of the introduction concerns the applications of magnetic skyrmions. Since their discovery, thanks to the topological protection and the potential to achieve small size, magnetic skyrmions were proposed to be used in the field of communication and information storage. In fact, the skyrmion motion can be easily driven by an electric current and the nonvolatility property reduces the heat generation and standby energy consumption while processing and transporting the information. To the aim of using magnetic skyrmions in electronic devices, a certain number of key ingredients is required: writing, meaning the capability of nucleating individual skyrmions; processing or manipulating, which involves displacement, creation, annihilation and excitation of skyrmions; reading, which consists in electrical detection of individual skyrmions. All these elements were already demonstrated, at least at low temperatures and for skyrmion lattices. The challenge is to succeed in achieving all the ingredients at room temperature and for single skyrmions, using electrical schemes to build compact, integrated devices. In the following some well known systems will be mentioned, such as skyrmion racetrack memories, skyrmion logic devices and skyrmion magnonic crystals. For further reading about this topic, including schematic images of possible devices, we refer to [97, 103].
Skyrmion racetrack memories are considered as a promising technology for mass storage applications, where data information is encoded in a magnetic track in the form of a sequence of skyrmions. The concept is similar to the one based on domain walls [104], even though skyrmions show some advantageous. In first place, by reducing the track width, skyrmions size can be compressed, in such a way a high information density is reached. For what concerns the skyrmion motion, this is induced by spin transfer torque and it is expected to behave similarly in straight and curved tracks, and with low energy consumption. Moreover, the skyrmion motion along the track can be detected via tunnel magnetoresistance devices or topological Hall effect. A further step in complexity is achieved by incorporating a gate inside the magnetic nanotrack [105]. By applying a gate voltage, the skyrmion motion can be denied or allowed, leading to a prototype of spin-polarized current-driven skyrmion transistor.
Skyrmion-based logic gates arise from the behavior of skyrmions as independent particles. Starting from the demonstration that an individual skyrmion can be converted into a domain walls pair and viceversa, a prototype of skyrmion-based logic device was proposed, such as AND and OR gates, which allows to perform basic Boolean logic computing operations [106]. The idea is to replace spin logic devices by building a logical architecture that combines their same functionality with a high level of integration.
Magnonic crystals are artificial magnetic media with properties characterized by periodic lateral variation, relying on magnons, which are the quanta of spin waves.

Magnons can propagate in magnetic materials with wavelengths at the nanometer scale and carry data information in terms of angular momentum [107]. For this reason, magnonic crystal are proposed to be used as future nanometric size data carriers, with the capability to process information with extremely low loss. In conventional magnonic crystals, the periodic modulation of the magnetic properties inside the medium is achieved by lithographic processes. Analogous systems can be realized, in which skyrmion lattices are used to modify the spin wave propagation [108]. The advantage offered by skyrmions is to establish dynamical magnonic crystals, where the periodicity of the lattice can be changed or removed and the skyrmion size can be tuned by applying an external magnetic field. The dynamics takes place on sub-nanosecond time scale, allowing for unique, fast switching functionality.

3.2 Chiral magnets and Cu_2OSeO_3

Here we focus on the properties of chiral magnets of the so called B20-type compounds. Representatives of this category are transition metal monosilicides and monogermanides, such as MnSi, $Mn_{1-x}Co_xSi$, $Mn_{1-x}Fe_xSi$, $Fe_{1-x}Co_xSi$, MnGe, FeGe and the insulator Cu_2OSeO_3. All these compounds crystallize into the chiral cubic lattice structure in the space group $P2_13$, with lack of inversion symmetry.

Despite identified by different electronic structure and different characteristic quantities, such as magnetic modulation period, magnetic transition temperature and transition field, the B20-type compounds all show a long-wavelength helimagnetic order. This arises from a well separated energy hierarchy in the magnetic interactions which lead to the formation of a skyrmion lattice [109, 110]. In order of decreasing magnitude, the three interactions are ferromagnetic exchange interaction, DM interaction, and magnetocrystalline anisotropy. Exchange interaction, on the strongest energy scale, favors a parallel spin alignment. Due to the lack of inversion symmetry of the lattice structure, DM spin-orbit interaction arises and favors perpendicular spin alignment. Magnetocrystalline anisotropy is a higher order spin-orbit coupling term and affects the direction of propagation of the helical modulations.

The consequence of this hierarchy is that B20-type compounds share a common magnetic phase diagram, which is sketched in Figure 3.2(a), as function of normalized magnetic field and temperature. At temperatures above the transition temperature T_c, typically at few tens of K, the magnetic state is exchange enhanced paramagnetic. When $T < T_c$, at zero magnetic field a long wavelength helical structure appears due to the mentioned competition between exchange interaction and DM interaction. This multidomain state consists of helices propagating in different directions along one of the crystalline axes, where the helical propagation vector is set by weak cubic magnetic anisotropies. The arrangement of spins in the helical state (image adapted from [111]) is shown in Figure 3.2(b), where [001] and [111] are possible crystalline axes along which the helical state is modulated.

When a magnetic field, bigger than the critical field B_{c1}, is applied, the helical state transforms into the conical state. This means that, while twisting helically along the field direction, the spins tilt towards the field direction. In this way, a spin disposition deformed like a cone is achieved, displayed in Figure 3.2(c) (image adapted from [111]). When the applied magnetic field overcomes the transition field B_{c2}, spins evolve into a field-polarized state, where they all align with the field direction.

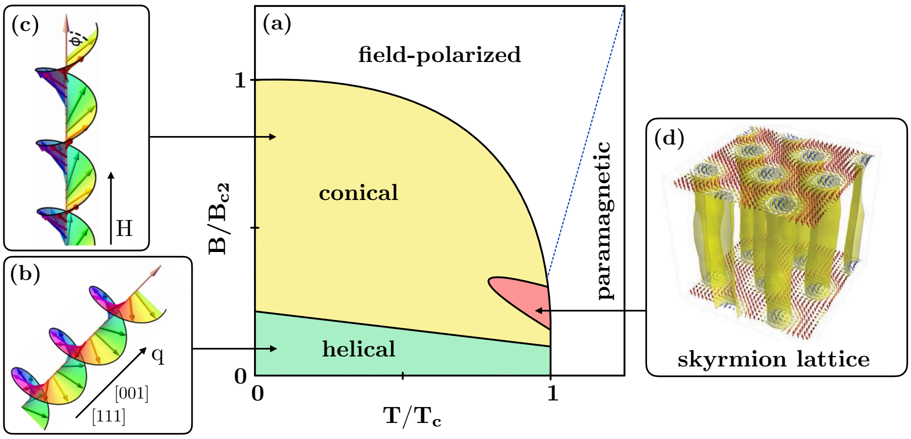

FIGURE 3.2: (a) Typical magnetic phase diagram of cubic chiral magnets, reported as function of normalized temperature and magnetic field, where different phases can be distinguished. On the left, the schematic spin structures of the helical (b) and conical state (c), adapted from [111]. (d) Representation of skyrmion lattice, from [112], where spin whirls are arranged in a regular lattice. The skyrmion lattice phase is found in a narrow T-B pocket close to the critical temperature.

Special attention is reserved to the skyrmion lattice phase, sometimes also called A-phase, which is localized in a small T-B phase pocket above B_{c1} close to the transition temperature T_c. The size of the pocket is changing based on sample thickness, with thin magnetic fields characterized by wider pockets and bulk materials by smaller ones. In this phase, skyrmions are disposed in a regular hexagonal lattice, as reported in Figure 3.2(d) (image from [112]), where the lattice constant is depending on the material. The first experimental evidence of a skyrmion lattice was reported in 2009 [99] in a bulk sample of MnSi, in the reciprocal space using the SANS technique. The first real space observation of a skyrmion lattice was presented in 2010, via LTEM on a thin film of $Fe_{0.5}Co_{0.5}Si$ [100].

Cu_2OSeO_3 (copper-oxo-selenite) is the first insulating material that was proved to host magnetic skyrmions [10]. Furthermore, skyrmions in this material were demonstrated to exert a strong magnetoelectric effect, which means that they can cause electric polarization and at the same time an electric field can modify their magnetic order. Since the energy dissipation due to an applied electric field is negligible in insulating materials, the possibility to manipulate skyrmions in Cu_2OSeO_3 by an external electric field without energy loss due to Joule heating has attracted great interest in the last years.
Copper-oxo-selenite belongs to the space group $P2_13$, even though its crystalline structure is more complex compared to the one of other B20-type transition metal compounds. Its structure is reported in Figure 3.3(a). Cu^{2+} ions, with spin $S = 1/2$, are located at two sites: three-quarters are surrounded by square pyramids of oxygen ligands, visible as green balls and tetragons, while one-quarter are surrounded by trigonal bipyramids, in blue color. As a result of ferromagnetic and antiferromagnetic interactions, a three-up, one-down type of ferrimagnetic spin structure defines the magnetic ground state below 60 K [10].
Cu_2OSeO_3 has a critical temperature $T_c \simeq 58$ K, below which a long period helical order manifests as a balance between ferromagnetic exchange and DM interaction, with a pitch of 60 - 70 nm. Below T_c, helices align parallel to the [100], [010], [001]

crystallographic directions. When B is increased above B_{c1}, the anisotropy is overcome by the applied field and helices get oriented along the direction of the field, leading to the conical phase. For $B > B_{c2}$, the DM interaction and helical correlations get suppressed and the field polarized state is achieved. A high temperature skyrmion lattice phase is found in a narrow pocket close to T_c.

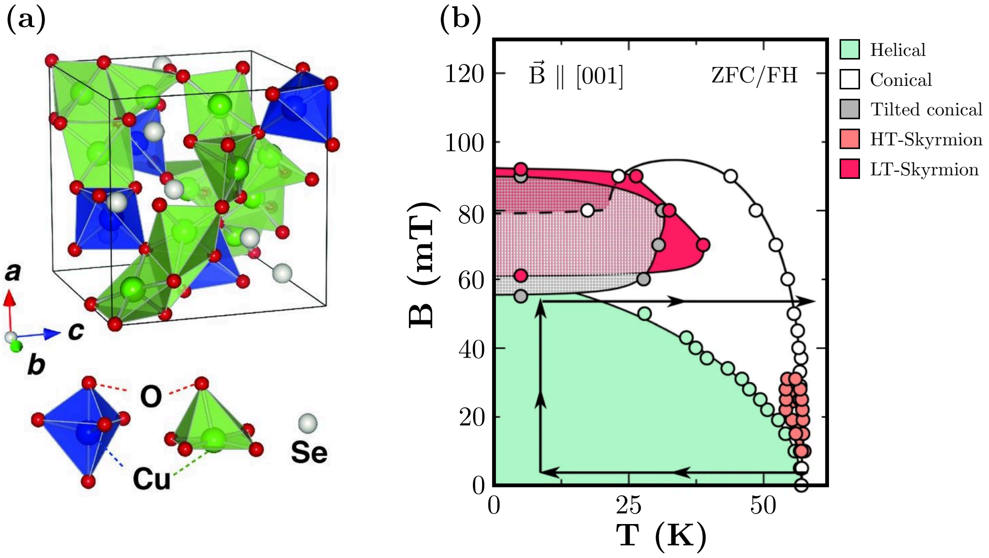

FIGURE 3.3: (a) Cu_2OSeO_3 crystalline structure, from [10]. (b) Copper-oxo-selenite phase diagram, measured via SANS by Chacon et al. [11], where helical, conical, tilted conical, high-temperature skyrmion phase, low-temperature skyrmion phase can be distinguished. The low-temperature skyrmion phase is found under condition of zero field cooling, when a magnetic field is applied parallel to the [001] crystallographic direction.

The first experiments on this material were performed recently, in 2012, via LTEM on thin samples [10] and via SANS on bulk crystals [113, 114]. The SANS studies focused on reconstructing the phase diagram, by identifying the helical and conical phases and the high temperature skyrmion phase below T_c (called A-phase). LTEM experiments require 100 nm thin films, for which the A-phase is extended to a much wider T-B pocket. Other interesting studies by SANS are [115, 116], where the strong magnetoelectric coupling is used to switch between topologically distinct phases and induce rotation of the skyrmion lattice by an electric field. Another work [117] combines SANS with magnetization measurements and observes a new high-field multidomain magnetic state, stable over a broad temperature range, that intervenes between the conical and field polarized state.

More recent experiments focused on investigating magnetic phases of Cu_2OSeO_3 at low temperatures. A scanning probe experiment via MFM can be mentioned [118], where the reorientation process between helical to conical phase at 10 K for magnetic fields parallel to the [110] direction is investigated. MFM allowed to obtain real-space images of these phases close to B_{c1} and observe the formation of domains and relaxation events that accompany the reorientation process.

A key experiment is the one by Chacon et al. [11], performed via SANS, where a second skyrmion phase in Cu_2OSeO_3 is identified, at low temperature, in presence of an applied magnetic field. While the high temperature skyrmion phase is stabilized by thermal fluctuations, the new skyrmion phase only manifests when the external magnetic field is oriented parallel to the [001] crystallographic direction.

The low-temperature skyrmion phase is proved to be highly hysteretic and thermodynamically stable, at the interface between conical and field-polarized state, and it is accompanied by a regime in which the conical modulation progressively tilts away from the field direction. The SANS observations are presented together with a theoretical analysis, that demonstrates that magnetocrystalline cubic anisotropies, being nonlinear in the magnetization squared, can stabilize topologically non trivial phases in presence of a magnetic field. The low-temperature skyrmion phase was studied by following different temperature vs field protocols, such as zero-field cooling/field heating, field cooling and high-field cooling/field heating. An example is reported in Figure 3.3(b), for the case of zero-field cooling/field heating, which is the same protocol that is used in the SOT scanning images shown in the following section. We can distinguish the helical phase (in green color), the conical phase (in white color), the tilted conical phase (in grey color) and the low temperature skyrmion phase (in red color). The phase diagram highlights the requirements in order to investigate skyrmions in Cu_2OSeO_3 using SSM. Under zero-field cooling the temperature setpoint has to be below 30 K. For what concerns the applied magnetic field, this is limited to a 20 mT range around a field of 80 mT. The skyrmion lattice constant is expected to be about 60 - 70 nm, so a SOT with a diameter comparable or smaller is required to have enough spatial resolution to resolve single skyrmions.

3.3 Investigation of magnetic phases

The aim of the experiment is to provide real-space images of different magnetic phases in a bulk crystal of Cu_2OSeO_3. The SOT technique allows to investigate the magnetic behavior of the bulk sample and eventual contributions from the surface at temperatures up to 5 - 6 K and in presence of external magnetic field, with low invasiveness for the crystal. The spin confguration is investigated by measuring the DC stray magnetic field component projected along the z axis.

By referring to the phase diagram presented in Figure 3.3, close to zero temperature we can distinguish different magnetic phases: in order from lower applied magnetic field, helical phase, conical and tilted conical phase, low-temperature skyrmion phase, and field-polarized state. Understanding how the bulk crystal switches from one phase to the other and imaging the evolution of the spin configurations in real-space are new contributions that add to the wide investigation performed on this chiral magnet in the last 10 years.

Ultimately, the most challenging goal is to look for the low-temperature skyrmion phase, located in a narrow pocket close to the transition between tilted conical phase and field polarized state. Studying the formation of skyrmions and the way single skyrmions aggregate in clusters or in a ordered lattice would be a result of extremely high impact.

3.3.1 Experimental method

Here, divided in different topics, a guide of the experiment is provided, with informations about the ^{3}He cryostat, crystal growth and preparation of the sample, sample cool down, SOT characterization and magnetic field vs temperature protocol followed in the experiment will be provided.

The cryostat used in the experiment is a ^{3}He type. The core of the scanning probe setup is the same described in Sec. 2.6 and Figure 2.20. The ^{3}He cryostat, produced by Janis Research Company, differs from the more standard, 4.2 K, cryostats by including a ^{4}He bath, in which a inner vacuum chamber (IVC) is placed. The IVC encloses the UHV sample chamber and the SSAA. This vacuum shell allows to thermally decouple sample chamber and ^{4}He bath and affords to regulate the temperature at the sample stage independently of the ^{4}He bath. In order to cool down the sample below 4.2 K, two sources of cooling power are used, a 1 K pot and a ^{3}He line. The 1 K pot is a separated reservoir of ^{4}He placed inside the IVC, which is kept at low pressure by pumping ^{4}He from the main bath. The pumping process cools the ^{4}He down to a temperature of 1 K. This stage provides cooling power to both sample chamber and ^{3}He line. The final cooling power is provided by a ^{3}He line, where the gas is pumped in a closed loop through a cold trap (for cleaning the gas from impurities) and it condenses on the cold surfaces of the thin-walled pumping tube (called impedance coil) leading to the ^{3}He pot. This pot, collecting liquid ^{3}He, is the coldest stage of the cryostat and usually reaches a temperature of about 300 mK. The sample stage, slightly warmer, gets to about 400 mK. The thermal decoupling between ^{4}He bath and UHV chamber allows to use heaters controlled via PID loop to stabilize the sample and SOT over a wide temperature range, between 400 mK and few tens of K, in short time. The IVC is surrounded by a superconducting magnet (Cryomagnetics), made of a NbTi/Cu coil cooled down to 4.2 K. The magnet allows to apply an external magnetic field up to 6 T along the z direction.

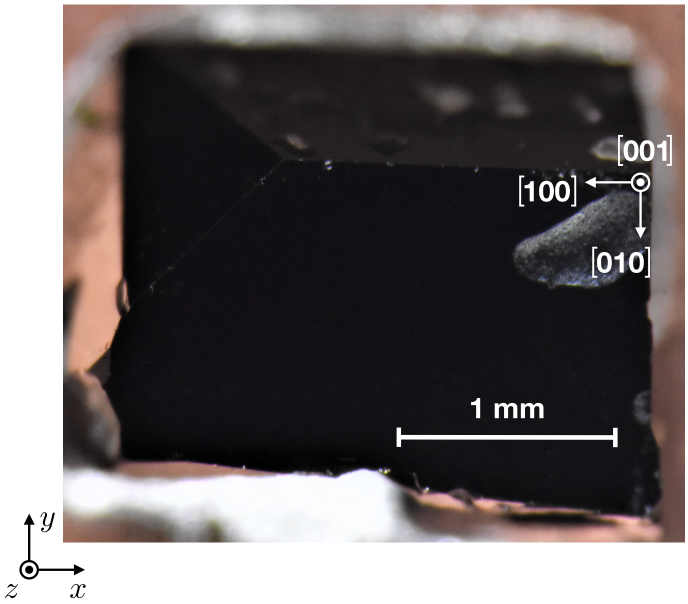

FIGURE 3.4: Optical microscope picture of a bulk crystal of Cu_2OSeO_3, grown by chemical vapor deposition in the Crystal Growth Facility at EPFL. The crystal has lateral dimensions of 2.4 mm × 1.9 mm, and a thickness of 1.1 mm and is glued on top of a copper sample holder. The crystallographic directions are [100], [010], [001]. After the growth, the top surface is polished for SPM experiments.

The investigated sample is a bulk single crystal of Cu_2OSeO_3, grown by chemical vapor deposition. The growth was performed in the Crystal Growth Facility at

EPFL, led by Dr. Arnaud Magrez, by our collaborators in the network ”Nanoskyrmionics”[1]. The crystal, whose optical microscope image is reported in Figure 3.4, has in-plane dimensions of 2.4 mm × 1.9 mm and thickness of 1.1 mm. The crystallographic directions are [100], [010], [001]. After the growth, the surface was polished, in order to minimize the roughness and be suitable for a SPM experiment with less risk of damaging the sensor while approaching the surface. The crystal was glued with conductive silver paint on a flat, copper sample holder. The copper holder maximizes the thermal coupling between the titanium probe frame and the crystal.

The cooling process from room temperature down to 400 mK is about two days long. The SOT, mechanically coupled to the qPlus resonator, is optically aligned above the sample at a distance of few tens of micrometers. This is a safety procedure, to avoid potential damages to the sample, due to thermal contractions during the cool down or mechanical bumps while closing the cryostat dewar. The first part of the cool down consists in pumping both UHV chamber and IVC, while the ^{3}He gas circulation at room temperature is tested. When a vacuum of 10^{-6} mbar is reached, the outer dewar is closed and the main bath is filled by liquid nitrogen. This is a fast, not expensive way to cool the main bath, IVC and UHV space down to a temperature of 80 K. At this stage, liquid nitrogen is pushed out by using ^{4}He gas and the main bath is filled by liquid ^{4}He. To the aim of having a better thermal coupling between main bath and UHV chamber, the IVC is filled by ^{4}He gas at low pressure (few mbar at 80 K). As a result, in a couple hours, the temperature drops from 80 K to about 20 K. At this point, exchange gas is pumped out and the cooling power from the 1K pot and ^{3}He is used to drop the temperature to the mK regime.

Once temperature stabilizes at 400 mK, the SOT is characterized, in the way shown in Sec 2.4, by using the setup described in Sec. 2.3. For this experiment, a MoGe SOT was chosen. There are two reasons behind this choice. In first place, Cu_2OSeO_3 is characterized by a helical order with a pitch of 60 - 70 nm, so a small diameter SOT is required. MoGe proved to be extremely reliable for fabricating SOT, even when the diameter is reduced. The drawback is that MoGe offers the lowest magnetic response among the three materials tested so far; however, magnetic phases in crystals such as Cu_2OSeO_3 are expected to produce rather high DC stray fields of 100 μT or higher, comparable to stray fields from superconducting vortices [90] or spin ice samples [92]. A initial characterization reveals that the MoGe SOT has a period in the interference pattern of 290 mT, corresponding to a effective diameter of 95 nm; a minimum of the interference pattern is located around 48 mT, which determines a lack of sensitivity in the range of applied field from 40 mT to 55 mT. The diameter is slightly bigger than the helimagnetic wavelength, which might not allow to achieve the fully resolve certain features, such as the ordered skyrmion lattice. However, it should be small enough to detect a modulation of the stray field in case the SOT is approached close to the crystal surface.
The initial characterization is useful to find the temperature at which the magnetic response is maximized. In fact, after being fabricated, the SOT are tested at 4.2 K, and properties drastically change when cooling the temperature down to 400 mK. The critical current increases and, depending on the combination of I_c and R_{SOT}, the I-V characteristic becomes hysteretic and the transition of the SOT to the normal state gets sharp. This reduces the range of (V_{bias},B_a) points where the SOT can be

---

[1] Interdisciplinary Sinergia project 171003 funded by the Swiss National Science Foundation (2017 - 2022), led by Prof. Dirk Grundler, EPFL. More informations about the network and publications can be found at https://www.epfl.ch/labs/lmgn/skyrmions/

locked to perform magnetic scanning. For this reason, the target temperature is the lowest one at which the *I*-*V* characteristic is not hysteretic. For the 95 nm diameter SOT used in the Cu_2OSeO_3 experiment, this temperature corresponds to 1.8 K.

The experiment requires to follow a temperature vs applied magnetic field protocol. As described in the work by Chacon et al. [11], the magnetic phases in Cu_2OSeO_3 are observed to be highly hysteretic, in such a way transitions of spin configurations from one phase to the other happen at unconsistent magnetic fields if B_a is ramped up and down. To avoid the crystal building a memory of the magnetic field history, a strict temperature vs magnetic field protocol must be followed. By referring to [11], we choose to perform ZFC, whose corresponding phase diagram is shown in Figure 3.3. An initial ramping of the magnetic field is required to characterize the SOT properties. After achieving this information, the magnetic memory of the crystal is erased, by heating the UHV chamber up to 65 K and then cooling it down to 1.8 K.

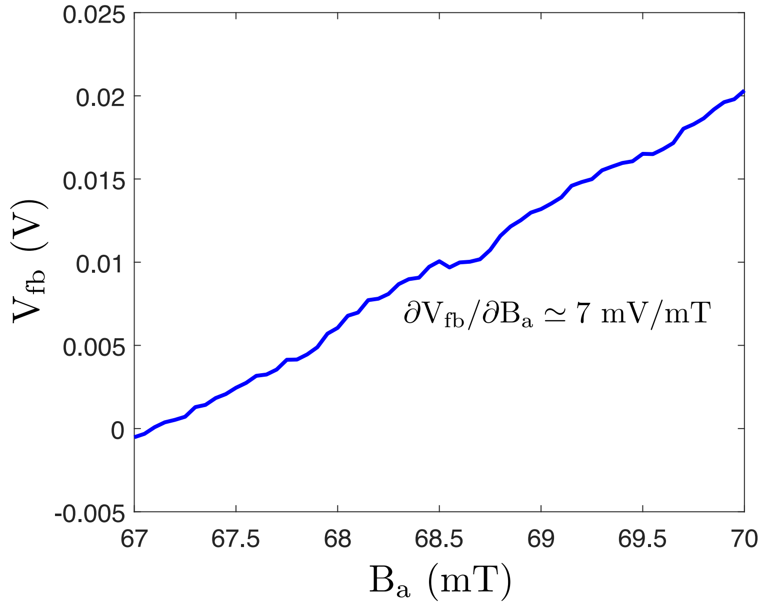

FIGURE 3.5: A *B*-*V* characterization for the MoGe SOT used in the Cu_2OSeO_3 investigation. The characterization is done by biasing the SOT with a fixed I_{bias} and recording V_{fb} output by the SSAA in a small range of applied field B_a. The first derivative of the curve corresponds to the SOT magnetic response.

After the second ZFC, the magnetic field is ramped only upwards. Before every scan, the value of V_{bias} is set accordingly to the initial *I*-*V* data, and then a *B*-*V* characterization is measured. This consists in setting a fixed value of V_{bias} and switching B_a in a small range, while the feedback voltage output by the SSAA is recorded. Typically, V_{fb} is filtered by a Stanford Research systems SR560 low-noise pre-amplifier, which has a tunable cutoff frequency. The field range of the *B*-*V* measurement is chosen in such a way a magnetic scan is performed at the final magnetic field value. This characterization is shown in Figure 3.5, for the magnetic field range from 67 mT to 70 mT. The derivative of V_{fb} with respect to B_a, $\partial V_{fb}/\partial B_a$, calibrates the magnetic response function. In this specific magnetic scan, the magnetic response function is about 7 mV/mT. When scanning over the crystal at a specific magnetic field, a 2D map of V_{fb} data is recorded by a lock-in amplifier, and the magnetic response function is used to convert the voltage data into stray magnetic field data.

The last point regards the method used to approach the SOT sensor close to the crystal surface. In the ^{3}He cryostat, the sample holder is mounted on top of a set of x-y-z nanopositioners (Attocube ANPx311 model), which have a titanium body and offer a 6 mm travel range and the capability to hold a load up to 2 Kg. The z positioner also works as a scanner, with a travel extension of 2 μm and a sub-nm precision. In the x-y plane, the fine movement is performed via a set of scanners (Attocube ANSxy100), which give a 30×30 $\mu\mathrm{m}^2$ scanning window and a sub-nm precision.
In Sec. 2.6.1 a technique to approach the crystal surface mechanically was discussed, based on coupling a qPlus tuning fork close to the SOT apex. Unfortunately, due to technical issues related to the shear piezo driving the qPlus oscillations below 4.2 K, in the Cu_2OSeO_3 experiment we could not take advantage of the coupling between SOT and qPlus. Therefore, the approach was done by measuring the DC V_{fb} signal, while slowly moving the crystal towards the SOT. The z scanner is extended, at a speed of about 10 - 20 nm/s, while the DC voltage output by the SSAA is recorded by a lock-in amplifier. At the end of the 2 μm extension, the scanner is retracted and the z nanopositioner is used to step the crystal towards the SOT. The number of steps is chosen is such a way the movement covers about 60 - 80 % of the scanner extension. This process is reiterated until the crystal to SOT distance gets less than 2 μm. In this case, while extending the z scanner, a rapid increase of the DC V_{fb} signal is measured, corresponding to the stray field of the sample under investigation. The crystal is retracted, and a new extension procedure is repeated, to verify that the increase of the signal is consistent. The final part of the approach consists in manually extending the z scanner by few nanometers at the time and scanning over the crystal surface, until magnetic features appear and a good spatial resolution is obtained.
Due to the absence of the qPlus, it is hard to precisely measure the crystal to sensor scanning distance. We estimate a distance in between 100 nm and 200 nm, based on the fact that the DC stray field was considerably changing when approaching the sensor by 5 - 10 nm. A limitation for the closest achievable distance is given by the intensity of the signal. When approaching the SOT too close to the crystal surface, the signal saturates, due to the fact that the sample stray field changes the working point of the SOT into a condition where the SOT has less or even zero magnetic response. For this reason, the scanning distance is chosen as the closest one at which this phenomenon does not take place.

3.3.2 Scanning results

After ZFC to 1.8 K, Cu_2OSeO_3 is in the helical magnetic phase. By referring to the sketch shown in Figure 3.2, the helical phase corresponds to a configuration where spins rotate around the q vector, which due to the cubic symmetry of the crystal is oriented parallel to the [100], [010], [001] directions. The first two are in-plane directions, while the third one is along the z axis.
The DC stray magnetic field sensed by the SOT is the projection B_z of the stray field along the z axis. This means that the spins rotating around $q \parallel [001]$ only have in-plane component and give a zero contribution to B_z. On the other hand, the spins rotating around $q \parallel [100]$ and $q \parallel [010]$ both give a nonzero contribution. If considering a perfect crystal surface, with no defects that could act as pinning points and alter the spin configuration, the expected B_z signal is the sum of the stray fields from

the helices rotating around [100] and [010] orientations. When taking into account a realistic surface, with defects, the helical phase projected along z should provide a kind of magnetic background, with regions of positive and negative B_z, without well defined features.

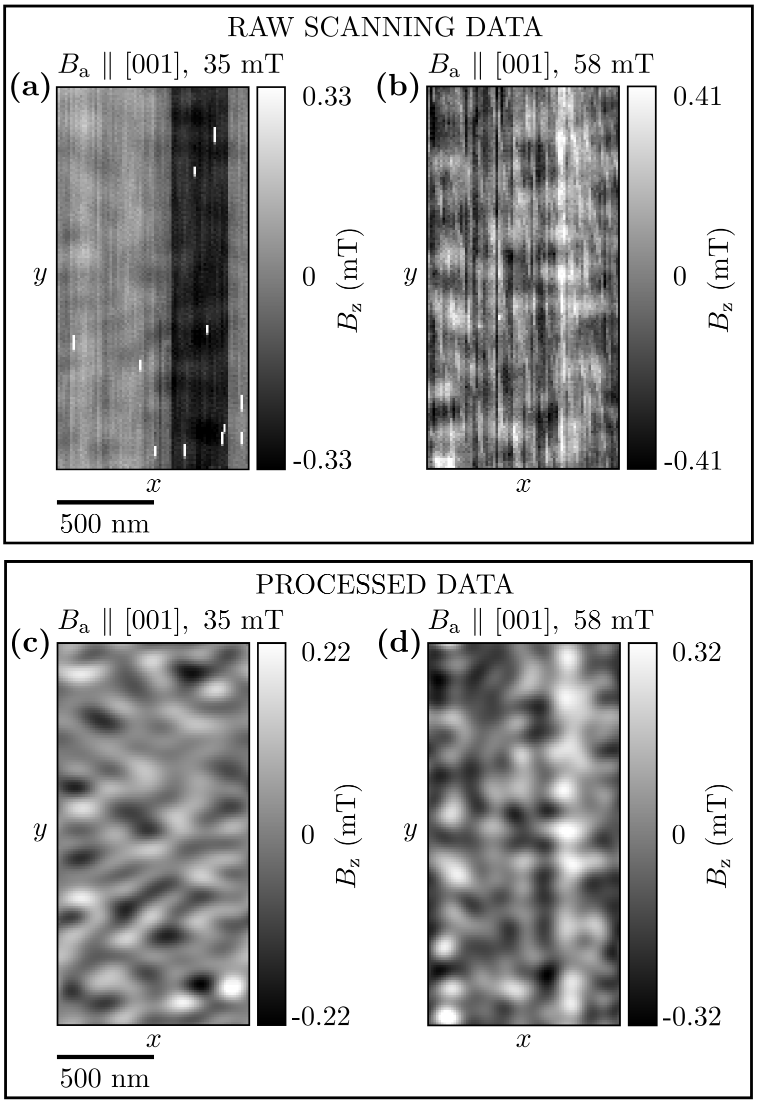

FIGURE 3.6: Real-space, 1 μm × 2 μm wide, magnetic images of the Cu_2OSeO_3 bulk crystal in the helical phase, at 1.8 K and under ZFC protocol, when an external field is applied in the z direction, parallel to the [001] crystallographic direction. In all images, the DC magnetic signal is centered around zero. (a),(b) raw scanning data, where steps and jumps in the DC magnetic signal can be observed. This is due to external interference on the SSAA, which provokes a change in the locking point. The physical information remains encoded in the data file, but requires a treatment in order to be correctly visualized. (c),(d) DC magnetic signal, after being processed via 2D FFT and step correction functions. The images show a magnetic background, with no particular features in it. The background is the result of the spins rotating in helices around q vectors oriented along [100], [010] and [001] crystallographic directions.

The helical phase was imaged from zero field up to 58 mT, where the value of magnetic field is not corrected by the demagnetization field. Images were acquired with steps of few mT, with the exception of a gap between 41 mT and 54 mT due to lack of magnetic response of the SOT. In every scan, a pixel size of about 10 - 20 nm is chosen and an integration time for every pixel of 300 - 500 ms, combined to an amplification factor 10, is used to increase the signal to noise ratio. Every scan is about 3 - 6 hours long, depending on the size of the scanning window.

Two images, 1 μm $\times$ 2 μm wide, taken at different magnetic fields are presented in Figure 3.6. For clarity, Figure 3.6(a),(b) report the raw signal measured by the lock-in amplifier. Figure 3.6(c),(d) show the same scanning area, after the signal is processed. There are few sources of noise: for instance, the white vertical lines are temporary jumps of the DC signal, due to a change in the FLL working point of the SSAA, caused by external interference. On top of this, there can be shifts of the DC signal, as visible in Figure 3.6(a). Jumps and shifts of the signal do not hide the physical information about the magnetic phase under investigation, but they make the understanding of the image more difficult by altering the natural colorscale of the 2D scan. Other distorsions in the scan arise from the pixel size, which give diverse contributions along the fast y axis and the slow x axis.

In order to treat the signal, few functions in the Gwyddion software are used. In first place, a step correction function is used to eliminate significative signal shifts and level the data. After that, a 2D Fast Fourier Transform (FFT), using a Hann windowing function, is applied to distinguish contributions to the scan having different frequencies. In this way, it is easy to preserve the original signal contrast and cancel the distortions from pixel size and jumps caused by external interference. As a last step, the stray field is centered around zero.

The final results for the real-space images relative to the helical phase are visible in Figure 3.6(c),(d). The stray magnetic field does not show any particular feature due to the helices rotating around the q vectors and the magnetic background has a range of about half a mT.

When B_a is increased from 58 mT to 61 mT, the spin configuration undergoes a transition from helical phase to tilted conical phase. This completely changes the stray magnetic field component projected along the z axis. In fact, the spins tilt towards the field direction, in such a way a disposition with conical shape is achieved. Moreover, the q vector does not remain aligned to the magnetic field axis, but tilts by a certain angle θ.

At $B_a = 61$ mT, periodic magnetic features appear. To prove that they are not an artifact due to the scanners, basic tests were performed: comparing the forward and backward data, inverting the slow and fast scanning axes and ultimately moving the scanning window to see if the feature coordinates change accordingly. Four images at increasing values of B_a are reported in Figure 3.7(a)-(d). The scanning window of 3 μm $\times$ 3 μm is obtained by stitching three individual scans together, each of them taking about 3 - 5 hours. The stitching is made by overlapping two objects that appear in two adjacent (and slightly overlapping) scanning windows. The stitching process allows to limit the time required for every scanning window, during which there can be shifts of the laboratory temperature or other phenomena that would make a long scan inconsistent. In all the images, signal processing is used to filter the noise out, as discussed for the helical phase data. The DC stray field has a range of about 1.5 mT and the magnetic features appear periodically in space, with a pitch of 1.6 - 2 μm. The period of the magnetic modulation has a specific physical meaning, which is discussed more in details in Sec. 3.4. The reason why the features are oriented more parallel to the x axis is due to the shape anisotropy of the crystal. In fact, by looking at Figure 3.4, it is clear how the crystal does not have a perfectly square top surface, but instead it has a rectangular surface, with the longer edge in the x direction. This determines the preferential orientation of the magnetic features.

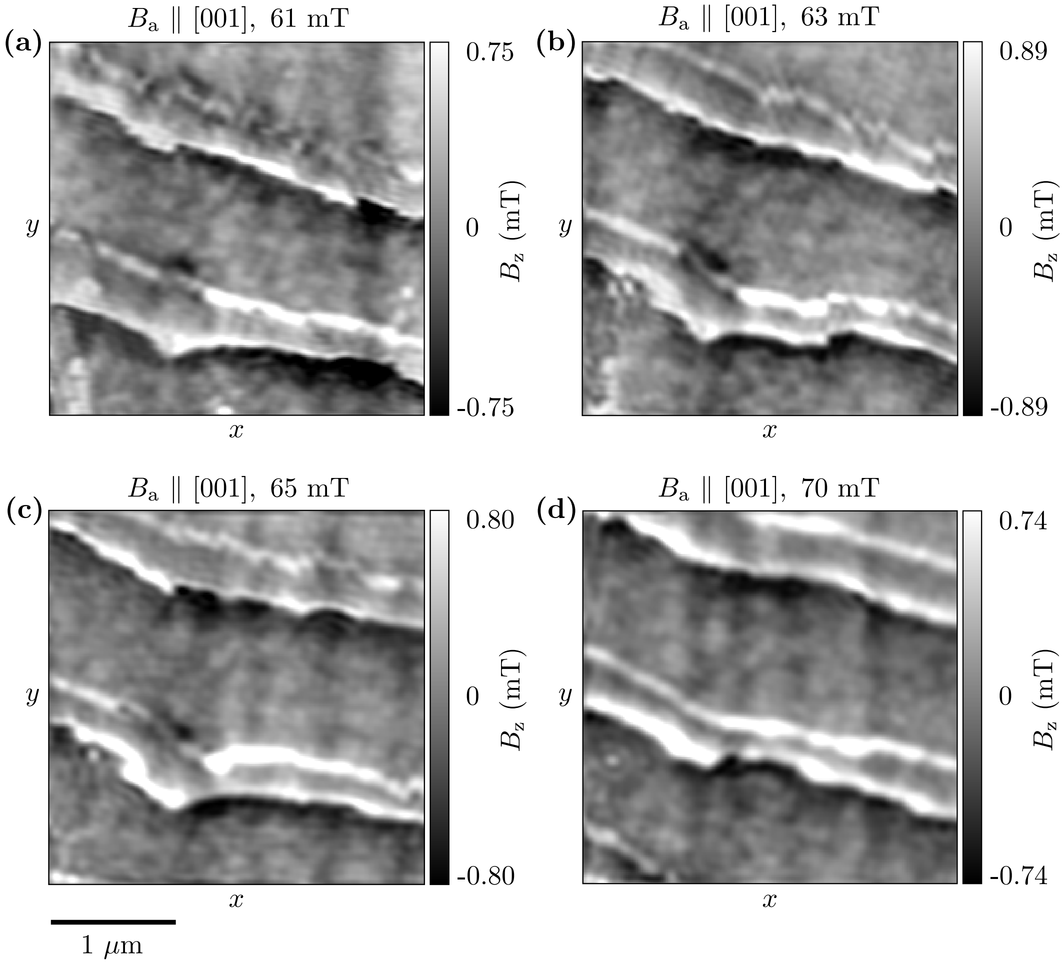

FIGURE 3.7: Real-space, 3 μm × 3 μm wide, magnetic images of the Cu_2OSeO_3 bulk crystal after the transition from helical to tilted conical phase, at 1.8 K and under ZFC protocol, when an external field is applied in the z direction, parallel to the [001] crystallographic direction. (a) $B_a = 61$ mT; (b) $B_a = 63$ mT; (c) $B_a = 65$ mT; (d) $B_a = 70$ mT. In all images, the DC magnetic signal is centered around zero. The transition to tilted conical phase takes place in between 58 mT and 61 mT, and manifests with the appearance of magnetic features, repeating with a periodicity of 1.6 - 2 μm.

When increasing B_a from 70 mT to 73 mT, a significant change in the magnetic features is noticed, as highlighted by the scanning images in Figure 3.8(a)-(f), where B_a ranges from 73 mT (a) to 113 mT (f). All images show a scanning window of 2 μm × 1 μm, where the fast scanning axis is along y and the slow scanning axis is along x. Each scanning takes approximately 5 hours, because a very small pixel size (13 nm) is chosen. The DC stray field has a range of 1 - 2 mT and, due to the crystal shape anisotropy, the magnetic textures have an orientation more aligned to the x axis.

A big difference can be noticed between Figure 3.7 and Figure 3.8, where the modulation pitch changes from 1.6 μm (Figure 3.7(d)) to 190 nm (Figure 3.8(a)). The pitch further reduces while increasing B_a, until a minimum value of 143 nm is found

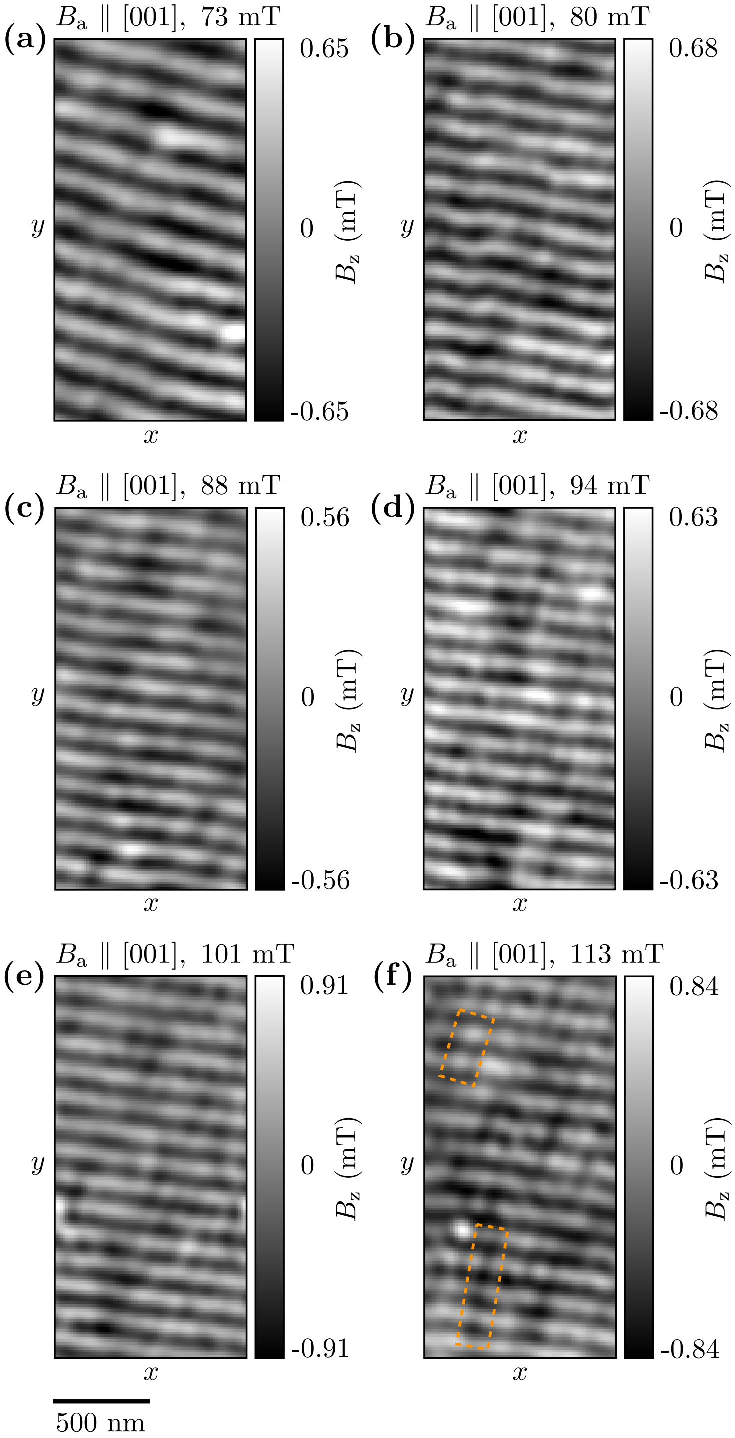

FIGURE 3.8: Real-space, 1 μm × 2 μm wide, magnetic images of the Cu_2OSeO_3 bulk crystal in the tilted conical phase, at 1.8 K and under ZFC protocol, when an external field is applied in the z direction, parallel to the [001] crystallographic direction. In all images, the DC magnetic signal is centered around zero. The modulation pitch is strongly reduced and varies with the applied field. (a) $B_a = 73$ mT, pitch 190 nm; (b) $B_a = 80$ mT, pitch 156.6 nm; (c) $B_a = 88$ mT, pitch 145.2 nm; (d) $B_a = 94$ mT, pitch 143 nm; (e) $B_a = 101$ mT, pitch 143 nm; (f) $B_a = 113$ mT, pitch 143 nm. The orange stepped line marks regions where skyrmion-like features are observed, disposed in straight lines.

at $B_a = 94$ mT. This can be visualized in Figure 3.8(a)-(d). Above 94 mT, no changes in the modulation pitch are observed anymore, until the tilted conical phase transitions to the field polarized state.

Starting from Figure 3.8(c), the magnetic stripes are accompanied by the presence of circular features, whose diameter is estimated to be around 60 - 70 nm. These dots are more visible while keeping y as the fast scanning axis, due to the fact that the stripes are almost orthogonal to the direction of scanning. The size and shape of these objects make us thinking that the circular features might be skyrmions, either isolated or aggregated ones. Especially in Figure 3.8(f), dots arranged in straight lines can be seen, as suggested by the contouring stepped line. This would corroborate the hypothesis of the presence of aggregated skyrmions, mixed to the tilted conical phase. The mixture of tilted conical phase and skyrmions would not be a surprise. In fact, by looking at the phase diagram in Figure 3.3 reported by Chacon et al., at a strong enough applied magnetic field, the tilted conical phase is intersected by the low-temperature skyrmion phase. This should lead to images like Figure 3.8(f), where both phases can be spotted.

Unfortunately, for few reasons, we cannot conclude that these circular features are magnetic skyrmions. In first place, the SOT diameter of 95 nm does not allow to achieve enough spatial resolution to distinguish two separated skyrmions, whose period is about 60 nm. The same experiment should be repeated with a smaller SOT, ideally with a diameter below 50 nm.

Another point is about the field vs temperature protocol followed in the experiment. In many papers [11, 119, 120] it is reported the role played by the cooling rate in the stabilization of the low-temperature skyrmion phase, either in conditions of zero-field cooling or field cooling. The faster the cooling rate, the more energetically stable the skyrmion phase gets. Typical cooling rates are about 6 - 10 K/min, achieved by locally heating the crystal, for instance by using a laser. This fast zero-field cooling could not be achieved in our setup, since the whole UHV chamber was heated up to 65 K and the cooling process down to 2 K was taking approximately few hours. This might compromise the energetic stability of the low-temperature skyrmion phase and its visibility if compared to the tilted conical phase.

Another issue regards the slow nucleation of the low-temperature skyrmion phase, even though it represents a thermodynamic ground state. In fact, as can be seen in Figure 3.3, a two-step process is observed in which the metastable tilted conical state is required as an intermediate state prior to the nucleation of the skyrmion phase. A reported way to increase the volume fraction of the low-temperature skyrmion phase is cycling the magnetic field, about hundred times or more, around a fixed value of B_a [121]. This approach was tempted at few values of B_a in between 100 mT and 120 mT, but no significant changes in the magnetic images were noticed.

The tilted conical phase was detected up to $B_a = 130$ mT. When B_a is increased to 131 mT, the transition from tilted conical phase to field-polarized state occurs, which changes the spin configuration. Instead of rotating around the q vector, tilted away from the magnetic field axis, spins align to the direction of B_a. In our configuration, this means that spins are pointing upwards and the projection of the magnetic stray field along the z direction should lead to a non-zero magnetic background, with no features in it.

Figure 3.9 shows the stray field image scanned at $B_a = 131$ mT, in a window of 1 μm $\times$ 2 μm. The signal range of about 1 mT is given by positive and negative peaks in the right side of the scan, probably corresponding to a surface defect, acting as a pinning point. The rest of the background shows a mild change of the magnetic

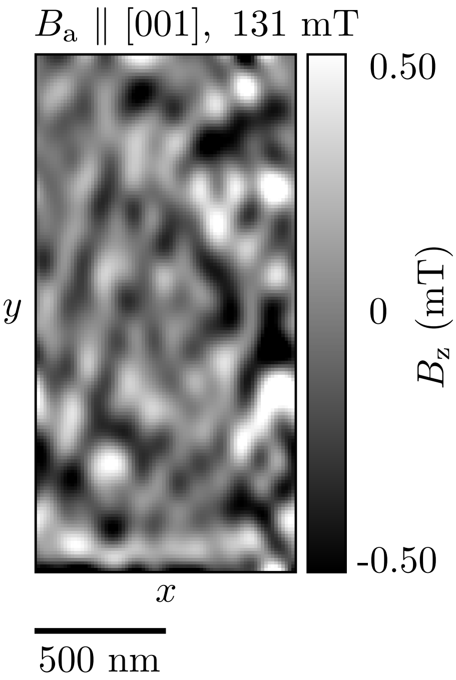

FIGURE 3.9: Real-space, 1 μm × 2 μm wide, magnetic image of the Cu_2OSeO_3 bulk crystal after the transition between tilted conical phase and field polarized phase, at 1.8 K and under ZFC protocol, when an external field is applied in the z direction, parallel to the [001] crystallographic direction. When B_a is increased from 130 mT to 131 mT, the modulation with 143 nm pitch disappears. In this regime, spins align parallel to the field direction and the projection along z gives a DC magnetic background with no specific features.

stray field, as expected for this phase.

3.4 Data analysis: modulation pitch of the tilted conical phase

As shown in Figure 3.7 and Figure 3.8, the tilted conical phase manifests with the appearance of magnetic features, which repeat with a period that is shrinking with the increase of the applied magnetic field. In the following, the measured modulation pitch will be linked to the corresponding spin configuration and the results will be compared to the ones presented in literature. Before discussing the meaning of the modulation pitch, we will focus on how to extract the value of the pitch from the scanning images.

There are two ways to precisely access the information about the period of the magnetic modulation, which can be seen in Figure 3.10.
The first approach is to take a vertical linescan along the y direction, at a fixed x position, of the DC stray magnetic field. Figure 3.10(a) shows the outcome for $B_\mathrm{a} = 88$ mT, where B_z is plotted as a function of y. Over the 3 μm range, about 19 full periods are observed. By using cursors, it is possible to precisely measure the length and then average the pitch over the 19 periods. This is repeated at several x positions, to make the measurement more precise. For the reported case of $B_\mathrm{a} = 88$ mT, the pitch is about 145 nm.

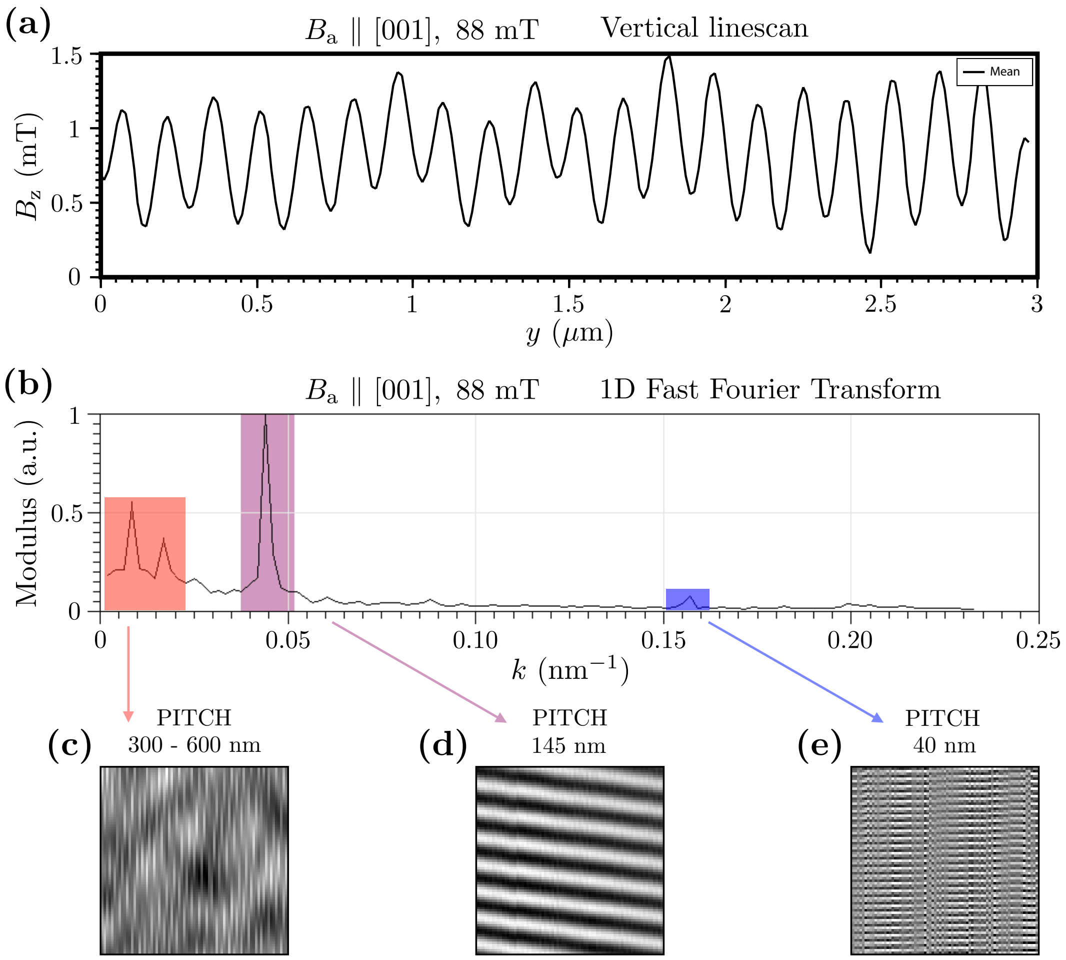

FIGURE 3.10: Determination of the modulation pitch of the tilted conical phase at 88 mT, performed via the commercial software Gwyddion. (a) Vertical linescan, 3 μm long, showing minima and maxima of B_z. Cursors can be used to calculate the period of the modulation, averaged over 19 periods. The result is about 145 nm. (b) Modulus of the 1D Fast Fourier Transform, as a function of the wavelength. The pitch can be calculated as $2\pi/k$. This analysis allows to distinguish contributions to the scan having different frequencies, highlighted in red, violet and blue colors. (c) Drifts in the scan, with a long pitch in the range 300 - 600 nm, due to small changes in experimental conditions. (d) Magnetic modulation of the tilted conical phase, which has the highest FFT modulus and a pitch of 145 nm. (e) Small pitch contribution due to the pixel size.

The second way to determine the modulation period is to perform a 1D FFT, over the same y range chosen for the vertical linescan. The Fourier transform is useful to convert the signal into the frequency domain, where different contributions can be filtered. An example is shown in Figure 3.10(b), where the modulus of the FFT is plotted as function of the wavelength. Three peaks can be distinguished, well spaced in the frequency domain. The real-space period characterizing each peak can be calculated as $2\pi/k$. A small wavelength region is marked in red color and its corresponding signal is reported in Figure 3.10(c). These features have a long pitch of 300 - 600 nm and are given by fluctuations in the scan due to small changes in the experimental conditions. Not particularly relevant for the information encoded in the scan is the contribution from the pixel size (about 13 nm), highlighted in blue color and visible in Figure 3.10(e). The highest and sharpest peak in the FFT is the

one reported in violet color, which is due to a strong magnetic signal with a specific modulation period, as can be seen in Figure 3.10(d). The pitch is found to be 145 nm, which is just a confirmation of what calculated with the first approach.
This process, repeated for every scanned magnetic image where periodic features are observed, allows to know the modulation pitch as function of B_a.

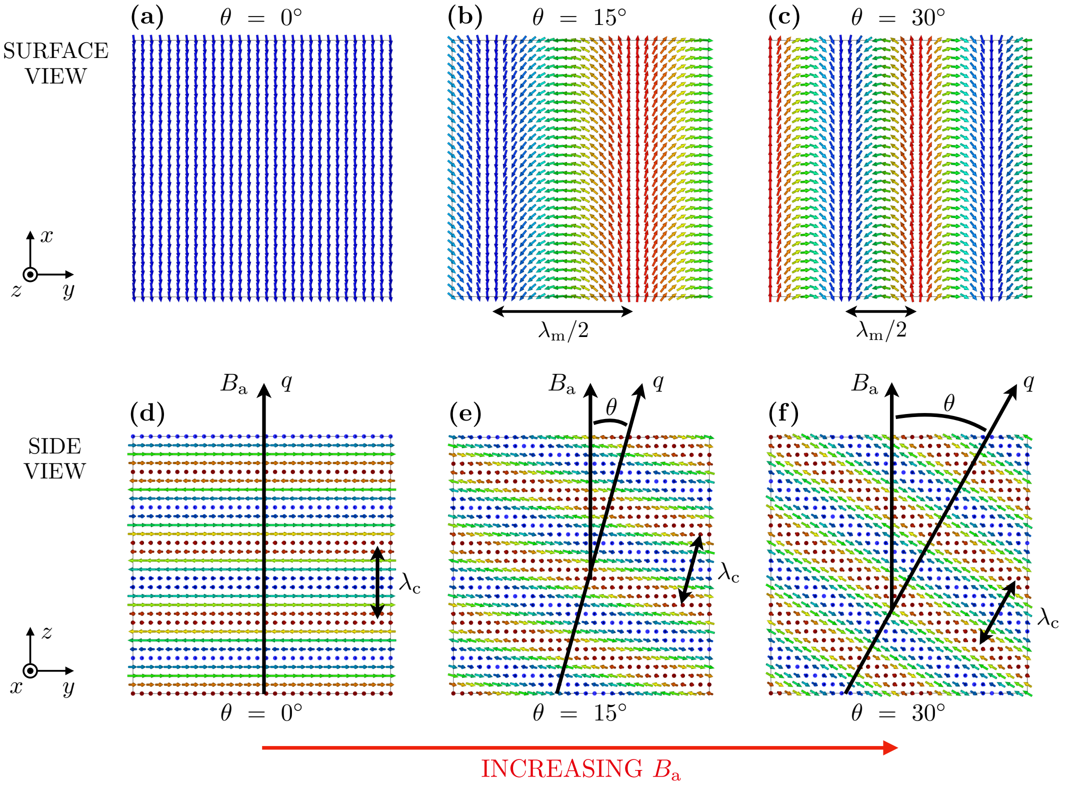

FIGURE 3.11: Spin configuration in the tilted conical phase, simulated via the software Spirit [122], as seen from surface view and side view. When a strong enough magnetic field B_a is applied, spins rotate around the q vector, which is tilted from the field direction by a certain angle θ, increasing with B_a. For matter of simplicity, in the rotation of the spins around the q vector, the tilting of the spins towards the field direction is omitted. The tilted conical modulation has a pitch $\lambda_c \simeq 66$ nm, which is the period after which spins recover the original orientation. This is visible in (d)-(f). The top row (a)-(c) shows the projection of the spin planes on the crystal surface, which defines the signal measured by the SOT. The projection gives rise to a tilted conical modulation with a new pitch λ_m. By knowing λ_c and λ_m, the angle θ is determined by Eq. 3.4.

At this point, we are interested in explaining what the measured period of the magnetic modulations in the tilted conical phase means in terms of spin configuration inside the crystal. The description is supported by Figure 3.11, where the spin arrangement is simulated by the magnetic simulation framework Spirit [122]. For matter of simplicity and ease to distinguish the spin directions, the simulations do not take into account the tilting of the spins towards the magnetic field direction, happening in the conical phase, but only the tilting of the q vector by a certain angle θ with respect to the magnetic field axis. Figure 3.11(a)-(c) describe how the spins dispose at three different angles, as seen from the top, which corresponds to the projection along z measured by the SOT. Contrary, Figure 3.11(d)-(f) show the same

phase as looking from the side, revealing the true spin configuration inside the crystal.
Let start by considering the situation at $\theta = 0°$, depicted in Figure 3.11(a),(d), which can be considered as the beginning of the tilted conical phase. The fact that $\theta = 0°$ means that spins are rotating forming cones around the q vector, which is aligned with the B_a direction. Spins recover their original orientation after a period λ_c, which is known from literature to be about 66 nm. In this situation where no tilting of the q vector occurs, the projection of the spin planes on the crystal surface transduces into a lack of magnetic modulations in the x-y plane.
An important change is observed when B_a is increased, in such a way the q vector gets tilted away from the z direction by an angle $\theta \neq 0°$. This is shown in Figure 3.11(b),(e), where we consider $\theta = 15°$. The spins keep rotating around q with a periodicity that can be approximated as constant. In reality, λ_c slightly increases with the magnetic field (from 64 nm to 68 nm), as reported by the SANS measurements by Chacon et al. [11], however the change is so mild that we assume a constant $\lambda_\mathrm{c} = 66$ nm. When the spin planes get projected on the crystal surface, magnetic modulations appear, with a period λ_m, which is the one found in the scanning images. In Figure 3.11(c),(f), the tilting of the q vector is further emphasized, which leads to a smaller modulation pitch if looking from the top.
By knowing λ_c and by measuring λ_m from the scanning images, simple trigonometry can be used to access the value of θ:

$$\sin\theta = \frac{\lambda_\mathrm{c}}{\lambda_\mathrm{m}} \tag{3.4}$$

Figure 3.12 shows a comparison between the θ from our experiment (Figure 3.12(b)), calculated by using Eq. 3.4, and the reference data measured by SANS (Figure 3.12(a)). Here the relevant data are the dark grey squares, measured under condition of ZFC. In the calculation of *theta*, a relative error of about ±2% is estimated mainly due to the approximation of constant λ_c and in second place due a small imprecision in determining λ_m. The error is not shown in the plot, because it is smaller than the dot size.
Starting from zero field up to 58 mT, no periodic magnetic features are observed. This corresponds to a infinite modulation pitch, therefore $\theta = 0$. This makes sense, because in the helical phase no tilting of the q vector with respect to the field takes place.
The entrance in the tilted conical phase, at $B_\mathrm{a} = 60$ mT, is characterized by magnetic modulations with a long period of 1.6 - 2 μm, corresponding to small angles about 2°. This mild tilting remains constant up to $B_\mathrm{a} = 70$ mT. When $B_\mathrm{a} = 73$ mT the period changes from 1.6 μm to 190 nm, meaning that θ transitions from 2° to 20°. More data points in this 3 mT range would be needed to investigate the tilting of the q vector and understand how sharp the increase is. Unfortunately, due to the hysteresis in the magnetic behavior, it was not possible to lower B_a and take more data points to fill the gap in between 70 mT and 73 mT. The only possibility to deeply study the transition from helical to tilted conical phase would have been heating the crystal above 65 K and performing a new ZFC study.

With the raising of the magnetic field, the angle θ progressively increases to about 27°, as the modulation pitch is reduced from 190 nm down to 143 nm. Above 100 mT, in order to look for skyrmion nucleation, magnetic scans are repeated at intervals of 1 mT. For clarity, in the graph in Figure 3.12(b) only few points are reported. No further increase of the angle is noticed, until the spins transition to the field-polarized

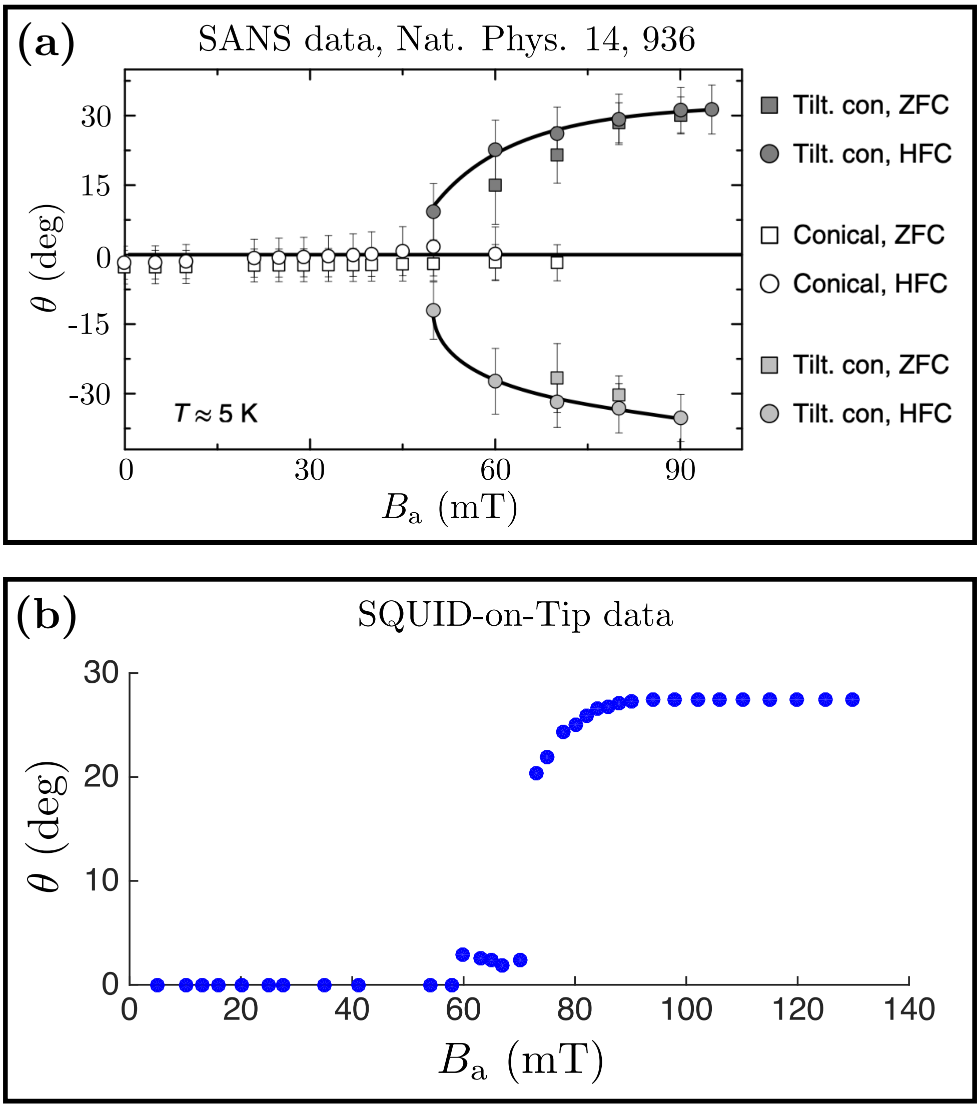

FIGURE 3.12: Dependence of the angle θ of the tilted conical modulation with respect to the B_a axis, as function of B_a, which is not corrected by the demagnetization field. (a) SANS measurements from [11]. The relevant data for our experiment are the ones about tilted conical phase under ZFC protocol. (b) θ plotted as function of B_a. The values of θ are calculated using Eq. 3.4. $\lambda_c = 66$ nm, from [11], is assumed to be constant with B_a, while λ_m is measured as discussed in Figure 3.11. A relative error of $\pm 2\%$ is estimated, due to the approximation of constant λ_c and the imprecision in determining λ_m from the data analysis. The error is smaller than the dot size. A good agreement can be noticed with the data reported by Chacon via SANS.

state and the periodic features disappear.

At this point, it is interesting to compare our data to the ones in Figure 3.12(a), reminding that our field is not corrected due to the demagnetization field. A good agreement can be found between the two set of data, especially for what concerns the transition from no tilting to $\theta = 20°$ and the maximum value of θ around 30 degrees.

Summary and Outlook

SOT sensors are one of the most powerful tools to perform magnetic scanning experiments at the nanoscale. The excellent SOT magnetic and thermal responses are associated to a small superconducting ring diameter, which allows for a fine, tunable spatial resolution. These qualities take on significant importance, since the SQUID ring is located at the apex of a capillary that can be approached few tens of nanometers far from the surface of the sample under investigation. This leads to the possibility of locally studying 2D maps of DC and AC stray magnetic fields, at cryogenic temperature and under external magnetic field up to few T, with low invasiveness.
In this thesis work, we have shown multiple techniques to coat the quartz capillaries with different superconducting materials, which results in a tunability of the main SOT properties, such as critical field, temperature and magnetic response, over a broad range. An example of the high potential of SOT magnetometry was presented, where different magnetic phases of a bulk chiral crystal were investigated in real-space and with a spatial resolution below 100 nm.
In the following the results concerning the sensor fabrication, the material properties and the magnetic imaging study of Cu_2OSeO_3 will be summarized. The conclusion will be an outlook about general comments on the SOT technique, future improvements and new possible samples to investigate.

Summary of SOT sensors

In Chapter 2, SOT sensors made of three materials, each of them deposited via a different deposition technique, were presented.
The original choice is to fabricate SOT with thermally evaporated Pb, due to the offered extremely low magnetic flux noise (about 50 $n\Phi_0/\sqrt{Hz}$ at 4.2 K [54]). The Pb SOT fabrication relies on the material softness in order to coat the pipette curved surface and achieve a high quality thin superconducting film. Due to the percolation length and high mobility at room temperature, cooling the pipette to cryogenic temperature is required. The necessity to cool the pipette and the influence that this process has on the Pb film quality makes the Pb SOT fabrication not straightforward. Another complication is the fast and strong oxidation of Pb films when exposed to oxygen. This limits the amount of time (approx 30 minutes) that the SOT can survive in air before the superconducting properties degrade and suddenly quench. This property influences the way we need to handle such sensors while mounting them in the microscope probe and the speed that is required to complete all the preparation steps, with no space for mistakes. More complications are observed when shrinking the apex diameter below 100 nm or, even worse, close to 50 nm.
Our experience with Pb limits it for the experiments where a diameter bigger than 100 nm, ideally close to 200 nm, is required. In fact, bigger sensors turn out to be more robust and with a higher probability to survive the cool down process. The Pb fragility is compensated by its excellent properties: working up to 7 K, up to an applied magnetic field of 2 T at 300 mK [8] and achieving a magnetic flux noise of

few tens of $n\Phi_0/\sqrt{Hz}$ [8, 54].

The development of SOT made of MoGe is motivated by the aim to achieve a sensor that can work in the mK temperature regime and well performs in presence of high applied magnetic field. The MoGe deposition combines two elements that are the key for the incoming years of SOT fabrication: quartz capillaries with four symmetric grooves, which help in maintaining a superconducting gap when the apex diameter gets shrinked to its limits, and magnetron sputtering technique, which can deposit elemental materials as well as compounds and is well known to provide high quality, thin films.
A way of combining magnetron sputtering and ballistic-flow deposition from point-like source is presented, based on establishing a differential pressure between the zone of the metal target and the quartz capillary to be coated and on using a narrow slit to collimate the plasma. This strategy allows to achieve a quasi-ballistic deposition technique and fabricate SOT with diameter close to 50 nm.
MoGe SOTs work from the mK temperature regime up to 5 K and were tested up to a applied magnetic field of 3 T at 450 mK. The smallest tested SOTs have a diameter of 60 - 70 nm, providing a high spatial resolution. The most appreciated characteristic is without any doubt the reliability of the fabrication process, showing a yield rate of 80% or more, and the robustness of SOTs in handling thermal cycles.
On the other hand, the measured magnetic response can not be compared to the one achieved by Pb SOTs. A typical MoGe SOT shows a magnetic flux noise of 5 $\mu\Phi_0/\sqrt{Hz}$ at 4.2 K, which is two orders of magnitude worse than the value reported for Pb SOTs. However, for many interesting samples, such as the investigated Cu_2OSeO_3, the magnetic response of MoGe SOTs is high enough.

Nb SOT are meant to be a compromise between the qualities of Pb and MoGe, combining a high magnetic response to a broad temperature and magnetic field working range. The Nb deposition makes use of the magnetron sputtering technique introduced for MoGe, with the major difference of the removal of the differential pressure setup. The traditional sputtering deposition provides higher quality thin films, and at the same time the presence of a superconducting gap between the electrodes is guaranteed by the four grooves. To avoid contamination of the bottom and top Nb layers from quartz and oxidation, the Nb film is protected by few nanometers of Ti. This leads to a thin Ti/Nb/Ti film with a critical temperature comparable to the one reported for bulk material.
A full set of data for a ∅180 nm Nb SOT was reported, showing at 4.2 K a critical field of almost 1 T and a magnetic field noise below 200 $nT/\sqrt{Hz}$, corresponding to a magnetic flux noise of 2 $\mu\Phi_0/\sqrt{Hz}$. This magnetic response is considerably higher than the one offered by MoGe, but still not close to the limit imposed by Pb.
The step in performance from the MoGe SOT seems to cost in terms of success rate of the fabrication process. Even when protected by the Ti layers, the Nb film is very reactive to small changes in the deposited amount, in such a way more effort is required to get a working SOT if compared to MoGe. Margins of improvement can still be achieved by tuning parameters in the sputtering recipe, such as power, plasma density and thickness of the protection layers.
The fabrication of SOT via direct sputtering deposition on grooved capillaries remains a remarkable result, since it paves to way for achieving high quality thin films from an entire class of elemental metals and material compounds that can expand the range of tunability of the SOT properties.

Summary of Cu_2OSeO_3 investigation

Chapter 3 has focused on a SPM experiment on the chiral magnet Cu_2OSeO_3, performed by using a sub-100 nm diameter MoGe SOT. The interest on this material by the scientific community in the last ten years is motivated by the fact that Cu_2OSeO_3 is the first insulating material where a magnetic skyrmion lattice was found, with a lattice constant of 60 - 70 nm. Since the material is an insulator, skyrmions can be manipulated by an external magnetic field, with a negligible energy dissipation. This low-cost manipulation is a quite promising ingredient for technological applications in the fields of communication and information storage.

Our research on this material had the target of investigating the behavior of a bulk crystal of Cu_2OSeO_3, with the top surface polished for SPM experiments. Following the references available in literature [11], the study was performed at cryogenic temperature, in presence of an applied magnetic field, parallel to the [001] crystallographic direction, after zero-field cooling the crystal. The aim was to provide real-space magnetic imaging of different phases, by measuring the projection of the DC stray magnetic field along the z axis. Excluding possible contributions from surface defects, this stray field reveals important informations about the spin configuration inside the bulk crystal. The SOT technique has the great advantage of shedding light on the magnetic configuration of the Cu_2OSeO_3, with a spatial resolution as good as 100 nm, and with weak perturbation of the sample surface.

The experimental investigation at 1.8 K showed clear traces of three distinct magnetic phases. At low applied magnetic field, the helical phase corresponds to spins forming helices around the q vectors parallel to [100], [010], [001] crystallographic directions. The magnetic scans revealed a magnetic background due to the helices rotating around the in-plane q vectors, without any particular feature. A similar outcome was observed at high applied magnetic field, when the spin configuration transitions from tilted conical phase to field-polarized state. In this case, spins align parallel to the magnetic field direction, along the z axis. This produces a non-zero DC stray field, with no features in it.

The most interesting result concerned the tilted conical phase. In this state, spins rotate around the q vector and bend towards the field direction, forming a cone. Moreover the q vector no longer remains parallel to the field direction, but it bends by an angle that ranges from zero to almost 30°. This configuration leads to the appearance of magnetic features, modulated by a period that changes with the applied magnetic field. The transition from helical phase to tilted conical phase at 61 mT was observed, with the detection of magnetic textures with a period of 1.6 - 2 μm, aligned according to the shape anisotropy direction of the crystal. Such a period corresponds to the q vector tilting from the field axis by about 2°. A second transition takes place at 73 mT, when the period of the magnetic modulations reduces to 190 nm, equivalent to the q vector tilting from the field axis by about 20°. The magnetic scans showed the progressive reduction of the modulation pitch, until it reached a minimum value of 143 nm. A detailed data analysis on the observed pitch of the tilted conical modulation was reported, explaining the physical meaning in terms of spin configuration inside the crystal and comparing the tilting angle of the q vector to reference values from the literature.

At high applied magnetic field, the magnetic modulations of the tilted conical phase are accompanied by circular features, with dimensions about 60 - 70 nm, especially visible in Figure 3.8(f), where dots show up as single objects, or disposed in lines. This could correspond to a mixed state, with the tilted conical phase and the low-temperature skyrmion phase. The idea would be supported by the zero-field cooling phase diagram from [11] and the estimated dimensions of these dots would be in good agreement with the theoretical predictions and the SANS measurements from [11]. However, due to lack of spatial resolution, our measurement is not conclusive and the confirmation of the detection of a mixed phase requires a new experimental investigation with a smaller SOT, ideally with a diameter below 50 nm.

Outlook

Here an outlook of possible improvements regarding sensor fabrication, new materials to be deposited via magnetron sputtering, microscope probe and future samples to investigate will be discussed.

If comparing the three deposition techniques described in Chap. 2, the most impressive one is the direct magnetron sputtering deposition on quartz four-grooves capillaries. Without the need of a collimation chamber, the shape of the capillary prevents by itself electrical shorts between the superconducting electrodes. At the same time, magnetron sputtering deposition guarantees high quality thin metal films. This technique certainly represents the future of our SOT fabrication, because it is compatible with a wide range of materials.

Two major upgrades, which could speed up the fabrication process and improve the SOT quality, are scheduled. In first place, the installation of a UHV gate valve, which is supposed to help reaching a lower base pressure. A second important upgrade is the installation of a load-lock chamber. This consists of an additional, small chamber where the SOT holder is mounted and pumped to high vacuum condition, before being transfered to the main sputtering chamber. The advantage is that no venting, and consequently pumping and baking of the main chamber is needed anymore, because the UHV condition is always maintained. This implies that the SOT fabrication time could be reduced by half or more, increasing time efficiency.

The sputtered materials introduced in this thesis work were MoGe and Nb. In the next future, we expect to try direct sputtering deposition of MoGe film, without using the collimation chamber. As described for Nb, the MoGe thin film could be protected by Ti layers, in order to avoid degradation of the superconducting film due to quartz impurities and oxidation. It will be interesting to compare the superconducting properties of such a MoGe SOT with the results previously obtained with the collimation chamber.

To the aim of increasing the range of tunability of the SOT properties, other materials could be tested, such as:

- Al: it was the first material to be reported in SOT fabrication [53]. Due to its critical temperature of 1.2 K (for bulk), it is suitable to work in the mK temperature regime. However, its magnetic response is not as good as the one reported for other materials.
- MoRe: it shares some properties already highlighted for MoGe, being suitable for applications at high applied magnetic field. If compared to MoGe, the reported critical field is even higher (about 5 T at 4.2 K) [9].
- Sn: it is suitable to work in the mK temperature regime. A Sn SOT was reported, with diameter 41 nm and a critical field of about 1 T [8].

- In: it shares the same characteristics as Sn, but the critical field is about 2 T and a SOT with 39 nm diameter was reported to achieve a magnetic flux sensitivity of 42 $n\Phi_0/\sqrt{\mathrm{Hz}}$ [8].

The SOT dedicated to experiments at mK temperatures require to be tested below 4.2 K. To this aim, a 1K pot probe is currently under development. Its design is similar to the current probe used to characterize the SOT at 4.2 K, with an addition of a needle valve to regulate the pressure of ^{4}He pumped from the dewar. This probe would allow to reach a base temperature close to 1 K and get knowledge of the SOT properties at a temperature close to the one at which the future experiment is carried.
Another point to consider is that materials such as In and Sn are soft, have a low melting point (about 430 K for In and 500 K for Sn) and a low thermal conductivity. This complicates the sputtering deposition, because particular attention to thermal gradients when ramping up and down the DC power is required. Additional cooling of the target via a copper plate or via bonding is needed to avoid the melting. More frequently, In and Sn are evaporated in the same way pictured for Pb.

A weak point of the SOT technique is that, when performing DC magnetometry, the minimum detectable magnetic flux is roughly ten times worse than the corresponding magnetic flux in the white noise limit. This is because at a frequency of few Hz spectral noise is dominated by the $1/f$ contribution. This makes the measurement of small DC stray fields more challenging.
A possibility to improve the minimum detectable DC magnetic flux is coming from few reference works [3, 5, 123]. As described in Sec. 2.6.1, we can couple a qPlus tuning fork close to the apex of a SOT. A first benefit regards the approach to the surface under investigation, which can be done mechanically by monitoring the frequency shift from the resonance frequency of the coupled qPlus. The same frequency shift can be used to keep the SOT apex at a fixed distance from the surface. A second benefit, not exploited yet, is that the SOT apex vibrates parallel to the sample surface with an amplitude x_{ac}, tunable up to tens of nanometers, and at a frequency of about 33 KHz. By using a lock-in amplifier, it is possible to measure the magnetic signal demodulated at the SOT oscillation frequency, corresponding to $B_{\mathrm{ac}}(x,y) = x_{\mathrm{ac}}\partial B_{\mathrm{z}}(x,y)/\partial x$, where B_{z} is the static stray magnetic field. By choosing an oscillation amplitude smaller than both the SOT diameter and the sensor to surface distance, the $1/f$ noise is avoided, with an improvement of ultimate detectable field and spatial resolution [24]. This could be interesting for samples such as the Cu_2OSeO_3 crystal investigated in this thesis work. Another advantage is that we could further shrink the SOT diameter, approaching the 50 nm limit, without the risk of not having enough magnetic sensitivity to perform the experiment.

The conclusion is an outlook of possible applications of our probe in the near future, which are considered of high impact by the scientific community.
Belonging to the class of oxo-selenite compounds, $VOSe_2O_5$ (vanadium oxo-selenite) is a tetragonal polar magnet, hosting a Néel-type skyrmion lattice. The interesting magnetic phases in the phase diagram are confined in a narrow pocket between 4 K and just above 7 K, from zero magnetic field up to about 5 - 10 mT. Recent magnetization and SANS measurements have experimentally identified a cycloidal spin state at zero field and a Néel-type triangular skyrmion lattice phase under applied magnetic field along the polar axis [124]. Adjacent to these two phases, another incommensurate spin texture order was observed, with in-plane modulation under

applied magnetic field along the polar axis. This magnetic phase was interpreted as a square skyrmion lattice state, induced by interplay of the tetragonal crystal anisotropy and the effect of thermally varying uniaxial anisotropy. No real-space observation of these magnetic phases is reported in literature, so that a SOT investigation of a bulk crystal of $VOSe_2O_5$ could provide novel insights into the formation and stabilization of skyrmion states in this polar magnet. Magnetic features have a size bigger than 100 nm, which is not imposing a tight requirement on the scanning spatial resolution. On the other hand, the experiment has to be performed up to a temperature above 7 K. This can be achieved by locally heating the sample, while keeping the SOT in UHV condition at a temperature between 400 mK and 4 K, at which the magnetic response is maximized.

Another promising field is the one of 2D layered materials. There is a growing class of layered materials with unique magnetic properties, which constitutes an ideal platform to investigate magnetism and spintronics device concepts in the 2D limit [125]. Since these materials are atomically thin, their magnetic states can be controlled by external perturbations, such as electric field and free carrier doping. The study of magnetism in a true 2D limit is a key step towards the integration of 2D magnetic layers into device structures. Among 2D materials, great attention was captured by the class of transition metal dichalcogenides, and in special way by $PtSe_2$ [126, 127]. $PtSe_2$ has a particular, thickness-dependent, electronic structure: multilayer films exhibit metallic behavior, while mono- and bilayers show a transition from metal to semiconductor. Furthermore, defect engineering can lead to tune the electronic properties. Few advantages are offered by $PtSe_2$ for immediate research. From a practical prospective, the material is stable in air without requiring to be handled inside a glove box or to be encapsulated [128]. This simplifies the fabrication and allows to perform the exfoliation process in a standard cleanroom environment. Furthermore, $PtSe_2$ can be easily grown with various scalable methods and is isolated from its substrate, in such a way it can be transfered to any other arbitrary substrate [129]. A SOT investigation could shed light on the interplay between disorder and magnetism at atomic-scale thickness, as a step towards the implementation of 2D semiconducting magnet devices.

Bibliography

[1] J.R. Kirtley et al. "Scanning SQUID susceptometers with sub-micron spatial resolution". In: *Rev. Sci. Instrum.* 87.9 (2016), p. 093702. DOI: `10.1063/1.4961982` (cit. on pp. viii, 6, 17, 18).

[2] A. Finkler, Y. Segev, Y. Myasoedov, M.L. Rappaport, L. Ne'eman, D. Vasyukov, E. Zeldov, M.E. Huber, J. Martin, and A. Yacoby. "Self-Aligned Nanoscale SQUID on a Tip". In: *Nano Lett.* 10.3 (Mar. 2010), pp. 1046–1049 (cit. on pp. viii, 6, 18, 19).

[3] D. Halbertal et al. "Nanoscale thermal imaging of dissipation in quantum systems". In: *Nature* 539.7629 (2016), pp. 407–410 (cit. on pp. viii, 19, 79).

[4] L. Embon et al. "Imaging of super-fast dynamics and flow instabilities of superconducting vortices". In: *Nat. Comm.* 8.1 (2017), p. 85 (cit. on pp. viii, 19).

[5] D. Halbertal et al. "Imaging resonant dissipation from individual atomic defects in graphene". In: *Science* 358.6368 (2017), pp. 1303–1306. DOI: `10.1126/science.aan0877` (cit. on pp. viii, 19, 50, 79).

[6] A. Uri et al. "Mapping the twist-angle disorder and Landau levels in magic-angle graphene". In: *Nature* 581.7806 (2020), pp. 47–52 (cit. on pp. viii, 19).

[7] A. Aharon-Steinberg, A. Marguerite, D.J. Perello, K. Bagani, T. Holder, Y. Myasoedov, L. S. Levitov, A. K. Geim, and E. Zeldov. "Long-range nontopological edge currents in charge-neutral graphene". In: *Nature* 593.7860 (2021), pp. 528–534 (cit. on pp. viii, 19).

[8] Y. Anahory et al. "SQUID-on-tip with single-electron spin sensitivity for high-field and ultra-low temperature nanomagnetic imaging". In: *Nanoscale* 12 (5 2020), pp. 3174–3182. DOI: `10.1039/C9NR08578E` (cit. on pp. viii, 49, 75, 76, 78, 79).

[9] K. Bagani, J. Sarkar, A. Uri, M.L. Rappaport, M.E. Huber, E. Zeldov, and Y. Myasoedov. "Sputtered Mo66Re34 SQUID-on-Tip for High-Field Magnetic and Thermal Nanoimaging". In: *Phys. Rev. Appl.* 12 (4 2019), p. 044062. DOI: `10.1103/PhysRevApplied.12.044062` (cit. on pp. viii, 6, 33, 78).

[10] S. Seki, X.Z. Yu, S. Ishiwata, and Y. Tokura. "Observation of Skyrmions in a Multiferroic Material". In: *Science* 336.6078 (2012), pp. 198–201. DOI: `10.1126/science.1214143` (cit. on pp. ix, 57, 58).

[11] A. Chacon, L. Heinen, M. Halder, A. Bauer, W. Simeth, S. Mühlbauer, H. Berger, M. Garst, A. Rosch, and C. Pfleiderer. "Observation of two independent skyrmion phases in a chiral magnetic material". In: *Nature Phys.* 14.9 (2018), pp. 936–941 (cit. on pp. ix, x, 58, 62, 68, 72, 73, 77, 78).

[12] P. Li-cong, Z. Ying, Z. Shu-lan, He Min, C. Jian-wang, W. Shou-guo, W. Hong-xiang, Li Jian-qi, Z. Tong-yun, and S. Bao-gen. "Lorentz transmission electron microscopy studies on topological magnetic domains". In: *Chinese Physics B* 27.6 (2018), p. 066802. DOI: `10.1088/1674-1056/27/6/066802` (cit. on p. ix).

[13] C.L. Degen. “Scanning magnetic field microscope with a diamond single-spin sensor”. In: *Appl. Phys. Lett.* 92.24 (2008), p. 243111. DOI: `10.1063/1.2943282` (cit. on pp. x, 4).

[14] G. Balasubramanian et al. “Nanoscale imaging magnetometry with diamond spins under ambient conditions”. In: *Nature* 455.7213 (2008), pp. 648–651 (cit. on pp. x, 4).

[15] P. Maletinsky, S. Hong, M.S. Grinolds, B. Hausmann, M.D. Lukin, R.L. Walsworth, M. Loncar, and A. Yacoby. “A robust scanning diamond sensor for nanoscale imaging with single nitrogen-vacancy centres”. In: *Nat. Nanotech.* 7.5 (2012), pp. 320–324 (cit. on pp. x, 4).

[16] D. Bonnell. *Scanning Probe Microscopy and Spectroscopy: Theory, Technique, and Applications, Second Edition*. Wiley-VCH, 2001 (cit. on p. 1).

[17] G. Binnig and H. Rohrer. “Scanning tunneling microscopy”. In: *Helv. Phys. Acta* 55 (1982), pp. 726–735 (cit. on p. 1).

[18] E. Meyer, R. Bennewitz, and H.J. Hug. *Scanning Probe Microscopy, The Lab on a Tip, Second Edition*. Springer Nature Switzerland AG, 2021 (cit. on p. 2).

[19] S.M. Salapaka and M.V. Salapaka. “Scanning Probe Microscopy”. In: *IEEE Control Systems Magazine* 28.2 (2008), pp. 65–83. DOI: `10.1109/MCS.2007.914688` (cit. on p. 2).

[20] G. Binnig, C.F. Quate, and Ch. Gerber. “Atomic Force Microscope”. In: *Phys. Rev. Lett.* 56 (9 1986), pp. 930–933. DOI: `10.1103/PhysRevLett.56.930` (cit. on p. 2).

[21] Y. Martin and H.K. Wickramasinghe. “Magnetic imaging by “force microscopy” with 1000 Å resolution”. In: *Applied Physics Letters* 50.20 (1987), pp. 1455–1457. DOI: `10.1063/1.97800` (cit. on pp. 2, 3).

[22] H.G. Hansma and J.H. Hoh. “Biomolecular imaging with the atomic force microscope”. In: *Annu. Rev. Biophys. Biomol. Struct.* 23 (1994), pp. 115–139. DOI: `10.1146/annurev.bb.23.060194.000555` (cit. on p. 2).

[23] J. Kirtley. “Fundamental studies of superconductors using scanning magnetic imaging”. In: *Rep. Prog. Phys.* 73 (Aug. 2010). DOI: `10.1088/0034-4885/73/12/126501` (cit. on pp. 3, 5, 6).

[24] E. Marchiori, L. Ceccarelli, N. Rossi, L. Lorenzelli, C.L. Degen, and M. Poggio. “Nanoscale magnetic field imaging for 2D materials”. In: *Nat. Rev. Phys.* 4.1 (2022), pp. 49–60 (cit. on pp. 3, 6, 79).

[25] J.J. Sáenz, N. García, P. Grütter, E. Meyer, H. Heinzelmann, R. Wiesendanger, L. Rosenthaler, H.R. Hidber, and H.J. Güntherodt. “Observation of magnetic forces by the atomic force microscope”. In: *J. Appl. Phys.* 62.10 (1987), pp. 4293–4295. DOI: `10.1063/1.339105` (cit. on p. 3).

[26] L.M. Belova, O. Hellwig, E. Dobisz, and E. Dan Dahlberg. “Rapid preparation of electron beam induced deposition Co magnetic force microscopy tips with 10 nm spatial resolution”. In: *Rev. of Sci. Instrum.* 83.9 (2012), p. 093711. DOI: `10.1063/1.4752225` (cit. on p. 3).

[27] A. Moser, M. Xiao, P. Kappenberger, K. Takano, W. Weresin, Y. Ikeda, H. Do, and H. Hug. “High-resolution magnetic force microscopy study of high-density transitions in perpendicular recording media”. In: *J. Magn. Magn. Mat.* 287 (Feb. 2005), pp. 298–302. DOI: `10.1016/j.jmmm.2004.10.048` (cit. on pp. 3, 4).

[28] A. Siria and A. Niguès. "Electron beam detection of a Nanotube Scanning Force Microscope". In: *Sci. Rep.* 7.1 (2017), p. 11595 (cit. on p. 3).

[29] L.M. de Lépinay, B. Pigeau, B. Besga, P. Vincent, P. Poncharal, and O. Arcizet. "A universal and ultrasensitive vectorial nanomechanical sensor for imaging 2D force fields". In: *Nat. Nanotechnol.* 12.2 (2017), pp. 156–162 (cit. on p. 3).

[30] N. Rossi, F.R. Braakman, D. Cadeddu, D. Vasyukov, G. Tütüncüoglu, A. Fontcuberta i Morral, and M. Poggio. "Vectorial scanning force microscopy using a nanowire sensor". In: *Nat. Nanotechnol.* 12.2 (2017), pp. 150–155 (cit. on p. 3).

[31] J.M. Nichol, E.R. Hemesath, L.J. Lauhon, and R. Budakian. "Nanomechanical detection of nuclear magnetic resonance using a silicon nanowire oscillator". In: *Phys. Rev. B* 85 (5 2012), p. 054414. DOI: `10.1103/PhysRevB.85.054414` (cit. on p. 3).

[32] F. Fabre, A. Finco, A. Purbawati, A. Hadj-Azzem, N. Rougemaille, J. Coraux, I. Philip, and V. Jacques. "Characterization of room-temperature in-plane magnetization in thin flakes of $CrTe_2$ with a single-spin magnetometer". In: *Phys. Rev. Materials* 5 (3 2021), p. 034008. DOI: `10.1103/PhysRevMaterials.5.034008` (cit. on p. 3).

[33] T. Yamaoka, H. Tsujikawa, S. Hasumura, K. Andou, M. Shigeno, A. Ito, and H. Kawamura. "Vacuum Magnetic Force Microscopy at High Temperatures: Observation of Permanent Magnets". In: *Microsc. Today* 22.6 (2014), 12–17. DOI: `10.1017/S1551929514001163` (cit. on p. 4).

[34] P.J.A. van Schendel, H.J. Hug, B. Stiefel, S. Martin, and H.-J. Güntherodt. "A method for the calibration of magnetic force microscopy tips". In: *J. Appl. Phys.* 88.1 (2000), pp. 435–445. DOI: `10.1063/1.373678` (cit. on p. 4).

[35] H. Mattiat, N. Rossi, B. Gross, J. Pablo-Navarro, C. Magén, R. Badea, J. Berezovsky, J. M. De Teresa, and M. Poggio. "Nanowire Magnetic Force Sensors Fabricated by Focused-Electron-Beam-Induced Deposition". In: *Phys. Rev. Applied* 13 (4 2020), p. 044043. DOI: `10.1103/PhysRevApplied.13.044043` (cit. on p. 4).

[36] R. Schirhagl, K. Chang, M. Loretz, and C.L. Degen. "Nitrogen-Vacancy Centers in Diamond: Nanoscale Sensors for Physics and Biology". In: *Annual Review of Physical Chemistry* 65.1 (2014), pp. 83–105. DOI: `10.1146/annurev-physchem-040513-103659` (cit. on p. 4).

[37] B.K. Ofori-Okai, S. Pezzagna, K. Chang, M. Loretz, R. Schirhagl, Y. Tao, B.A. Moores, K. Groot-Berning, J. Meijer, and C.L. Degen. "Spin properties of very shallow nitrogen vacancy defects in diamond". In: *Phys. Rev. B* 86 (8 2012), p. 081406. DOI: `10.1103/PhysRevB.86.081406` (cit. on p. 4).

[38] K. Chang, A. Eichler, J. Rhensius, L. Lorenzelli, and C.L. Degen. "Nanoscale Imaging of Current Density with a Single-Spin Magnetometer". In: *Nano Lett.* 17.4 (Apr. 2017), pp. 2367–2373 (cit. on p. 4).

[39] U. Vool et al. "Imaging phonon-mediated hydrodynamic flow in WTe2". In: *Nat. Phys.* 17.11 (2021), pp. 1216–1220 (cit. on p. 4).

[40] M.S. Wörnle, P. Welter, M. Giraldo, T. Lottermoser, M. Fiebig, P. Gambardella, and C.L. Degen. "Coexistence of Bloch and Néel walls in a collinear antiferromagnet". In: *Phys. Rev. B* 103 (9 2021), p. 094426. DOI: `10.1103/PhysRevB.103.094426` (cit. on p. 4).

[41] R.J. Epstein, F.M. Mendoza, Y.K. Kato, and D.D. Awschalom. "Anisotropic interactions of a single spin and dark-spin spectroscopy in diamond". In: *Nat. Phys.* 1.2 (2005), pp. 94–98 (cit. on p. 4).

[42] D. Budker and M. Romalis. "Optical magnetometry". In: *Nat. Phys.* 3.4 (2007), pp. 227–234. DOI: `10.1038/nphys566` (cit. on p. 4).

[43] S. Sangtawesin et al. "Origins of Diamond Surface Noise Probed by Correlating Single-Spin Measurements with Surface Spectroscopy". In: *Phys. Rev. X* 9 (3 2019), p. 031052. DOI: `10.1103/PhysRevX.9.031052` (cit. on p. 5).

[44] A.M. Chang, H.D. Hallen, L. Harriott, H.F. Hess, H.L. Kao, J. Kwo, R.E. Miller, R. Wolfe, J. van der Ziel, and T.Y. Chang. "Scanning Hall probe microscopy". In: *Appl. Phys. Lett.* 61.16 (1992), pp. 1974–1976. DOI: `10.1063/1.108334` (cit. on p. 5).

[45] A. Oral, S.J. Bending, and M. Henini. "Real time scanning Hall probe microscopy". In: *Appl. Phys. Lett.* 69.9 (1996), pp. 1324–1326. DOI: `10.1063/1.117582` (cit. on p. 5).

[46] R.B. Dinner, M.R. Beasley, and K.A. Moler. "Cryogenic scanning Hall-probe microscope with centimeter scan range and submicron resolution". In: *Rev. Sci. Inst.* 76.10 (2005), p. 103702. DOI: `10.1063/1.2072438` (cit. on p. 5).

[47] A.N. Grigorenko, S.J. Bending, J.K. Gregory, and R.G. Humphreys. "Scanning Hall probe microscopy of flux penetration into a superconducting YBa2Cu3O7 thin film strip". In: *Appl. Phys. Lett.* 78.11 (2001), pp. 1586–1588. DOI: `10.1063/1.1352041` (cit. on p. 5).

[48] R.G. van Veen, A.H. Verbruggen, E. van der Drift, S. Radelaar, S. Anders, and H.M. Jaeger. "Micron-sized Hall probes on a Si/SiGe heterostructure as a tool to study vortex dynamics in high-temperature superconducting crystals". In: *Rev. Sci. Inst.* 70.3 (1999), pp. 1767–1770. DOI: `10.1063/1.1149666` (cit. on p. 5).

[49] V. Cambel, G. Karapetrov, P. Eliáš, S. Hasenöhrl, W.K. Kwok, J. Krause, and J. Maňka. "Approaching the pT range with a 2DEG InGaAs/InP Hall sensor at 77 K". In: *Microelect. Eng.* 51-52 (2000), pp. 333–342 (cit. on p. 5).

[50] C.W. Hicks, L. Luan, K.A. Moler, E. Zeldov, and H. Shtrikman. "Noise characteristics of 100nm scale GaAs/AlxGa1-xAs scanning Hall probes". In: *Appl. Phys. Lett.* 90.13 (2007), p. 133512 (cit. on p. 5).

[51] G. Boero, M. Demierre, P.A. Besse, and R. Popovic. "Micro-Hall Devices: Performance, Technologies and Applications". In: *Sens. and Act. A* 106 (Sept. 2003), pp. 314–320. DOI: `10.1016/S0924-4247(03)00192-4` (cit. on p. 5).

[52] M. José Martínez-Pérez and D. Koelle. "NanoSQUIDs: Basics & recent advances". In: *Phys. Sci. Rev.* 2.8 (2017), p. 20175001. DOI: `doi:10.1515/psr-2017-5001` (cit. on p. 6).

[53] A. Finkler, D. Vasyukov, Y. Segev, L. Ne'eman, E.O. Lachman, M.L. Rappaport, Y. Myasoedov, E. Zeldov, and M.E. Huber. "Scanning superconducting quantum interference device on a tip for magnetic imaging of nanoscale phenomena". In: *Rev. Sci. Instrum.* 83.7 (2012), p. 073702. DOI: `10.1063/1.4731656` (cit. on pp. 6, 78).

[54] D. Vasyukov et al. "A scanning superconducting quantum interference device with single electron spin sensitivity". In: *Nat. Nanotech.* 8.9 (2013), pp. 639–644 (cit. on pp. 6, 19, 30, 48, 49, 75, 76).

[55] C.D. Tesche and J. Clarke. “dc SQUID: Noise and optimization”. In: *J. Low Temp. Phys.* 29.3 (1977), pp. 301–331 (cit. on p. 6).

[56] M.W. Mitchell and S. Palacios Alvarez. “Colloquium: Quantum limits to the energy resolution of magnetic field sensors”. In: *Rev. Mod. Phys.* 92 (2 2020), p. 021001. DOI: `10.1103/RevModPhys.92.021001` (cit. on p. 6).

[57] M. Wyss, K. Bagani, D. Jetter, E. Marchiori, A. Vervelaki, B. Gross, J. Ridderbos, S. Gliga, C. Schönenberger, and M. Poggio. *Magnetic, thermal, and topographic imaging with a nanometer-scale SQUID-on-cantilever scanning probe*. 2021 (cit. on p. 6).

[58] O.W. Kennedy, J. Burnett, J.C. Fenton, N.G.N. Constantino, P.A. Warburton, J.J.L. Morton, and E. Dupont-Ferrier. “Tunable Nb Superconducting Resonator Based on a Constriction Nano-SQUID Fabricated with a Ne Focused Ion Beam”. In: *Phys. Rev. Appl.* 11.1 (2019). DOI: `10.1103/physrevapplied.11.014006` (cit. on p. 6).

[59] B. Müller, M. Karrer, F. Limberger, M. Becker, B. Schröppel, C.J. Burkhardt, R. Kleiner, E. Goldobin, and D. Koelle. “Josephson Junctions and SQUIDs Created by Focused Helium-Ion-Beam Irradiation of $YBa_2Cu_3O_7$”. In: *Phys. Rev. Appl.* 11 (4 2019), p. 044082. DOI: `10.1103/PhysRevApplied.11.044082` (cit. on p. 6).

[60] Heike Kamerlingh Onnes. In: *Communications-Leiden* 120b, 122b, 124c (1911) (cit. on p. 7).

[61] J. Bardeen, L. N. Cooper, and J. R. Schrieffer. “Theory of Superconductivity”. In: *Phys. Rev.* 108 (5 1957), pp. 1175–1204. DOI: `10.1103/PhysRev.108.1175` (cit. on p. 7).

[62] G. Grosso and G.P. Parravicini. “Chapter 18 - Superconductivity”. In: *Solid State Physics (Second Edition)*. Ed. by G. Grosso and G.P. Parravicini. Second Edition. Amsterdam: Academic Pres, 2014, pp. 789 –849. DOI: `http://dx.doi.org/10.1016/B978-0-12-385030-0.00018-9` (cit. on pp. 7, 8).

[63] M. Tinkham. *Introduction to Superconductivity*. International series in pure and applied physics. McGraw Hill, 1996 (cit. on pp. 7, 8).

[64] B.D. Josephson. “Possible new effects in superconductive tunnelling”. In: *Phys. Lett.* 1.7 (1962), pp. 251–253 (cit. on p. 7).

[65] P.W. Anderson and A.H. Dayem. “Radio-Frequency Effects in Superconducting Thin Film Bridges”. In: *Phys. Rev. Lett.* 13 (6 1964), pp. 195–197. DOI: `10.1103/PhysRevLett.13.195` (cit. on p. 7).

[66] L.G. Aslamazov and A.I. Larkin. “Josephson effect in superconducting point contacts”. English. In: *JETP Lett.* 9 (1969), p. 87 (cit. on p. 8).

[67] J. Clarke and A.I. Braginski. *The SQUID handbook: fundamentals and technology of SQUIDs and SQUID Systems, Volume I*. Wiley-VCH Verlag GmbH&Co, KGaA, Weinheim, 2004 (cit. on pp. 8, 12, 15, 16).

[68] H. Greenhouse. “Design of Planar Rectangular Microelectronic Inductors”. In: *IEEE Trans. Parts Hybrids Packag.* 10.2 (1974), pp. 101–109. DOI: `10.1109/TPHP.1974.1134841` (cit. on p. 15).

[69] R. Meservey and P.M. Tedrow. “Measurements of the Kinetic Inductance of Superconducting Linear Structures”. In: *J. Appl. Phys.* 40.5 (1969), pp. 2028–2034. DOI: `10.1063/1.1657905` (cit. on p. 15).

[70] A.J. Annunziata, D.F. Santavicca, L. Frunzio, G. Catelani, M.J. Rooks, A. Frydman, and D.E. Prober. “Tunable superconducting nanoinductors”. In: *Nanotech.* 21.44 (2010), p. 445202. DOI: `10.1088/0957-4484/21/44/445202` (cit. on p. 15).

[71] H. Dausy, L. Nulens, B. Raes, M.J. Van Bael, and J. Van de Vondel. “Impact of Kinetic Inductance on the Critical-Current Oscillations of Nanobridge SQUIDs”. In: *Phys. Rev. Appl.* 16 (2 2021), p. 024013. DOI: `10.1103/PhysRevApplied.16.024013` (cit. on p. 15).

[72] A. Shearrow, G. Koolstra, S.J. Whiteley, N. Earnest, P.S. Barry, F.J. Heremans, D.D. Awschalom, E. Shirokoff, and D.I. Schuster. “Atomic layer deposition of titanium nitride for quantum circuits”. In: *Appl. Phys. Lett.* 113.21 (2018), p. 212601. DOI: `10.1063/1.5053461` (cit. on p. 15).

[73] D. Niepce, J. Burnett, and J. Bylander. “High Kinetic Inductance NbN Nanowire Superinductors”. In: *Phys. Rev. Appl.* 11 (4 2019), p. 044014. DOI: `10.1103/PhysRevApplied.11.044014` (cit. on p. 15).

[74] T. Sekihara, R. Masutomi, and T. Okamoto. “Two-Dimensional Superconducting State of Monolayer Pb Films Grown on GaAs(110) in a Strong Parallel Magnetic Field”. In: *Phys. Rev. Lett.* 111 (5 2013), p. 057005. DOI: `10.1103/PhysRevLett.111.057005` (cit. on p. 15).

[75] M. Frommberger, F. Mattiocco, P. Sabon, M. Schicke, K. Schuster, and O. Laborde. “Properties of Nb Thin Films and their Application for Diffusion-Cooled Hot-Electron Bolometer”. In: (May 2000) (cit. on p. 15).

[76] N.C. Koshnick, M.E. Huber, J.A. Bert, C.W. Hicks, J. Large, H. Edwards, and K.A. Moler. “A terraced scanning super conducting quantum interference device susceptometer with submicron pickup loops”. In: *Appl. Phys. Lett.* 93.24 (2008), p. 243101. DOI: `10.1063/1.3046098` (cit. on pp. 17, 18).

[77] K. Hasselbach, C. Veauvy, and D. Mailly. “MicroSQUID magnetometry and magnetic imaging”. In: *Physica C* 332.1 (2000), pp. 140–147. DOI: `https://doi.org/10.1016/S0921-4534(99)00657-7` (cit. on pp. 17, 18).

[78] M.B. Ketchen, D.D. Awschalom, W.J. Gallagher, A.W. Kleinsasser, R.L. Sandstrom, J.R. Rozen, and B. Bumble. “Design, fabrication, and performance of integrated miniature SQUID susceptometers”. In: *IEEE Trans. Magn.* 25.2 (1989), pp. 1212–1215. DOI: `10.1109/20.92513` (cit. on p. 17).

[79] J.R. Kirtley, M.B. Ketchen, K.G. Stawiasz, J.Z. Sun, W.J. Gallagher, S.H. Blanton, and S.J. Wind. “High-resolution scanning SQUID microscope”. In: *Appl. Phys. Lett.* 66.9 (1995), pp. 1138–1140. DOI: `10.1063/1.113838` (cit. on p. 17).

[80] M.B. Ketchen and J.R. Kirtley. “Design and performance aspects of pickup loop structures for miniature SQUID magnetometry”. In: *IEEE Transactions on Applied Superconductivity* 5.2 (1995), pp. 2133–2136. DOI: `10.1109/77.403004` (cit. on p. 17).

[81] B.W. Gardner, J.C. Wynn, P.G. Bj́ornsson, E.W.J. Straver, K.A. Moler, J.R. Kirtley, and M.B. Ketchen. “Scanning superconducting quantum interference device susceptometry”. In: *Rev. Sci. Instrum.* 72.5 (2001), pp. 2361–2364. DOI: `10.1063/1.1364668` (cit. on p. 17).

[82] J.A. Bert, B. Kalisky, C. Bell, M. Kim, Y. Hikita, H.Y. Hwang, and K.A. Moler. “Direct imaging of the coexistence of ferromagnetism and superconductivity at the LaAlO3/SrTiO3 interface”. In: *Nat. Phys.* 7.10 (2011), pp. 767–771 (cit. on p. 18).

[83] H. Bluhm, J.A. Bert, N.C. Koshnick, M.E. Huber, and K.A. Moler. "Spinlike Susceptibility of Metallic and Insulating Thin Films at Low Temperature". In: *Phys. Rev. Lett.* 103 (2 2009), p. 026805. DOI: `10.1103/PhysRevLett.103.026805` (cit. on p. 18).

[84] K.C. Nowack et al. "Imaging currents in HgTe quantum wells in the quantum spin Hall regime". In: *Nat. Mater.* 12.9 (2013), pp. 787–791 (cit. on p. 18).

[85] W. Wernsdorfer. "From micro- to nano-SQUIDs: applications to nanomagnetism". In: *Supercond. Sci. Tech.* 22.6 (2009), p. 064013. DOI: `10.1088/0953-2048/22/6/064013` (cit. on p. 18).

[86] C. Veauvy, K. Hasselbach, and D. Mailly. "Scanning μ-superconduction quantum interference device force microscope". In: *Rev. Sci. Instrum.* 73.11 (2002), pp. 3825–3830. DOI: `10.1063/1.1515384` (cit. on p. 18).

[87] D.J. Hykel, Z.S. Wang, P. Castellazzi, T. Crozes, G. Shaw, K. Schuster, and K. Hasselbach. "MicroSQUID Force Microscopy in a Dilution Refrigerator". In: *J. Low Temp. Phys.* 175.5 (2014), pp. 861–867 (cit. on p. 18).

[88] C. Veauvy, K. Hasselbach, and D. Mailly. "Micro-SQUID microscopy of vortices in a perforated superconducting Al film". In: *Phys. Rev. B* 70 (21 2004), p. 214513. DOI: `10.1103/PhysRevB.70.214513` (cit. on p. 18).

[89] A. Finkler et al. "Nano-sized SQUID-on-tip for scanning probe microscopy". In: *J. Phys.: Conf. Ser.* 400.5 (2012), p. 052004. DOI: `10.1088/1742-6596/400/5/052004` (cit. on pp. 19, 42, 49).

[90] L. Ceccarelli, D. Vasyukov, M. Wyss, G. Romagnoli, N. Rossi, L. Moser, and M. Poggio. "Imaging pinning and expulsion of individual superconducting vortices in amorphous MoSi thin films". In: *Phys. Rev. B* 100 (10 2019), p. 104504. DOI: `10.1103/PhysRevB.100.104504` (cit. on pp. 19, 49, 61).

[91] D. Vasyukov et al. "Imaging Stray Magnetic Field of Individual Ferromagnetic Nanotubes". In: *Nano Lett.* 18.2 (Feb. 2018), pp. 964–970 (cit. on pp. 19, 49).

[92] M. Wyss, S. Gliga, D. Vasyukov, L. Ceccarelli, G. Romagnoli, J. Cui, A. Kleibert, R.L. Stamps, and M. Poggio. "Stray-Field Imaging of a Chiral Artificial Spin Ice during Magnetization Reversal". In: *ACS Nano* 13.12 (Dec. 2019), pp. 13910–13916 (cit. on pp. 19, 49, 61).

[93] A. Finkler. *Scanning SQUID Microscope for Studying Vortex Matter in Type-II Superconductors*. Jan. 2012. DOI: `10.1007/978-3-642-29393-1` (cit. on pp. 19, 20, 22, 50).

[94] M.E. Huber, P.A. Neil, R.G. Benson, D.A. Burns, A.M. Corey, C.S. Flynn, Y. Kitaygorodskaya, O. Massihzadeh, J.M. Martinis, and G.C. Hilton. "DC SQUID series array amplifiers with 120 MHz bandwidth". In: *IEEE Trans. Appl. Supercond.* 11.1 (2001), pp. 1251–1256. DOI: `10.1109/77.919577` (cit. on p. 38).

[95] L. Ceccarelli. *Scanning probe microscopy with SQUID-on-tip sensor*. 2020. DOI: `10.5451/unibas-ep79793` (cit. on p. 51).

[96] T. H. R. Skyrme and B. F. J. Schonland. "A non-linear field theory". In: *Proc. R. Soc. Lond.* 260.1300 (1961), pp. 127–138. DOI: `10.1098/rspa.1961.0018` (cit. on p. 53).

[97] A. Fert, N. Reyren, and V. Cros. "Magnetic skyrmions: advances in physics and potential applications". In: *Nat. Rev. Mater.* 2.7 (2017), p. 17031 (cit. on pp. 53, 55).

[98] A.A. Kovalev and S. Sandhoefner. “Skyrmions and Antiskyrmions in Quasi-Two-Dimensional Magnets”. In: *Frontiers in Physics* 6 (2018). DOI: 10.3389/fphy.2018.00098 (cit. on pp. 53, 54).

[99] S. Ḿuhlbauer, B. Binz, F. Jonietz, C. Pfleiderer, A. Rosch, A. Neubauer, R. Georgii, and P. B́oni. “Skyrmion Lattice in a Chiral Magnet”. In: *Science* 323.5916 (2009), pp. 915–919. DOI: 10.1126/science.1166767 (cit. on pp. 54, 57).

[100] X.Z. Yu, Y. Onose, N. Kanazawa, J.H. Park, J.H. Han, Y. Matsui, N. Nagaosa, and Y. Tokura. “Real-space observation of a two-dimensional skyrmion crystal”. In: *Nature* 465.7300 (2010), pp. 901–904 (cit. on pp. 54, 57).

[101] I. Dzyaloshinsky. “A thermodynamic theory of ”weak” ferromagnetism of antiferromagnetics”. In: *J. Phys. Chem. Solids* 4.4 (1958), pp. 241–255. DOI: https://doi.org/10.1016/0022-3697(58)90076-3 (cit. on p. 54).

[102] T. Moriya. “Anisotropic Superexchange Interaction and Weak Ferromagnetism”. In: *Phys. Rev.* 120 (1 1960), pp. 91–98. DOI: 10.1103/PhysRev.120.91 (cit. on p. 54).

[103] W. Kang, Y. Huang, X. Zhang, Y. Zhou, and W. Zhao. “Skyrmion-Electronics: An Overview and Outlook”. In: *Proceedings of the IEEE* (Aug. 2016), pp. 1–22. DOI: 10.1109/JPROC.2016.2591578 (cit. on p. 55).

[104] S. Parkin and S.-H. Yang. “Memory on the racetrack”. In: *Nat. Nanotech.* 10.3 (2015), pp. 195–198 (cit. on p. 55).

[105] X. Zhang, Y. Zhou, M. Ezawa, G.P. Zhao, and W. Zhao. “Magnetic skyrmion transistor: skyrmion motion in a voltage-gated nanotrack”. In: *Sci. Rep.* 5.1 (2015), p. 11369 (cit. on p. 55).

[106] X. Zhang, M. Ezawa, and Y. Zhou. “Magnetic skyrmion logic gates: conversion, duplication and merging of skyrmions”. In: *Sci. Rep.* 5.1 (2015), p. 9400 (cit. on p. 55).

[107] A.V. Chumak, A.A. Serga, and B. Hillebrands. “Magnonic crystals for data processing”. In: *J. Phys. D: Appl. Phys.* 50.24 (2017), p. 244001. DOI: 10.1088/1361-6463/aa6a65 (cit. on p. 56).

[108] F. Ma, Y. Zhou, H.B. Braun, and W.S. Lew. “Skyrmion-Based Dynamic Magnonic Crystal”. In: *Nano Lett.* 15.6 (June 2015), pp. 4029–4036 (cit. on p. 56).

[109] Y. Tokura and N. Kanazawa. “Magnetic Skyrmion Materials”. In: *Chem. Rev.* 121.5 (Mar. 2021), pp. 2857–2897 (cit. on p. 56).

[110] A. Bauer and C. Pfleiderer. “Generic Aspects of Skyrmion Lattices in Chiral Magnets”. In: *Topological Structures in Ferroic Materials: Domain Walls, Vortices and Skyrmions*. Ed. by Jan Seidel. Cham: Springer International Publishing, 2016, pp. 1–28. DOI: 10.1007/978-3-319-25301-5_1 (cit. on p. 56).

[111] J. Masell, X. Yu, N. Kanazawa, Y. Tokura, and N. Nagaosa. “Combing the helical phase of chiral magnets with electric currents”. In: *Phys. Rev. B* 102 (18 2020), p. 180402. DOI: 10.1103/PhysRevB.102.180402 (cit. on pp. 56, 57).

[112] P. Milde et al. “Unwinding of a Skyrmion Lattice by Magnetic Monopoles”. In: *Science* 340.6136 (2013), pp. 1076–1080. DOI: 10.1126/science.1234657 (cit. on p. 57).

[113] T. Adams, A. Chacon, M. Wagner, A. Bauer, G. Brandl, B. Pedersen, H. Berger, P. Lemmens, and C. Pfleiderer. “Long-Wavelength Helimagnetic Order and Skyrmion Lattice Phase in Cu_2OSeO_3”. In: *Phys. Rev. Lett.* 108 (23 2012), p. 237204. DOI: 10.1103/PhysRevLett.108.237204 (cit. on p. 58).

[114] S. Seki, J.-H. Kim, D. S. Inosov, R. Georgii, B. Keimer, S. Ishiwata, and Y. Tokura. "Formation and rotation of skyrmion crystal in the chiral-lattice insulator Cu_2OSeO_3". In: *Phys. Rev. B* 85 (22 2012), p. 220406. DOI: `10.1103/PhysRevB.85.220406` (cit. on p. 58).

[115] J.S. White et al. "Electric-Field-Induced Skyrmion Distortion and Giant Lattice Rotation in the Magnetoelectric Insulator Cu_2OSeO_3". In: *Phys. Rev. Lett.* 113 (10 2014), p. 107203. DOI: `10.1103/PhysRevLett.113.107203` (cit. on p. 58).

[116] J.S. White, I. Živković, A.J. Kruchkov, M. Bartkowiak, A. Magrez, and H.M. R´onnow. "Electric-Field-Driven Topological Phase Switching and Skyrmion-Lattice Metastability in Magnetoelectric Cu_2OSeO_3". In: *Phys. Rev. Appl.* 10 (1 2018), p. 014021. DOI: `10.1103/PhysRevApplied.10.014021` (cit. on p. 58).

[117] F. Qian et al. "New magnetic phase of the chiral skyrmion material Cu_2OSeO_3". In: *Science Adv.* 4.9 (2018), eaat7323. DOI: `10.1126/sciadv.aat7323` (cit. on p. 58).

[118] P. Milde, L. K´ohler, E. Neuber, P. Ritzinger, M. Garst, A. Bauer, C. Pfleiderer, H. Berger, and L.M. Eng. "Field-induced reorientation of helimagnetic order in Cu_2OSeO_3 probed by magnetic force microscopy". In: *Phys. Rev. B* 102 (2 2020), p. 024426. DOI: `10.1103/PhysRevB.102.024426` (cit. on p. 58).

[119] L.J. Bannenberg, H. Wilhelm, R. Cubitt, A. Labh, M.P. Schmidt, E. Leliévre-Berna, C. Pappas, M. Mostovoy, and A.O. Leonov. "Multiple low-temperature skyrmionic states in a bulk chiral magnet". In: *npj Quantum Mater.* 4.1 (2019), p. 11 (cit. on p. 68).

[120] P. Che. *Helimagnons and Skyrmion Dynamics in Cu2OSeO3 and Fe/Gd Multilayers Explored by Brillouin Light Scattering and X-ray Microscopy*. Lausanne: EPFL, 2021, p. 183. DOI: `10.5075/epfl-thesis-8280` (cit. on p. 68).

[121] A. Aqeel, J. Sahliger, T. Taniguchi, S. M´andl, D. Mettus, H. Berger, A. Bauer, M. Garst, C. Pfleiderer, and C.H. Back. "Microwave Spectroscopy of the Low-Temperature Skyrmion State in Cu_2OSeO_3". In: *Phys. Rev. Lett.* 126 (1 2021), p. 017202. DOI: `10.1103/PhysRevLett.126.017202` (cit. on p. 68).

[122] G.P. Müller, M. Hoffmann, C. Disselkamp, D.l Sch´urhoff, S. Mavros, M. Sallermann, N.S. Kiselev, H. Jónsson, and S. Blügel. "Spirit: Multifunctional framework for atomistic spin simulations". In: *Phys. Rev. B* 99 (22 2019), p. 224414. DOI: `10.1103/PhysRevB.99.224414` (cit. on p. 71).

[123] C. Tschirhart et al. "Imaging orbital ferromagnetism in a moiré Chern insulator". In: *Science* 372 (May 2021), eabd3190. DOI: `10.1126/science.abd3190` (cit. on p. 79).

[124] T. Kurumaji, T. Nakajima, V. Ukleev, A. Feoktystov, T. Arima, K. Kakurai, and Y. Tokura. "Néel-Type Skyrmion Lattice in the Tetragonal Polar Magnet $VOSe_2O_5$". In: *Phys. Rev. Lett.* 119 (23 2017), p. 237201. DOI: `10.1103/PhysRevLett.119.237201` (cit. on p. 79).

[125] K.F. Mak, J. Shan, and D.C. Ralph. "Probing and controlling magnetic states in 2D layered magnetic materials". In: *Nat. Rev. Phys.* 1.11 (2019), pp. 646–661 (cit. on p. 80).

[126] A. Avsar, A. Ciarrocchi, M. Pizzochero, D. Unuchek, O.V. Yazyev, and A. Kis. "Defect induced, layer-modulated magnetism in ultrathin metallic $PtSe_2$". In: *Nat. Nanotech.* 14.7 (2019), pp. 674–678 (cit. on p. 80).

[127] A. Avsar, C.-Y. Cheon, M. Pizzochero, M. Tripathi, A. Ciarrocchi, O.V. Yazyev, and A. Kis. "Probing magnetism in atomically thin semiconducting $PtSe_2$". In: *Nat. Comm.* 11.1 (2020), p. 4806 (cit. on p. 80).

[128] Y. Zhao et al. "High-Electron-Mobility and Air-Stable 2D Layered $PtSe_2$ FETs". In: *Adv. Mater.* 29.5 (2017), p. 1604230. DOI: `https://doi.org/10.1002/adma.201604230` (cit. on p. 80).

[129] X. Yu et al. "Atomically thin noble metal dichalcogenide: a broadband mid-infrared semiconductor". In: *Nat. Commun.* 9.1 (2018), p. 1545 (cit. on p. 80).

[130] Sutter Instrument. *P-2000 Laser-Based Micropipette Puller System, operation manual*. 2020 (cit. on p. 91).

Appendix A

Laser-pulling quartz capillaries

Laser-pulling quartz capillaries, for both normal and grooved pipettes, was performed by using the commercial P-2000 laser puller. A full manual [130] can be found at Sutter Instrument website. In the following an introduction about the device is presented, followed by an explanation of how to tune the parameters to influence the final result.

A.1 Introduction

The P-2000 is a microprocessor controlled, CO_2 laser-based micropipette puller. It allows to fabricate micro- or nano-pipettes for intracellular recording, patch clamping, microinjection and microperfusion. The main advantage of using a heat source such as a CO_2 laser is the ability to work with quartz (fused silica) glass, a much more pure, stronger and stiffer glass formulation than standard glass capillary tubing. All other lower melting point glasses, such as aluminosilicate or borosilicate can be pulled as well.

The model of P-2000 used in this work is the P2000/G, the one outfitted to be used for glass capillaries with outer diamater (OD) in the range 0.6 - 1.5 mm. Note that the best performances are achieved with capillaries with OD of 1.2 mm or less. All our work involved 1 mm OD quartz capillaries.

A sketch of the pulling process is showed in Figure A.1, where a side and top view are reported. The capillary is clamped in such a way it stands few millimiters away from the concave gold-coated surface of the retromirror, the cross sectional area (or back face) being on the optical pathway of the laser light. The CO_2 laser beam is projected onto the back face of the glass by a reflective scanning mirror, which is mounted onto a rotating base. Heating of the glass is obtained by repeatedly scanning the mirror horizontally between limits that can be set by the user. The scanning mirror is mounted on a tilting table, whose degree of tilt is controlled by the tilt micrometer. The tilt determines the elevation of the laser beam relative to the glass. Every time the puller gets relocated or the capillary shape change (for instance a new OD) or whenever consistently bad pulling outcomes are observed, is good to check the tilt correction. For that we refer to the manual [130].
The incident beam component that exits the capillary is collected by the retromirror. The retromirror redirects the divergent laser light back towards the front side of the glass, in such a way the capillary receives a uniform heating around its circumference. The two-stage manipulator consists in two screws that allow for tuning the horizontal and vertical position of the retromirror. Changing the vertical or the horizontal position will determine a different influence of the retroreflected light on the

capillary and consequently will lead to different shapes and final diameters.

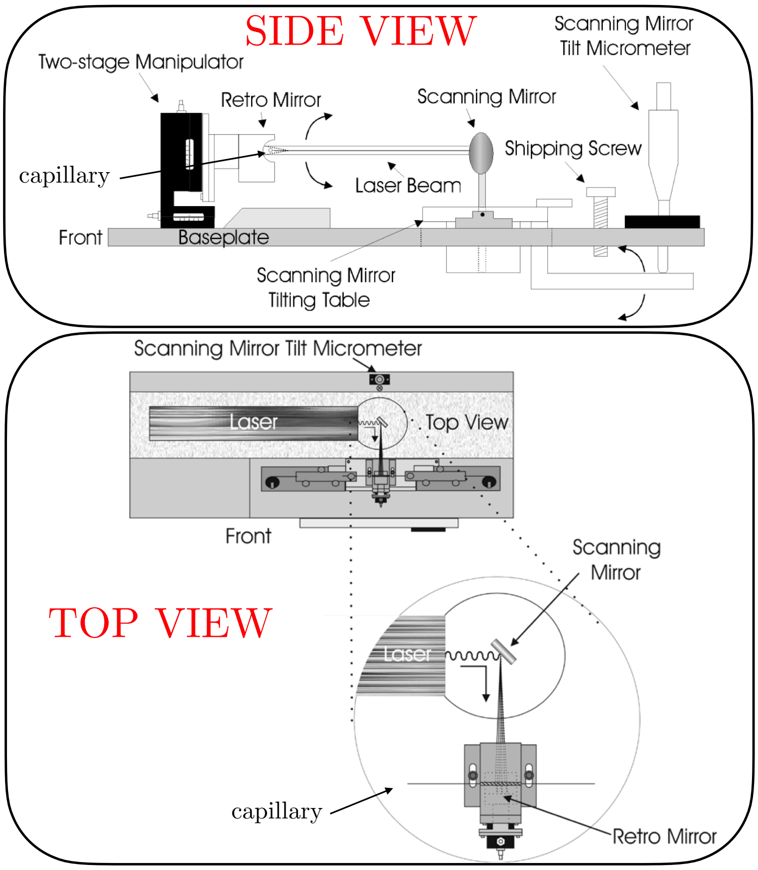

FIGURE A.1: Side- and top-view sketches of the optical pathway.

A.2 Pulling cycle

A pulling program is made of one or more (up to 8) cycles, also called lines, each of them consists of five programmable parameters and determines a pulling process. The parameters are defined as follows:

- **HEAT**: range from 0 to 999. This parameter sets the amount of energy supplied by the laser to the capillary, so it measures the output power of the laser. The HEAT needed to melt a piece of glass is a function of the glass material and OD and of the chosen value of filament. Quartz do require high heat values around 700 or more. Changes to HEAT should be made in steps of 10 units in order to see some significative effect.
  The HEAT setting affects length and tip size of the capillary. Usually, high values of HEAT generate very fine and long tapered pipettes. It does have an influence on the total pulling time as well, since higher HEAT values correspond to shorter pulling times. To make a process the most reproducible as possible, the pulling time should be in the range 4 - 8 seconds. In fact, shorter processes turn out to be too fast and not controllable, while processes longer than 10 seconds lead to a variability in the laser operation which affects reproducibility. So HEAT should be adjusted as a consequence of the pulling time.

- **FILAMENT**: range from 0 to 5. It specifies the scanning pattern of the laser beam used to scan and heat the glass. Every value corresponds to a different scan length and rate: 0 FILAMENT value means 1 mm scan length, 0 = 1 mm; 1 = 1.5 mm; 2 = 1.9 mm; 3 = 4.5 mm; 4 = 6.5 mm; 5 = 8 mm. For a fixed value of HEAT, FILAMENT parameter determines the applied power per unit length of glass. Clearly it drastically affects the pulling time.
- **VELOCITY**: range from 0 to 255. While HEAT is applied, a soft pull is carried out. The glass starts to soften and begins to pull apart under a constant load, while in the meantime the machine is measuring the speed (or VELOCITY) at which the carrier bars holding the pipette are moving. The increasing speed of the initial pull is determined by the viscosity of the glass, which is a function of its temperature. So VELOCITY represents an indirect measurement of how warm the capillary is. The chosen VELOCITY value sets the glass temperature (called trip point) at which the HEAT is turned off and the hard PULL starts. For the quartz micropipettes of interest, typical values are in the range 45 - 60. In a multiple cycle process, as the ones used in this work, it is important to decrease the VELOCITY in the next to last line of the program. This leads to an increased amount of glass left at the beginning of the last program cycle and avoids the glass to not separate during the soft pull part.
- **DELAY**: range from 0 to 255. It controls the time between when the HEAT turns off and when the hard PULL is activated. A zero time gap between the trip point and the beginning of hard PULL corresponds to DELAY = 128. Time differences (DELAY - 128), which can be negative values, are time measurements in milliseconds. A value of DELAY smaller than 128 means that the hard PULL is initiated before the laser power is turned off.
  Clearly, the higher the DELAY the cooler the glass will be when the hard PULL is executed and bigger will be the outcome diameter. Furthermore, extremely important, a temperature gradient proportional to DELAY is set between inner (hot) and outer part (cold) of the capillary, which is required when very high hard PULL is exerted. So high DELAY values are the key the achieve final diameters in the 50 nm range. For quartz capillaries, the usual range is 100 - 140, but even 150 can be used if PULL values close to the machine limit are applied.
- **PULL**: range from 0 to 255. It determines the force of the hard pull. Usually, the higher the PULL, the smaller the pipette's tip diameter and longer the taper. Even though every value can be used with no damage for the machine, a good advice is to make sure the pipette is well clamped inside the carrier bars if PULL values around 200 or more are applied. In case the pipette is not well clamped, the risk is to break it in proximity to the retromirror when the hard pull starts. This can cause a damage of the retromirror, such as a scratch of its gold-coated surface. Any damage to it is irreversible and can be fixed only by installing a new mirror. In our case values up to 220 were tested without any issue.

A.3 Pulling quartz capillaries with a P2000 laser puller

In the following, the intention is to report few important notions to keep in mind while pulling quartz capillaries with the P2000 laser puller. They are the result of a fruitful communication over the years with the specialists from Sutter instrument company and lot of time invested on laser-pulling, with tens of tests and failures. These suggestions should be seen as a guidance to avoid possible common mistakes and a way to improve the reproducibility of the process. In bullet points, item by item:

- **Tickle for the laser system**. For the P2000 machine, laser system is activated by very brief pulses delivered to the laser system RF driver circuit board. Pulses are too short to produce a significant amount of laser power, but they are needed to set the laser tube in the ideal state to deliver power when is needed. So, in other words, tickle guarantees that the laser will start correctly when the integrated microprocessor calls for laser power. In order to obtain the full advantage of this process, a certain amount of time has to be waited after closing the cover before starting the pulling program.
  Ideal amount of time according to the manual is 4 seconds, but we experimented that 7 - 8 seconds give very consistent pulling results.
- **Uneven taper length**. Sometimes it is found that the two tapers in output of the process are not equal in length. This most likely is the result of focusing laser power to a glass whose diameter was reduced too much. In fact, when things work correctly, glass draws down in diameter as the laser power becomes more concentrated due to the retromirror and the mass of glass to be heated per unit length decreases. Time to melt for the glass drops and as a consequence glass melts firstly at its smallest point. However, if the smallest point of the hourglass becomes too small, eventually glass no longer melts firstly at its smallest diameter. For instance, this can happen if a too high velocity value is set, since the soft pull keeps pulling the hourglass from the two sides until the trip point is reached.
  To avoid this issue, typical of multiline processes, make sure that the next to last line of the program doesn't draw the diameter of the hourglass down to too small diameters. To this aim, reduce heat or velocity on the next to last line, and avoid very high velocity settings and delay values less than 128 on the last line.
- **Taking care of the retromirror**. The gold-coated retromirror surface is positioned very close to the target pipette and can get coated with materials originated by the heating process of the glass. This is most likely due to a wrong handling of the capillary, which gets dirty of oil from fingers or other stuff. In the worst case, after heavy use, very aggressive deposits can penetrate the gold coating and damage the retromirror. At that point, the only solution is to install and set a new mirror, which absolutely is not a straightforward process. For not specialist users, it can take up to two weeks to converge to a working setting.
  Few suggestions to avoid such an issue are:
  - Always use gloves to handle the capillaries, better two pairs.
  - For any reason, not even by wearing gloves, touch the center part of the glass pipette, which is the one that will be heated by the laser.
  - Commercial pipettes are pre-cleaned when purchased. However, good practice is to clean them inside and outside with acetone and isopropanol and dry them with nitrogen gun.
  - Laser puller is very sensitive to dust. Despite the retromirror is protected inside the two-stage manipulator box, it is better to place the machine in

  a clean environment, such as a cleanroom or a box with outgoing flow of filtered air (the latter is our case).
  - Often inspecting and cleaning the mirror. This can be done by using optical paper, which doesn't release particles, wet by methanol or, even better, ethanol. For a heavily used laser puller, the retromirror should be cleaned at least once per week. In our case once per month is enough.

- **Adjustments of retromirror position**. After the pulling process, tip pipette is supposed to be concentric with the shaft. If not, it means that the pipette is not heated symmetrically and the optical pathway of the laser beam has to be adjusted. Our way to quantitatively determine how concentric the tips are is described in the dedicated Sec. A.4. Here I focus on few crucial details.
  By default, company aligns the retromirror of the P2000 puller in such a way it produces concentric tips when pulling 1 mm OD quartz pipettes with a one heating cycle (or line) program. In other words, whenever a two or more heating cycles program is applied, the tip is expected to be off centered compared to its long rotation axis. The offset depends on the chosen program and can range from almost 0 to even more than 100 μm. When the offset becomes too big, certain issues can take place, such as an asymmetry in the coating of the superconducting electrodes due to the different pipette curvature on the two sides. Moreover, the coupling to the QPlus tuning fork (Cit. Chap 2) can be problematic. The experience with the Qplus made us estimating a maximum tolerable offset of 50 - 60 μm. To reduce the offset and make the tips concentric, adjustments might have to be made on both vertical and horizontal positions of the retromirror.
  First thing to do after pulling a test pipette is to take a reference on the glass as viewing it from the top and from the front of the machine. This allows to determine whether the tip is asymmetric if looked from the front or from the top. Front (top) misalignment means that the mirror vertical (horizontal) position has to be corrected. To adjust the position of the retromirror, the two-stage manipulator can be used. Two set screws allow to change either the horizontal or the vertical position, moving the mirror forwards/backwards and upwards/downwards. Important to know, a full turn of the screw corresponds to a movement of the mirror of about 500 μm, and the outcome of a pulling program is really sensitive to changes of mirror position of 30 - 50 μm. So we recommend to start by changing the position by 1/16 of full turn and repeat the same pulling program and determine whether there was an improvement or not. If not, then it means that the screw has to be turned in the opposite direction, and restart by turning it by 1/16 of full turn. In few iterations, a decent visual concentricity can be reached. For further analysis, we refer to Sec. A.4.

- **Role of DELAY while pulling quartz pipettes**. Quartz glass softens at a very high temperature, but the transition from stiff to soft occurs over a fairly small temperature range. This allows temperature gradients across the tube's wall to produce layers of glass that differ in stiffness. The laser power is absorbed near the surface and must conduct towards the center before the inner layer can soften. When the trip point (or velocity setpoint) is reached and laser power is turned off, heat is lost from the surface layers, while heat in deeper layers continues to conduct towards the inner wall. The result is a reversal of the temperature gradient at some point in time after the laser turns off.
  When the glass draws, large temperature gradients cause the wall thickness

to decrease more rapidly than the outer diameter of the glass. This makes the glass less stiff and also limits how small a tip can be formed. In order to avoid this issue, the DELAY time before activating the hard PULL has to be chosen very wisely. Value of DELAY has be long enough to allow the temperature gradient to reduce, but short enough to maintain the glass still soft enough to draw.

The best DELAY time depends on the other program values and needs to be determined by trial and error. However, we can state that high PULL values complete the draw more quickly, so they require a longer DELAY to maintain a good walls thickness. In fact, low DELAY and high PULL are expected to produce thinning of quartz pipette walls. Increasing the DELAY will result as well in cooler glass at the start of the hard PULL. This leads to an increased final diameter of the tip. If small diameter tips are required, then HEAT or VELOCITY have to be increased to ensure that the glass will still be hot enough to draw properly when the hard PULL turns on.

A.4 Determining tip concentricity and tip diameter

The relevance of tip concentricity was already mentioned, here the procedure to estimate tip concentricity and final diameter is reported. Despite the same tip concentricity estimation could be achieved by using an optical microscope with a reticule in the eyepiece, for practical reasons we decide to combine concentricity to diameter measurement, which requires a Scanning Electron Microscope (SEM).

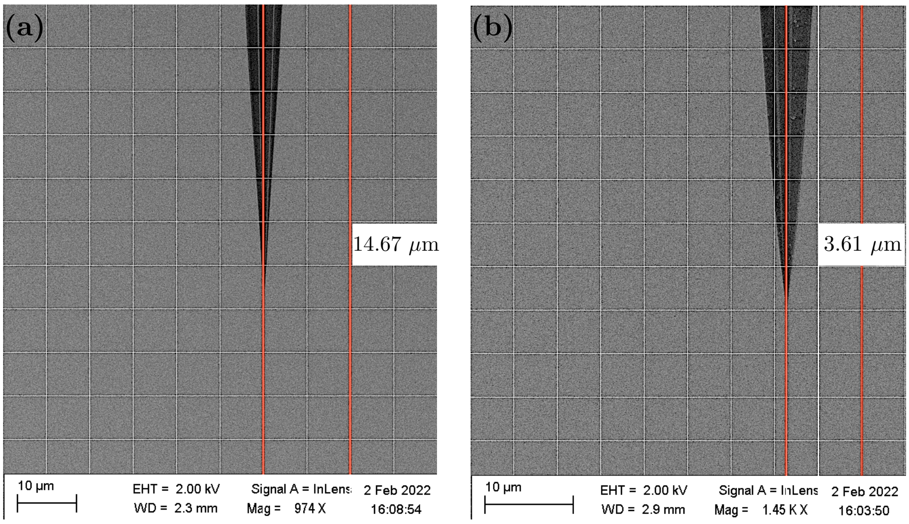

FIGURE A.2: Estimation of the concentricity for two quartz nano-pipettes, as looked from the top (horizontal alignment of the mirror). The one in (a), of diameter 55 nm, shows an offset of 14 μm; the tip in (b), corresponding to a diameter of 180 nm, has an offset of 3 μm. Both offsets are way within our tolerance threshold of 50 μm.

After pulling program, the front and top surfaces of the pipette shaft (the unpulled portion of the capillary) are marked before the pipette is removed from the puller. Then it is transfered to SEM, where it is imaged using a very low acceleration voltage (2 KV) and at a short working distance of about 2 mm. SEM software is equipped with many tools that can help in the measurement of the concentricity, one of them being a graticule that resembles the reticule in the eyepiece of an optical microscope. The pipette is rotated until is perfectly aligned with the graticule: this means that, by moving the SEM stage along the pipette towards the tip, the edges of the capillary don't move with respect to the graticule and the computer screen edges. Once the tip is found, it can look off-centered with respect to the graticule center, which corresponds to the symmetry axis of the pipette. At this point, it is immediate to measure how much the off-centering is.

An example is showed in Figure A.2, where two tips corresponding to different pulling programs are imaged as viewed from the top of the puller. This means investigating the quality of the horizontal alignment of the retromirror. Panel (a) reports an offset of about 14 μm, while Panel (b) an offset of 3 μm. Both offsets are minimal and way below the tolerance threshold set by the coupling to the QPlus tuning fork. For this reason, in both cases no further alignment of the retromirror is needed.

After checking the off-centering, the graticule is removed and an image of the tip is acquired. Figure A.3 shows the corresponding apex for the two tips of Figure A.2. The pipette in Panel (a) has a diameter of 55 nm, one of the smallest ever pulled, while the pipette in Panel (b) has a diameter of 180 nm, which represents a more conventional tip for SPM experiment. In fact, not many samples studied so far by our group required a spatial resolution below 100 nm. For this reason, often the pulling program aims to produce quartz capillaries with a diameter in the range 100 - 200 nm, which are expected to give SQUIDs with higher sensitivity.

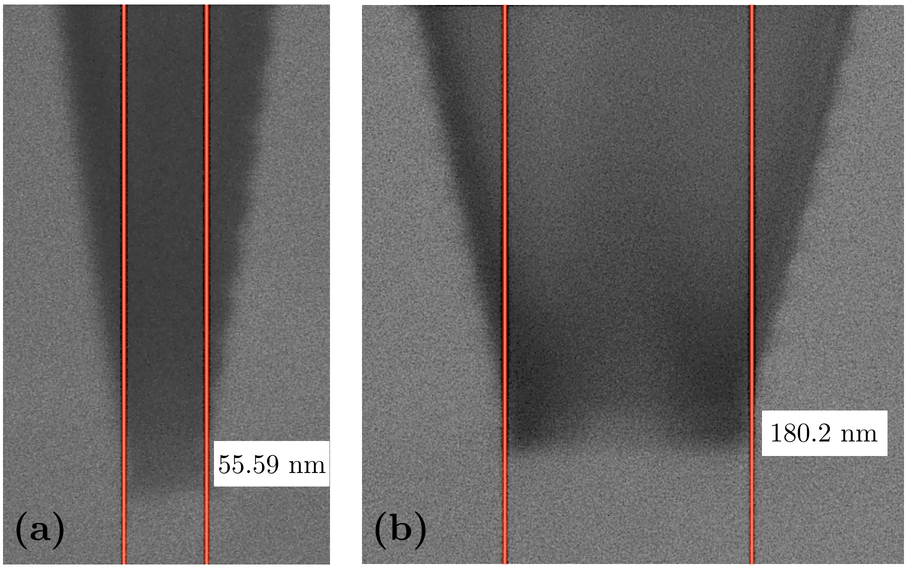

FIGURE A.3: SEM picture of two quartz capillaries after the pulling process. The blurriness in the pictures comes from imaging bare quartz (insulating) nano-scale objects and would disappear if the tips were coated with a metal layer. (a) 55 nm diameter tip, one of the smallest ever pulled; (b) a more traditional tip for our SPM experiments, with diameter of 180nm.

Few final comments on the tip apex: it is immediate to notice that the picture is not of high quality and presents some blurriness. This is because the bare quartz pipettes are imaged, without any metal coating. Imaging an insulating material with the aim of resolving a nano-scale object is quite challenging and requires a certain speed in zooming in and adjusting the focus, before the tip starts distorting due to charging effects. Furthermore, no integration time for reducing background noise can be used. As soon as the feature is zoomed in, screen gets frozen and the image is acquired. The choice of where to place the cursors gives some imprecision as well in the measurement of the diameter. This is acceptable, since the aim is just to have an estimation. As far as the imaging technique is similar, we expect to have consistent imaging results. In particular, it must be taken into account that the effective diameter of the SQUID after coating the pipette with superconducting film is usually 10 - 20 % more than what expected after SEM imaging.

A.5 Book of recipes

Here I report the most used 2-lines pulling programs for quartz tips. I divide the section in two parts: firstly, the recipes for 1 mm OD, 0.5 mm ID pipettes (Figure 2.1(a)) are reported, while in the second part the recipes for the custom four-grooves capillaries (as the ones showed in Figure 2.1(b)) are presented. For every recipe the expected pulling time, diameter and, when known, concentricity are specified.

A.5.1 Not groovy capillaries, 1 mm OD, 0.5 mm ID

1. **RECIPE**:

HEAT	**FIL**	**VEL**	**DEL**	**PULL**
700	4	40	140	60
600	3	50	135	96

- Pulling time: 6.5 - 6.8 sec
- SEM diameter: 200 nm

2. **RECIPE**:

HEAT	**FIL**	**VEL**	**DEL**	**PULL**
700	4	40	140	60
600	3	50	140	137

- Pulling time: 6.2 - 6.6 sec
- SEM diameter: 120 nm

3. **RECIPE**:

HEAT	**FIL**	**VEL**	**DEL**	**PULL**
700	4	40	140	60
600	3	50	140	160

- Pulling time: $\sim$ 6.9 sec
- SEM diameter: 95 nm

4. **RECIPE**:

HEAT	**FIL**	**VEL**	**DEL**	**PULL**
700	4	40	140	60
600	3	50	140	170

- Pulling time: $\sim$ 6.6 sec

- SEM diameter: 70 nm

5. **RECIPE**:

HEAT	FIL	VEL	DEL	PULL
700	4	40	140	60
600	3	50	140	180

- Pulling time: $\sim$ 6.8 sec
- SEM diameter: 65 nm

6. **RECIPE**:

HEAT	FIL	VEL	DEL	PULL
700	4	40	140	60
600	3	50	140	190

- Pulling time: $\sim$ 6.8 sec
- SEM diameter: 60 nm

7. **RECIPE**:

HEAT	FIL	VEL	DEL	PULL
700	4	40	140	60
600	3	50	138	121

- Pulling time: 6.6 - 6.9 sec
- SEM diameter: (150 ± 5) nm

8. **RECIPE**:

HEAT	FIL	VEL	DEL	PULL
715	4	40	140	100
610	3	50	140	140

- Pulling time: 5.9 - 6.3 sec
- SEM diameter: (100 ± 10) nm

9. **RECIPE**:

HEAT	FIL	VEL	DEL	PULL
700	4	40	130	60
600	3	50	140	120

- Pulling time: 6.8 - 7.1 sec
- SEM diameter: 150 nm

A.5.2 Custom 4-grooves capillaries, 1 mm OD, 0.4 mm ID

1. **RECIPE**:

HEAT	FIL	VEL	DEL	PULL
700	4	40	140	60
600	3	50	140	170

- Pulling time: 6.4 - 6.8 sec
- Vertical offset: 20 μm; Horizontal offset: 30 μm
- SEM diameter: 80 - 85 nm

2. **RECIPE:**

HEAT	FIL	VEL	DEL	PULL
700	4	40	140	60
600	3	50	140	160

- Pulling time: 6.6 - 6.8 sec
- Vertical offset: 30 μm; Horizontal offset: 35 μm
- SEM diameter: 90 nm

3. **RECIPE:**

HEAT	FIL	VEL	DEL	PULL
690	4	40	140	60
570	3	48	138	156

- Pulling time: 5.9 - 6.3 sec
- Vertical offset: 10 μm; Horizontal offset: 20 μm
- SEM diameter: 105 - 110 nm

4. **RECIPE:**

HEAT	FIL	VEL	DEL	PULL
690	4	40	140	60
570	3	48	142	210

- Pulling time: 6.5 - 6.9 sec
- Vertical offset: 20 μm; Horizontal offset: 30 μm
- SEM diameter: 70 - 80 nm

5. **RECIPE:**

HEAT	FIL	VEL	DEL	PULL
690	4	40	140	60
570	3	48	134	135

- Pulling time: 5.9 - 6.3 sec

- Vertical offset: ~ 0 μm; Horizontal offset: ~ 0 μm
- SEM diameter: 90 nm

6. **RECIPE**:

HEAT	**FIL**	**VEL**	**DEL**	**PULL**
690	4	40	140	60
570	3	48	134	124

- Pulling time: 6.3 - 6.6 sec
- Vertical offset: ~ 0 μm; Horizontal offset: ~ 0 μm
- SEM diameter: 130 nm

7. **RECIPE**:

HEAT	**FIL**	**VEL**	**DEL**	**PULL**
690	4	40	140	60
570	3	60	134	110

- Pulling time: 5.9 - 6.2 sec
- Vertical offset: ≤ 10 μm; Horizontal offset: ≤ 10 μm
- SEM diameter: 160 nm

8. **RECIPE**:

HEAT	**FIL**	**VEL**	**DEL**	**PULL**
710	4	45	135	60
700	4	60	135	220

- Pulling time: 5.6 - 5.8 sec
- Vertical offset: ~ 0 μm; Horizontal offset: ~ 0 μm
- SEM diameter: 50 nm

9. **RECIPE**:

HEAT	**FIL**	**VEL**	**DEL**	**PULL**
710	4	45	135	60
700	4	60	135	170

- Pulling time: 5.6 - 5.8 sec
- Vertical offset: ≤ 10 μm; Horizontal offset: ≤ 10 μm
- SEM diameter: 90 nm

10. **RECIPE**:

HEAT	**FIL**	**VEL**	**DEL**	**PULL**
690	4	40	140	60
570	3	60	134	100

- Pulling time: 6 - 6.5 sec
- Vertical offset: $\leq 20\ \mu$m; Horizontal offset: $\leq 20\ \mu$m
- SEM diameter: 200 nm

Appendix B

Common issues in Pb deposition

As mentioned in Chap. 2, Pb thermal evaporation is not a straightforward process and can lead to failures due to many reasons. In Figure B.1 we show the outcome of common issues, where the scale bar in every picture is 100 nm. For every SOT the corresponding explanation is included.

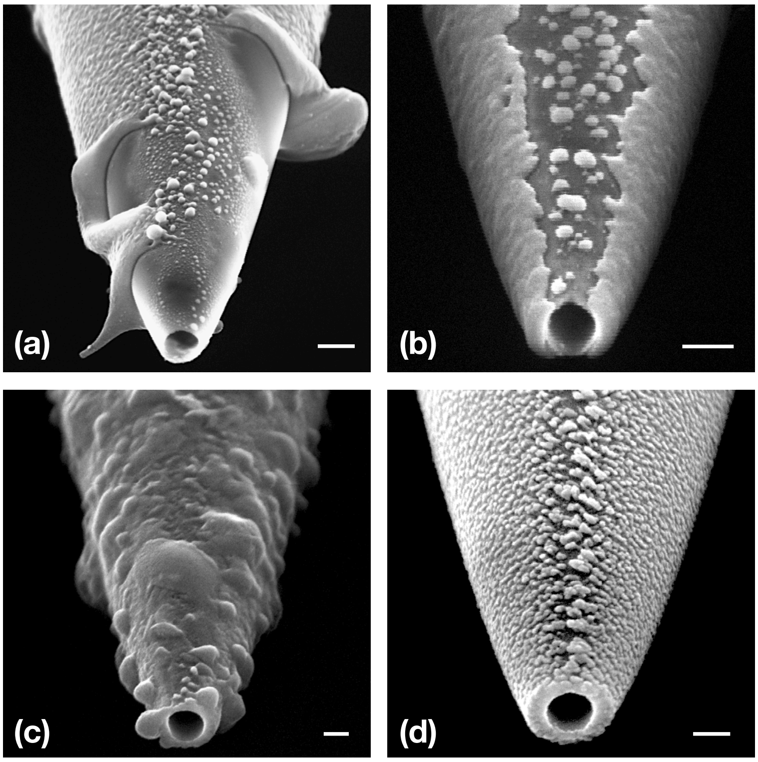

FIGURE B.1: Failed attempts in fabricating Pb SOTs. The scale bar in every figure is 100 nm. (a) Electrostatic discharge, an effect of improper grounding of the SOT or of who is handling the SOT after the fabrication. The result is similar to an explosion, with the Pb film lifted off from the capillary. (b) Missing weak links. This can be due to a not optimal pulling process, breaking the quartz capillary so that the apex is not flat. Pb islands struggle to coat the rough surface and one or both junctions are missing. Too big evaporation angles can contribute to this issue, because they elongate the weak link. (c) Thermal issue, due to a lack of cooling of the quartz capillary. When the surface to be coated is not cold enough, instead of forming a nice thin film, Pb islands create disordered bubbles, coating the whole pipette. (d) Missing gap between the superconducting leads, probably due to small evaporation angles. This phenomenon happens more often when the diameter of the SOT gets reduced and no grooves are present.

Acknowledgements

In first place I would like to thank Prof. Martino Poggio for welcoming me in his group and allowing me to conduct my research in the Poggio Lab. It was a great experience, at a personal and scientific level, and this would have not be possible without your guidance and support. I could mention so many moments and adventures over the years, for which I am extremely greteful. Again, I think of you as one of the best people I met so far and I am so glad for this. Thank you and I wish we keep this connection in the incoming years.

Thank you as well to Prof. Ilaria Zardo, my second supervisor, for the innumerable discussions over the years. Always cheering me up in difficult times, when research was frustrating. Thanks also to Dr. Amit Finkler for being my external referee in the doctoral committee. Your corrections, experience in the topic and attention to details was truly helpful.

The research experience is as pleasent and valuable as the people you spend your days, evenings, good and bad moments with. In Poggio Lab, over the years, I had the pleasure of being surrounded by special people.

When I joined the group, and I felt a bit lost due to change of environment, I immediately bonded with the italian side of Poggio guys. In particular, Nicola, Davide and Lorenzo. With Nicola I don't even know where to start from. He helped me moving from Baselland to Kaserne, he introduced me to the hobby (cycling) that now I love the most, we spent hours playing ping-pong of the rooftop of the department and commenting any kind of sport. Some of the best cycling adventures were completed together. I cannot be more grateful to you for all these moments together. Memorable are also the evenings spent in the office playing Magic with you, Davide and Lorenzo. So many good games, topped with good laughs, pizzas and beers.

About the SOT team, I would like to thank Denis for introducing me to the lab, it was a pleasure to work together and learn so many valuable tricks. Thanks as well to Marcus, our local rock-star, the basler Gallagher. I won't never forget the FC Basel games together and especially the evening of the swiss cup game in Letzigrund. Thanks to Lorenzo for all the years together scanning together and sharing precious Pb frustration together.

A special thanks goes to Estefani, a person I spent four years with, sharing my daily life, experiments, and much more. Our days were like a rollercoaster of emotions, bad results, great results, frustrations and satisfactions. But I am so glad we met and we could work together for such a long time. A (huge) part of me will miss these moments and will miss spending time together.

In Poggio Lab, many other colleagues contributed to make my days special. Mention to Hinrich, my blond german (but secretly austrian) desk mate and cyling buddy. Countless sunset rides, alpine loops, just enjoying outdoor life. Then a mention to Thibaud. Our table tennis matches on the rooftop of the department were legendary for many years, as well the discussions on Monday morning about how painful the sport activities in the weekend were. Finally a mention to the current and former colleagues in the group I had the pleasure to share time with: Kousik, David, Simon,

Floris, Boris, Francesco, Lukas, Andriani, Daniel, Luca, Mathias, Liza, Aurèle and Aris. I thank all of you for the great time together, inside and outside the lab, and wish you the best for your future.
I would like to thank a few people outside the group, without which the research would have not been possible. I thank Sascha Martin and his team from the mechanical workshop for the outstanding job in supporting us with the probe design and Dominik Sifrig for all the Helium dewars he prepared for us, even on short notice. Finally, Claudia Wirth, for the incredible help in administrative matters over the years, since the moment I chose to move to Switzerland.

Outside of the physics world, I would like to thank some people I spent days and days with, exploring Switzerland and not only that. The dudes from KGB cycling club, Lukasz and Bruno in particular. Some of the best adventures on wheels were done with you guys. Then the guys from Voyage Cycling Club, Reto, Christian, and many others. And finally my good dear friend Stefano, thank you for all the Sundays we spent together pushing all the possible climbs in Switzerland.
Friends can support you also from very far away. This PhD would not have been possible without the constant support of Vieri and Alberto. Friends since 30 years, constantly helping each others and sharing all moments.

Last but not least, my family, my mum Monica, Marco and Annapaola. I know it was hard to see me leaving Italy, and your support was fundamental. And thanks to the person I spent my last years with, Federica, cheering me up and helping me to get out from one of the hardest periods of my life. Hope many more years to come, with trips, laughs and jokes. Thank you Fede.